

ULTRABROADBAND MICROWAVE AND MILLIMETER-WAVE ARBITRARY  
WAVEFORMS: PHOTONIC-ASSISTED GENERATION AND  
RADIO-FREQUENCY APPLICATIONS

A Dissertation

Submitted to the Faculty

of

Purdue University

by

Amir Rashidinejad

In Partial Fulfillment of the  
Requirements for the Degree

of

Doctor of Philosophy

May 2016

Purdue University

West Lafayette, Indiana

Dedicated to my beloved family

## ACKNOWLEDGEMENTS

There are many people who have been of tremendous help to me during my time at Purdue University. I would like to express my utmost gratitude and appreciation to my advisor Professor Andrew M. Weiner for his guidance, support, and patience throughout my graduate studies. My special thanks goes to Dr. Daniel E. Leaird for his invaluable technical support and discussions throughout this research. I would also like to thank Professor Mark R. Bell, Professor James S. Lehnert and Professor Michael D. Zoltowski for serving as my Ph.D. committee members and for their helpful comments and constructive feedback throughout.

I am indebted to my current and former colleagues at the Ultrafast Optics and Optical Communications Laboratory, Dr. Amir Dezfouliyan, Dr. Yihan Li, Dr. Hyoung-Jun Kim, Dr. Victor Torres-Company, Dr. Xiaoxiao Xue, Dr. Joseph Lukens, Dr. Andrew J. Metcalf, Mr. Jose Jarramillo, and Mr. Poolad Imany for their valuable discussions and collaborations. I also thank all the staff of Purdue University who have provided unique environment and made being a graduate student a great experience.

Last but not least, I owe the completion of this stage of my life to my parents, as I do the rest of my accomplishments. Words cannot express the deep appreciation that I hold in my heart for their genuine love and support throughout my life.

*Amir Rashidinejad*

## TABLE OF CONTENTS

	Page
LIST OF TABLES .....	vi
LIST OF FIGURES.....	vii
ABSTRACT .....	xii
1. INTRODUCTION.....	1
1.1 Photonic-Assisted RF-Arbitrary Waveform Generation .....	2
1.2 Organization of the Dissertation and Contribution Summary .....	4
2. FREQUENCY-TO-TIME MAPPING AND CONVENTIONAL PHOTONIC- ASSISTED RF-ARBITRARY WAVEFORM GENERATION .....	7
2.1 Introduction.....	7
2.2 Characteristics of Conventional FTM-based RF-AWG .....	10
3. INTERFEROMETRIC RADIO-FREQUENCY ARBITRARY WAVEFORM GENERATION.....	15
3.1 Introduction.....	15
3.2 Setup Configuration and Mathematical Analysis .....	16
3.3 Numerical Analysis .....	21
3.3.1 Ultrabroadband Continuous Frequency Chirps .....	22
3.3.2 Wideband Frequency-Hopped Spread Spectrum Sequences .....	26
3.4 Experimental Implementation and Results .....	28
3.4.1 Experimental Setup Stabilization.....	29
3.4.2 Ultrabroadband Continuous Frequency-Chirps .....	30
3.4.3 Higher-Order Dispersion Compensation .....	35
3.4.4 Wideband Frequency-Hopped Spread Spectrum Sequences .....	38
4. ENABLING HIGH-SPEED DATA MODULATION FOR RF-ARBITRARY WAVEFORM GENERATION AND APPLICATION IN TIME APERTURE EXPANSION.....	41

	Page
4.1 Introduction.....	41
4.2 Setup Configuration.....	43
4.3 Experimental Results.....	46
4.3.1 Ultrabroadband Chirp Generation.....	46
4.3.2 Programmable Phase Modulation.....	48
4.3.3 Programmable Phase and Amplitude Modulation.....	51
4.4 Time Aperture Expanded RF-AWG.....	53
4.4.1 Principle.....	56
4.4.2 Experimental results.....	61
5. W-BAND ARBITRARY WAVEFORM GENERATION WITH ULTRA-HIGH TIME-BANDWIDTH PRODUCTS AND APPLICATION IN HIGH-RESOLUTION RANGING.....	64
5.1 Introduction.....	64
5.2 W-band Experimental Setup and Components.....	65
5.3 W-band Arbitrary Waveform Generation.....	66
5.4 W-band RF-AWG Phase-Noise Analysis.....	71
5.5 Ultrafine-Resolution Ranging in W-band.....	77
6. ULTRABROADBAND RADIO-FREQUENCY ARBITRARY WAVEFORMS IN DENSE MULTIPATH ENVIRONMENTS.....	83
6.1 Introduction.....	83
6.2 Channel Pre-Compensation via RF-AWG.....	88
6.3 Experimental Study of Multiple Antenna Beamforming.....	92
6.3.1 Experimental Setup.....	93
6.3.2 MISO Beamforming Experiment and Results.....	94
6.4 Theoretical Study of PAPR Gain in MISO Beamforming Systems.....	98
7. SUMMARY AND CONCLUDING REMARKS.....	106
LIST OF REFERENCES.....	109
VITA.....	120

## LIST OF TABLES

Table		Page
2.1	Utilized variables for FTM and TBWP derivations. Optical variables refer to the shaped optical pulse prior to dispersive propagation.....	11
3.1	Length 15 Costas sequence.....	26
5.1	Length 15 Costas sequence.....	69
5.2	Comparison of prominent MMW and sub-THz ranging systems. ....	82
6.1	Comparison of spatio-temporal focusing performance of uncompensated multipath channel, time reversal and phase compensation in the multipath environment of Fig. 6.1. The temporal metrics are averaged over 100 different channel realizations.....	92
6.2	Comparison of spatio-temporal focusing performance of MISO and SISO beamforming experiment in the multipath environment of Fig. 6.1. The temporal metrics are averaged over 100 different channel realizations. ....	97
6.3	Mathematical analysis of channel cross-correlations ( $C_{ij}$ ) for the MISO TR experiments of Section 6.3, normalized to SISO channels' average power ( $P_{avg}^{SISO}$ ). ....	102
6.4	Mathematical analysis of channel cross-correlations ( $C_{ij}$ ) for the MISO PC experiments of Section 6.3, normalized to SISO channels' average power ( $P_{avg}^{SISO}$ ). ....	102
6.5	Normalized correlation coefficients for the uncompensated multipath channels in the experiments of Section 6.3. ....	102
6.6	4×1 MISO beamforming simulations based on channel models 3, 4, 7 and 8 of the IEEE 802.15.4a standard (LOS and NLOS indoor office/factory environment).....	104

## LIST OF FIGURES

Figure	Page
2.1 Cartoon schematic of the frequency-to-time mapping phenomenon for sufficiently large chromatic dispersion. As shown in [49], on page 76. ....	7
2.2 Schematic block diagram for conventional (and near-field) frequency-to-time mapping based RF-AWG. ....	9
2.3 (a-b) Frequency and time domain variables for optical waveforms. (c-d) Frequency and time variables for RF waveforms. Shown in [49], on page 75. ....	11
2.4 Cartoon representation of pulse shaper resolution elements for generating the fastest possible oscillations using conventional (baseband) FTM-based RF-AWG. ....	13
3.1 Ultrabroadband linear frequency downchirp simulation result – (a) DC-blocked temporal waveform ( $e_{des}$ ) and instantaneous frequency (b) Power spectrum of photodetected waveform ( $e_{PD}$ ). ....	16
3.2 Comparison of spatio-temporal focusing performance of MISO and SISO beamforming experiments in the dense multipath channel of Fig. 6.1. ....	24
3.3 Wideband Costas sequence simulation result – DC-blocked temporal waveform ( $e_{des}$ ) and instantaneous frequency. ....	27
3.4 Detailed experimental setup. ....	29
3.5 Ultrabroadband linear frequency downchirp experimental result – (a) DC-blocked temporal waveform ( $e_{des}$ ) and instantaneous frequency (b) Power spectrum. ....	31
3.6 Overlaid temporal representation of 750 different sample measurements of the ultrawideband linear frequency downchirp in Fig. 3.5(a) – Zoomed-in views at (a) higher frequency region (b) lower frequency region. ....	33

Figure	Page	
3.7	Calculated signal constellation plots from long real-time measurements of various quadrature amplitude modulation scenarios and zoom-ins: (a) Rectangular 8-QAM, (b) Rectangular 16-QAM, and (c) Non-rectangular (circular) 16-QAM.....	34
3.8	Overlaid cross-correlation plots of 750 different sample measurements of the ultrawideband linear frequency downchirp in Fig. 3.5 with respect to a common reference.....	35
3.9	Experimental spectrogram curve and numerical instantaneous frequency of (a) Uncompensated linear frequency chirp (b) Dispersion compensated truly-linear frequency chirp.....	37
3.10	Applied unwrapped phase for Costas experiment and corresponding frequency harmonics (Actual phase applied to pulse shaper is modulo $2\pi$ )...	39
3.11	Wideband Costas sequence experimental result – (a) DC-blocked temporal waveform ( $e_{des}$ ) and instantaneous frequency (b) Normalized contour plot of autoambiguity function versus delay and Doppler.....	39
4.1	Schematic for modified interferometric RF-AWG scheme.....	44
4.2	Periodic repetition of ultrabroadband linear down-chirp waveform. (a) 60 ns-long real-time measurement of the generated sequence. (b) Temporal profile of an individual 4 ns-long, 50 GHz bandwidth RF chirp. (c) Normalized spectrogram plot of an individual RF chirp.....	47
4.3	Zoom-in views of the generated ultrabroadband RF waveforms with (a) $0^\circ$ , (b) $90^\circ$ , (c) $180^\circ$ , and (d) $270^\circ$ phase shift. ....	48
4.4	Ultrabroadband BPSK measurement results – (a) Color-coded 60ns window of $4\mu\text{s}$ -long BPSK sequence. (b) Normalized bi-level electrical signal at the input of the phase modulator ( $V_\pi = 2.9\text{V}$ ). (c) Overlay of generated antipodal chirps and zoom-ins.....	49
4.5	Calculated signal constellations from long real-time measurements of various PSK scenarios and zoom-ins: (a) BPSK, (b) QPSK, (c) 16-PSK.....	50
4.6	Ultrabroadband 8-QAM measurement results – (a) Color-coded 60ns window of $4\mu\text{s}$ -long 8-QAM sequence. (b) Normalized electrical drive signal at the input of the IM ( $V_\pi = 3.5\text{V}$ ), and (c) normalized electrical drive signal at the input of the PM ( $V_\pi = 2.9\text{V}$ ).....	52

Figure	Page	
4.7	Calculated signal constellation plots from long real-time measurements of various quadrature amplitude modulation scenarios and zoom-ins: (a) Rectangular 8-QAM, (b) Rectangular 16-QAM, and (c) Non-rectangular (circular) 16-QAM.....	53
4.8	Schematic diagram of time aperture expansion RF-AWG, adapted from [63] (a) Repetitive linear up-chirp waveform train with period $T$ . (b) Autocorrelation function of (a). (c) Chirp train in (a) modulated by a length $L$ regular PN sequence. Polarity of chirps is either maintained (black) or flipped (red). (d) Autocorrelation function of (c), spacing of $T$ between low-power peaks. (e) Chirp train in (a) modulated by a length $L$ amplitude-mismatched PN sequence. Peak-to-peak amplitude of the polarity-maintained chirps in (c) is adjusted to $1+p$ , where $p$ is a PN length dependent value. (f) Autocorrelation function of (e). .....	54
4.9	Schematic diagram of time aperture expansion RF-AWG via phase-detuning (a) Chirp train in Fig. 4.8(a) modulated by a length $L$ phase-shifted PN sequence. An excess phase shift of $\Delta\phi$ is applied to antipodal waveforms. It is shown later that this value depends on the PN sequence length according to Eq. (4.9). (b) Autocorrelation function of (a).....	56
4.10	Measurement results of ultrabroadband linear down-chirp spanning 2-52 GHz – (a) Single waveform and its instantaneous frequency plot. (b) Color-coded 60 ns window of 180 ns-long measurement of length-15 phase-detuned PN coding according to Eq. (4.9). (c) Overlay of two phase-coded basis waveforms of (b) and zoom-in views. ....	60
4.11	Normalized autocorrelation functions of generated ultrabroadband chirp sequences. (a) No Modulation, (b) Length 15 phase-detuned PN modulation, (c) Length 1023 phase-detuned PN modulation. ....	62
5.1	W-band experimental setup – (a) Schematic of waveform generation, transmission and measurement. NBUTC-PD: near-ballistic uni-travelling-carrier photodetector. Tx: transmitter antenna. Rx: receiver antenna. LNA: low noise amplifier. (b) Close-up of optical-to-electrical conversion block, followed by Tx feed. (c) Transmitter block. (d) Receiver block. ....	65
5.2	W-band RF-arbitrary waveform generation – (a) Down-converted measurements using various local oscillator (LO) frequencies. (b),(c) Reconstructed W-band waveform and spectrogram of ultrabroadband linear down-chirp.....	68

Figure	Page
5.3 W-band Costas Implementation – (a) Reconstructed frequency-hopped Costas sequence (plotted in baseband) and corresponding instantaneous frequency. (b) Computed auto-ambiguity function of the waveform in (a). ..	70
5.4 Phase-noise measurement results – (a) Temporal profile of the down-converted 80 GHz waveform (LO = $2 \times 39$ GHz). (b) Phase-noise measurements of the down-converted 80 GHz waveform (in blue), utilized LO frequency at 39 GHz (in red), and its ideal projection to 78 GHz (in green). .....	73
5.5 Phase-noise measurement of a 5 GHz RF signal generated using state-of-the-art electronic AWG and its projection to 80 GHz assuming ideal up-conversion.....	75
5.6 Comparison between the projected phase-noise of state-of-the-art electronic AWG versus down-converted phase-noise of our photonic-assisted RF-AWG, both at 80 GHz. ....	77
5.7 Ultra-high resolution W-band ranging experiments. – (a) Setup schematic (b) NBUTC-PD chips. (c) Electrical and optical probing configuration. (d) Tunable double-plate reflector set. (e) Photograph of an example ranging experiment with all 4 objects in the beam path (from Tx-Rx pair point-of-view). .....	78
5.8 High-resolution W-band multi-target ranging experimental results – (a) Ranging results with un-modulated sensing waveform. (b) Ranging results with length-15 modified PN-modulated sensing waveform. (c) Magnified view from 24-26 ns of (b).	80
5.9 Ultrafine resolution W-band ranging experimental results – (a) ~10 mm target separation. (b) ~6 mm target separation. (c) ~4 mm target separation.	81
6.1 Highly-dense multipath channel measurement – (a) Bird’s eye view of the laboratory environment. Tx: Transmitter, Rx: Receiver (on 80cm $\times$ 80cm positioner grid). (b) Channel impulse response. (c) Channel spectral content.	84
6.2 Beamforming in the NLOS multipath environment of Fig. 6.1 – (a) Time reversal (TR). (b) Phase compensation (PC). .....	89
6.3 Spatial focusing in the NLOS multipath ultra-wideband channel of Fig. 6.1(a) (right: 3D view, left: bird’s eye view) – (a) Time reversal (TR). (b) Phase compensation (PC). .....	90

Figure		Page
6.4	Block diagram of the MISO testbed. Inset in bottom right shows the received waveform as a result of chirp excitation. As shown in [49] on page 65.....	93
6.5	TR temporal focusing comparisons – (a) $4 \times 1$ MISO configuration and (b) TR for only channel 1, $h_1(t)$ . Amplitudes are normalized to the peak voltage level measured at Rx from only a single antenna TR excitation. ....	95
6.6	PC temporal focusing comparisons – (a) $4 \times 1$ MISO configuration and (b) PC for only channel 1, $h_1(t)$ . Amplitudes are normalized to the peak voltage level measured at Rx from only a single antenna PC excitation.....	96
6.7	Spatial focusing comparisons in $4 \times 1$ MISO configuration – (a) Time reversal and (b) Phase compensation. ....	96

## ABSTRACT

Rashidinejad, Amir. Ph.D., Purdue University, May 2016. Type Ultrabroadband Microwave and Millimeter-wave Arbitrary Waveforms: Photonic-Assisted Generation and Radio-Frequency Applications. Major Professor: Andrew M. Weiner.

Ultrabroadband microwave and millimeter-wave signals offer significant potentials for various applications from ultrahigh-speed communications to high-resolution ranging and electromagnetic imaging. The key challenge in advancing these technologies is generating broadband programmable waveforms centered at such high frequencies. Electronic RF arbitrary waveform generation (RF-AWG) typically suffers from limited digital-to-analog converter speed and high timing jitter, which is why, over the past couple of decades, researchers have shifted their attention toward robust photonic-assisted RF-AWG schemes.

In this dissertation, we first present a novel photonic strategy to generate programmable waveforms in the microwave, millimeter-wave and even sub-terahertz frequency regimes. Mathematical and experimental analyses confirm the superiority of our technique over its electronic and photonics-based counterparts in terms of bandwidth, center frequency, time-bandwidth product, stability and timing jitter. Furthermore, a simple modification of the presented RF-AWG setup is introduced that enables immediate incorporation of real-time data modulation on the generated programmable RF waveforms

for high-speed communication and time-aperture expansion applications. We then employ our RF-AWG waveforms in a W-band (75-110 GHz) high-resolution ranging experiment, achieving an unprecedented depth resolution of 3.9 mm. Finally, a mathematical and experimental assessment of temporal and spatial focusing of single- and multiple-antenna ultra-wideband systems in highly-dense multipath environments is carried out by means of RF arbitrary waveform generation.

## 1. INTRODUCTION

During the last couple of decades, broadband and ultrabroadband radio-frequency (RF) arbitrary waveform generation (RF-AWG) has received a great deal of attention from both academic and industrial communities [1]. This surge of interest is a direct result of showing vast potentials for generating electrical signals that not only exhibit absolute bandwidths well over 500 MHz, but are also arbitrarily programmable to suit and advance many different applications [1,2]. However, due to the over-congestion of previously-accessible low frequency regimes – generally below several gigahertz (GHz) – the main focus was very soon shifted toward generating ultrabroadband arbitrary electrical signals in the high-microwave ( $\mu$ -wave), millimeter-wave (MMW) and sub-terahertz (sub-THz) frequencies [3]. Accessing such high RF frequency regions not only circumvents the extreme spectral congestion of lower frequency bands, but also opens up the potential for utilizing unprecedented ultrabroad bandwidths for applications like ultrahigh-speed wireless communication [4-9], high-resolution ranging [10-12], electromagnetic imaging and tomography [13-16], and high-speed spectroscopy [17-20].

Although RF-AWG has been successfully demonstrated for the low  $\mu$ -wave region using many different electrical schemes and electronic configurations, they generally lack the potential to be scaled to higher frequencies, such as the regulated 60 GHz or 100 GHz frequency bands [21]. For example, as a result of digital-to-analog converter (DAC) speed

limitations, the current state-of-the-art electronic arbitrary waveform generator (commercially available since late 2015) is restricted to signals from DC (0 Hz) to only 20 GHz [22]. This issue is less intense for photonic-assisted approaches, which show no inherent restriction in terms of the bandwidth or center frequency of the generated programmable waveforms. However, as a result of many of these schemes still being in the infancy stage, there has only been a few demonstrations of photonic-assisted RF-AWG at higher than 15 GHz [23-27]. Moreover, as will be discussed later in this dissertation, there are other issues like achievable time-bandwidth product (TBWP), RF jitter and phase-noise performance that remain to be comprehensively addressed for photonic-assisted RF-AWG schemes.

### **1.1 Photonic-Assisted RF-Arbitrary Waveform Generation**

As discussed earlier, due to practical limits associated with DAC technology, electronic RF-AWG is not very favorable for accessing high frequency regimes. Additionally, these methods suffer severely from the viewpoint of timing jitter, electromagnetic interference (EMI) and bulkiness. Photonic-assisted strategies, however, owing to their inherent broadband nature, have proven to be very attractive solution for  $\mu$ -wave, MMW, and even sub-THz generation [27-32].

Many RF-photonics schemes have been developed to generate a wide variety of desirable RF waveforms at high frequencies [23-27, 33-44]. For example, chirped MMW pulse generation has drawn a great deal of research attention in the RF-photonics community [24,25, 37-41]. Another example of RF-photonics waveform generation is the ability to construct frequency-hopped microwave pulses with indefinite record lengths by

exploiting the ultrafast switching capability and optical pulse shaping resources available in photonics [42,43].

Other techniques, on the other hand, are not only aimed at generating specific classes of waveforms, but target the possibility of creating programmable RF waveforms [24,26,33-36]. These photonic-assisted RF-AWG schemes allow the user to define, in a reconfigurable manner, any desired RF waveform that could be employed in various applications. Among the many photonic RF-AWG techniques, those relying on optical pulse shaping [44,45] and the concept of frequency-to-time mapping (FTM) offer better performance in terms of signal fidelity and reconfigurability [24, 34-36]. In these techniques, the spectrum of an ultrafast laser pulse train is manipulated using optical pulse shaping configurations. This tailored spectrum is then mapped to the time domain by stretching the optical pulses through a dispersive medium, resulting in a programmable optical intensity profile. The resultant optical intensity can be easily mapped to the RF domain using a high-speed photodetector.

Current photonic-assisted RF-AWG technology is mainly baseband in nature, which creates some implications in terms of scaling to higher frequencies and maximum achievable TBWP [46]. Although recent advances have demonstrated an impressive ability to generate arbitrary waveforms spanning DC to 41 GHz with a TBWP of  $\sim 280$  [24], in high-frequency passband scenarios, these schemes tend to fall quite short of their performance characteristics [46]. Moreover, issues like RF jitter and phase-noise performance for these photonic RF-AWG require more in-depth analysis.

## 1.2 Organization of the Dissertation and Contribution Summary

Chapter 2 describes the basic mathematical concepts, on which the ideas presented in this dissertation are built upon. This chapter starts by introducing the detailed governing equations regarding dispersion and frequency-to-time mapping. Subsequently, a recount of the original idea for Fourier transform (FT) pulse shaper-based RF-AWG, referred to as *Conventional* FTM-based RF-AWG, is presented and its main performance features are evaluated.

In Chapter 3, we present a novel scheme for photonic-assisted RF-AWG based on optical interferometry, pulse shaping and frequency-to-time mapping. The presented interferometric shaping design enables creating programmable passband RF waveforms with independent control over center frequency, temporal amplitude and temporal phase. In-depth theoretical analysis and numerical simulations are accompanied by experimental results for several classes of interesting RF waveforms, spanning up to 50 GHz. We also verify the ability to successfully achieve the upper-bound time-bandwidth product capability from our setup (limited by the number of frequency-resolved pulse shaper elements), regardless of the center frequency of the target waveform. Comparisons with conventional RF-AWG schemes are also provided in this section.

In Chapter 4, we present a novel modification to the photonics-based RF-AWG technique described in Chapter 3. This simple adaption allows the incorporation of high-speed real-time data modulation with the RF-AWG system and is simply implemented using a pair of optical phase and intensity modulators in the setup. Various phase-shift keying (PSK) and quadrature-quadrature amplitude modulation (QAM) experiments are performed on programmable RF waveforms with ~50 GHz bandwidth. One major

limitation of photonic-assisted RF-AWG is that waveforms may be generated over only a limited time aperture. Later in this chapter, by taking advantage of the unique modulation capability of our RF-AWG setup, we develop an innovative binary coding strategy that circumvents this issue and enables an increase in the nanosecond-level time aperture to several microseconds and beyond, with a corresponding increase in TBWP.

Chapter 5 consists of experiments carried out using the previous proposed setup in the low atmospheric absorption region of 75-110 GHz, termed W-band [21]. Based on the Federal Communications Commission (FCC) regulations, the W-band is one of only a few allocated frequency regions, in which up to 35 GHz of bandwidth is entirely available for various applications. In these experiments, we first design arbitrary RF waveforms that cover the full allocated band with maximal TBWP and then provide a configuration to be able to down-convert and measure the generated signals. The generated signals are further evaluated in terms of jitter and phase-noise performance and compared with other competitive electronic and photonic-assisted schemes. Later in this chapter, we utilize these ultrabroadband sensing signals in an application setting, namely ultrahigh-resolution ranging; and achieve an unprecedented 3.9mm range resolution over more than 5 meters of ranging distance.

In Chapter 6, in contrast to the previous chapters in which photonics-based schemes were used to synthesize arbitrary RF waveforms, an electronic RF-arbitrary waveform generator is utilized to analyze some characteristics of highly-dense ultra-wideband (UWB) electrical channels below 12 GHz. By taking advantage of programmable RF waveform generation, two pre-compensation schemes, namely Time Reversal [47] and Phase Compensation [48], are implemented to experimentally analyze the temporal and spatial

focusing characteristics of these channels in single- and multiple-antenna scenarios. Lastly, a mathematical assessment is provided to derive the equations that govern the limits to the temporal focusing performance of these schemes in multiple-antenna configurations and the results are compared with and confirm our experimental data.

Finally, in Chapter 7, we summarize our results and discuss concluding remarks and future research possibilities.

## 2. FREQUENCY-TO-TIME MAPPING AND CONVENTIONAL PHOTONIC-ASSISTED RF-ARBITRARY WAVEFORM GENERATION

### 2.1 Introduction

As introduced in the previous chapter, most photonic-assisted RF-AWG schemes rely on the concept of frequency-to-time mapping (FTM) via passing a shaped optical pulse train through a 1<sup>st</sup>-order dispersive medium. Figure 2.1 shows a cartoon description of this phenomenon. When compressed optical pulses propagate through a 1<sup>st</sup>-order dispersive element (with group delay dispersion), different wavelengths travel at different speeds. For large enough dispersion values, this propagation results in a linear frequency-dependent time delay, which maps the input pulses' power spectrum (frequency) to the output pulses' temporal intensity profile (time), hence the name frequency-to-time mapping.

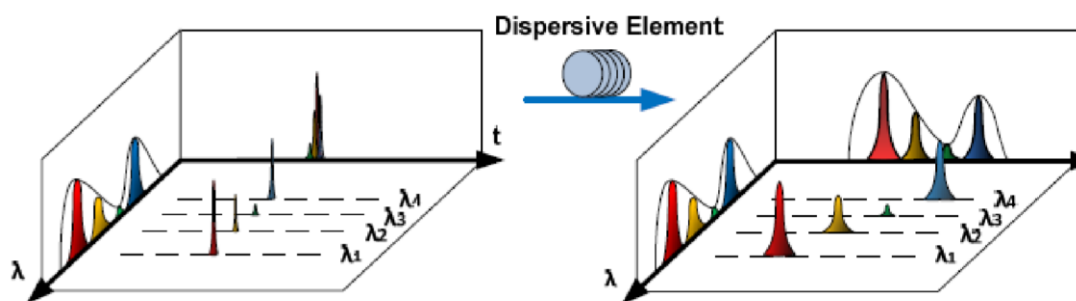


Figure 2.1: Cartoon schematic of the frequency-to-time mapping phenomenon for sufficiently large chromatic dispersion. As shown in [49], on page 76.

Mathematically, the transformation of a pulse travelling through 1<sup>st</sup>-order dispersion ( $\psi_2$ ) can be expressed by the Fresnel integral as:

$$a_{out}(t) \propto e^{-j\left(\frac{t^2}{2\psi_2}\right)} \int_{\langle\sigma_{in}\rangle} a_{in}(t') e^{-j\left(\frac{t'^2}{2\psi_2}\right)} e^{j\left(\frac{tt'}{\psi_2}\right)} dt' \quad (2.1)$$

where  $a_{in}(t)$  and  $a_{out}(t)$  are respectively the complex envelopes of the optical pulses before and after the dispersive medium. Here  $\psi_2$  (units  $s^2$ ) is the group delay dispersion, defined as  $\psi_2 = -\partial^2\beta(\omega)/\partial\omega^2 \cdot L$ , where  $\beta(\omega)$  is the propagation constant of the medium with length  $L$ . In some applications, notably fiber optics, the fiber dispersion is usually described in terms of  $D$ , with units  $ps.nm^{-1}.km^{-1}$ . This parameter relates to group delay dispersion as  $\psi_2 = -(\lambda^2 D)/(2\pi c) \cdot L$ , where  $\lambda$  and  $c$  are the wavelength and velocity of light in free-space/vacuum.

When the amount of dispersion is sufficiently large such that  $\sigma_{in}^2/2|\psi_2| \ll \pi$ , the *far-field limit* is satisfied [50,51] and the quadratic phase factor  $\exp(-jt'^2/2\psi_2)$  in the integral in (2.1) can be ignored. In this limit the output optical waveform's intensity is simply a scaled replica of the optical power spectrum, i.e.:

$$|a_{out}(t)|^2 \propto \left| e^{-j\left(\frac{t^2}{2\psi_2}\right)} \int_{\langle\sigma_{in}\rangle} a_{in}(t') e^{j\left(\frac{tt'}{\psi_2}\right)} dt' \right|^2 \propto \left| A_{in}\left(\tilde{\omega} = -\frac{t}{\psi_2}\right) \right|^2 \quad (2.2)$$

where  $A_{in}(\tilde{\omega})$  is the complex spectral envelope function of  $a_{in}(t)$ . Note that we use the symbol  $\tilde{\omega} = \omega - \omega_0$  (where  $\omega_0$  is the center frequency of the optical pulses in  $rad/s$ ) to emphasize that  $A_{in}(\tilde{\omega})$  is the baseband Fourier transform of  $a_{in}(t)$ .

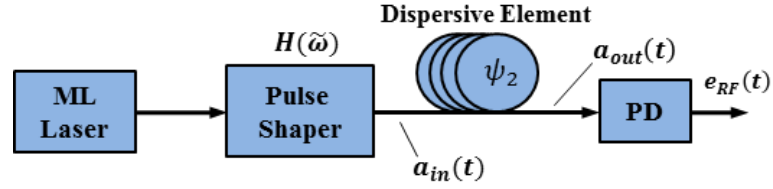


Figure 2.2: Schematic block diagram for conventional (and near-field) frequency-to-time mapping based RF-AWG.

From (2.2), one can clearly see the potential of utilizing FTM for RF-AWG, by arbitrarily shaping the input pulses' optical spectrum and detecting the output intensity on a photodetector. The setup schematic for conventional FTM-based RF-AWG is depicted in Fig. 2.2., where a programmable RF temporal field profile is generated, as below:

$$e_{RF}(t) \propto |a_{out}(t)|^2 \propto \left| A_{in} \left( \tilde{\omega} = -\frac{t}{\psi_2} \right) \right|^2 \quad (2.3)$$

Of course, this programmable signal has to be completely positive, since it is physically equal to a photodetected intensity, however, special techniques have been proposed to generated bipolar RF signals in the same manner [26,36].

It is worth noting that the only considerations we took into account for the FTM derivations of (2.3) are:

- 1- The far-field condition is satisfied, i.e., the length of utilized dispersion is long enough such that the excess quadratic phase term in the Fresnel integral of equation (2.1) is negligible.
- 2- The optical-to-electrical conversion speed is adequately high, i.e., the photodetector bandwidth is large enough such that fine temporal variations of  $|A_{in}(\tilde{\omega} = -t / \psi_2)|^2$  can be mapped directly to the RF domain without any distortion.

As will be discussed in later sections of this dissertation, both of these restrictions play a major role in any FTM-based RF-AWG scheme and must not be overlooked.

## 2.2 Characteristics of Conventional FTM-based RF-AWG

As introduced in Fig. 2.2, the general setup for conventional FTM-based RF-AWG includes an optical pulse shaping mechanism. More correctly, since in conventional FTM-based RF-AWG, the far-field condition is assumed to be satisfied, only spectral amplitude shaping is required from the pulse shaper and optical spectral phase is irrelevant. Recently in our group, a work on *near-field* frequency-to-time mapping (NF-FTM) was conducted, showing the possibility that using the same setup as that of Fig. 2.2 and accessing the previously unused spectral phase shaping ability of the optical pulse shaper, the far-field condition can be achieved for radically reduced dispersion lengths (and hence reduced time-apertures) [24], leading to the ability to obtain similar results to that of (2.3).

In both conventional and near-field FTM schemes, the utilized pulse shaper sets the limits for waveform generation. First of all, as is obvious from (2.3), the complexity of the engineered RF waveform is directly proportional to the complexity of the applied optical shaping function. For example, if a very coarse resolution pulse shaper is employed, the resultant RF signal will also have coarse temporal features as compared to its time duration. To facilitate the formulation of the relationship between pulse shaper spectral resolution and RF-AWG signal complexity, we assume a bandwidth-limited optical pulse is sent through a programmable optical pulse shaper, after which its characteristics are described in Fig. 2.3 and Table 2.1.

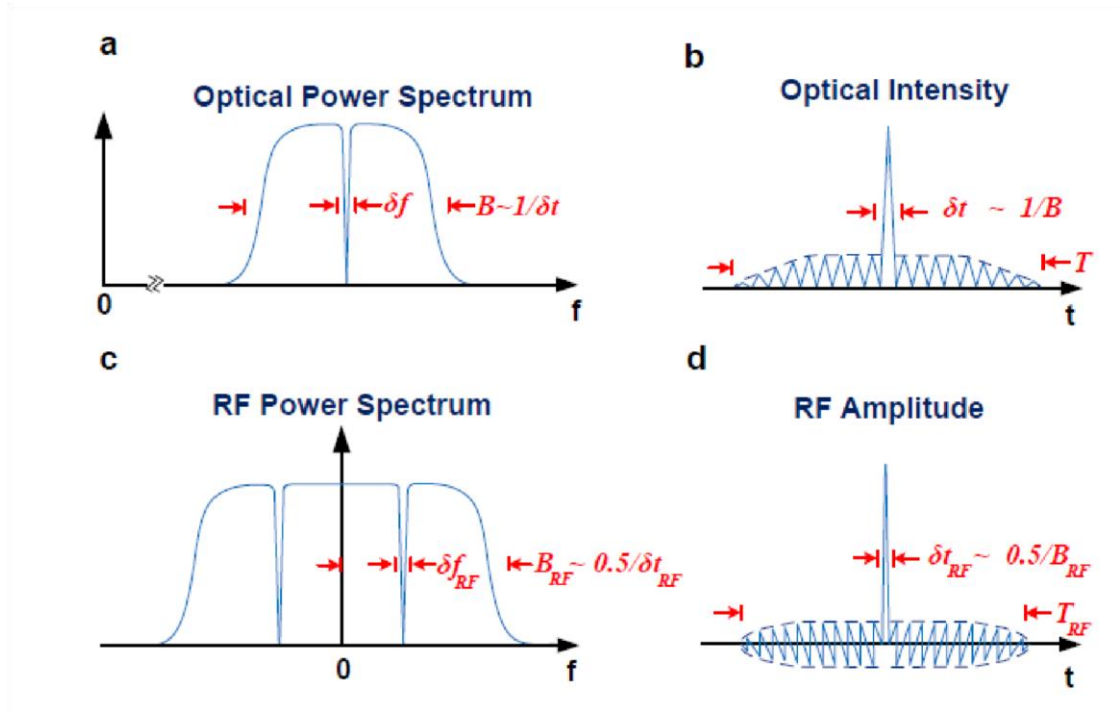


Figure 2.3: (a-b) Frequency and time domain variables for optical waveforms. (c-d) Frequency and time variables for RF waveforms. Shown in [49], on page 75.

Table 2.1: Utilized variables for FTM and TBWP derivations. Optical variables refer to the shaped optical pulse prior to dispersive propagation.

Symbol	Meaning	Symbol	Meaning
$\delta t$	Optical time resolution ( <i>sec</i> )	$\delta t_{RF}$	RF time resolution( <i>sec</i> )
$T$	Optical time aperture ( <i>sec</i> )	$T_{RF}$	RF time aperture ( <i>sec</i> )
$B$	Optical bandwidth ( <i>rad/s</i> )	$B_{RF}$	RF bandwidth ( <i>Hz</i> )
$\delta\omega$	Optical spectral resolution ( <i>rad/s</i> )	$\delta f_{RF}$	RF spectral resolution ( <i>Hz</i> )

First, we define signal complexity for RF-AWG schemes based on the parameters outlined in Table 2.1 and Fig. 2.3. An RF burst's complexity, can be described as being proportional to the ratio between its total temporal duration and the duration of its shortest temporal features ( $T_{RF}/\delta t_{RF}$ ), or equivalently, the ratio between the bandwidth of the generated chirp to its smallest spectral feature ( $B_{RF}/\delta f_{RF}$ ). Using time-frequency relationships [52], one can reformulate RF signal complexity as:

$$\text{Signal Complexity} \propto \frac{T_{RF}}{\delta t_{RF}} \propto B_{RF} \cdot T_{RF} = \text{TBWP} \quad (2.4)$$

where, TBWP (short for time-bandwidth product) is the product of the time aperture of the generated RF signal and its bandwidth (non-negative bandwidth). It is clear from (2.4) that TBWP is a good criterion to use as a means of comparison for signal complexity for various RF-AWG schemes, and will be utilized in that manner throughout the remainder of this dissertation.

Based on Table 2.1 and Fig. 2.3, and the derivations provided in [46,52], after dispersive propagation (far-field limit for conventional FTM, and respectively the now less-demanding limit for NF-FTM), the temporal duration of the generated RF signal as well as the maximum achievable RF frequency can be approximated as follows:

$$T_{RF} \simeq B \times |\psi_2| = N\delta\omega \times |\psi_2| \quad (2.5)$$

$$f_{max} \simeq \frac{1}{2\delta\omega \times |\psi_2|} \quad (2.6)$$

where,  $N = B/\delta\omega = T/\delta t = T \times B$  is the time-bandwidth produce of the bandwidth limited shaped optical signal prior to dispersive propagation. As a matter of fact, this  $N$  parameter is equal to the number of spectrally-resolved optical pulse shaper resolution elements. Equations (2.5) and (2.6) can be understood from the simple explanation that

for conventional schemes (which rely mainly on spectral amplitude shaping for signal synthesis), to create the fastest achievable frequency oscillations, one must consume at least two pulse shaper resolution elements, one for the positive half-cycle and one for the negative half-cycle. A simple depiction of this is provided in Fig. 2.4, showing the target optical spectrum (equivalent to target RF temporal field profile) and corresponding function programmed onto the pulse shaper.

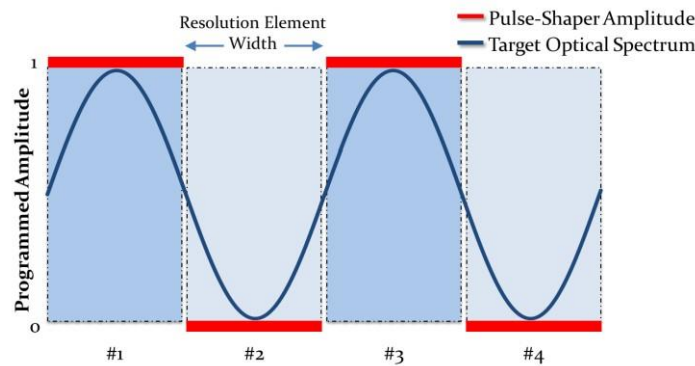


Figure 2.4: Cartoon representation of pulse shaper resolution elements for generating the fastest possible oscillations using conventional (baseband) FTM-based RF-AWG.

Since conventional (and near-field) FTM-based RF-AWG schemes both have limits on the maximum achievable frequency oscillations, for any fixed length of dispersion ( $\psi_2$ ), the maximum achievable TBWP (equivalent to maximum signal complexity) is attained when the signal covers DC to  $f_{max}$ . This is the main reason why these techniques are sometimes referred to as *baseband* RF-AWG schemes, since their maximum performance capabilities are achieved when the generated signal is baseband, while for passband settings the generation technique falls quite short of its maximum

capacity. This way, the bandwidth of the generated electrical signal can be expressed as  $B_{RF} = f_{max} - 0 = f_{max}$ , setting the maximum TBWP of these schemes as follows:

$$\text{TBWP} = T_{RF} B_{RF} = T_{RF} \cdot f_{max} = \frac{N}{2} \quad (2.7)$$

Thus, (2.7) clearly shows that for baseband RF-AWG schemes, the TBWP is capped at half the number of pulse shaper resolution elements, and one cannot use the full  $N$  degrees of freedom provided by the pulse shaper. In other words, a programmable optical signal with TBWP of  $N$  is used to create a programmable RF signal with TBWP of only  $N/2$ .

In the next chapter, we present a novel photonics-based RF-AWG scheme that can actually achieve TBWP values in the proximity of this limit ( $N$ ), which can be considered as an upper-bound for all pulse shaper-based RF arbitrary waveform generation methods. The presentation of this RF-AWG technique is accompanied by numerical, simulation and experimental results, leading to the generation of RF-arbitrary waveforms with frequency content far larger than previous electronic or photonic RF-AWG demonstrations [27].

### 3. INTERFEROMETRIC RADIO-FREQUENCY ARBITRARY WAVEFORM GENERATION

#### 3.1 Introduction

As clearly stated in the previous chapter, conventional FTM-based RF-AWG schemes, can only achieve half of the possible TBWP capability allowed by the utilized pulse shaping mechanism. Furthermore, these schemes were proven to be inherently baseband, requiring full coverage from DC to a specific maximum frequency to achieve the mentioned TBWP. In this chapter, we present our work on a novel FTM-based RF-AWG scheme that utilizes an optical interferometric configuration to achieve the upper bound TBWP allowed by the pulse shaper resolution [46]. Furthermore, we prove that our technique is inherently passband, thus changing the center frequency of the target spectrum will not affect the maximum achievable TBWP.

This means, that we not only double the TBWP of conventional baseband FTM-based schemes, but for passband settings, such as those in the vicinity of 60 or 100 GHz, our scheme provides an even more impressive advantage [46]. The results presented in this chapter were originally published by us in the *IEEE Journal of Lightwave Technology* in early 2014 [46].

### 3.2 Setup Configuration and Mathematical Analysis

The basic schematic of our proposed technique is depicted in Fig. 3.1. The system consists of a short-pulse mode-locked (ML) laser, an interferometric pulse shaping system, a quadratic dispersive element, and a (preferably high speed) photodetectors (PD). The interferometric shaping subsystem is composed of an optical pulse shaper and a polarization controller (PC) in one arm; as well as a variable delay line (VDL) and a variable optical attenuator (VOA) in the other. In Fig. 3.1,  $a_{ML}(t)$  denotes the complex temporal envelope function of bandwidth-limited short optical pulses created within the ML laser cavity. For the sake of theoretical analysis, we assume a flat optical spectrum for these pulses spanning an optical bandwidth of  $B$  about the center frequency  $\omega_0$  in  $rad/s$ . The Fourier representation of the ML pulses is expressed as  $A_{ML}(\tilde{\omega})$ .

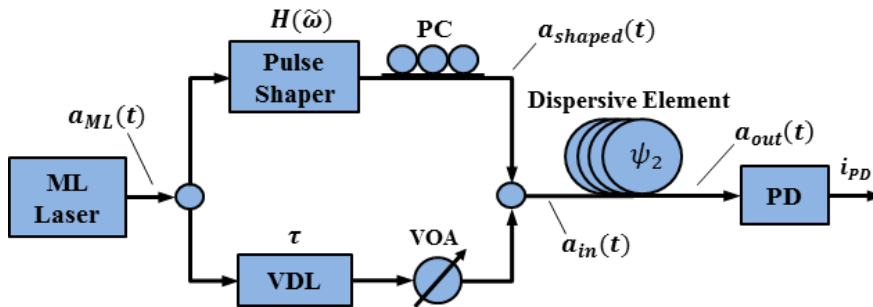


Figure 3.1: Basic schematic block diagram for proposed interferometric (passband) RF-AWG scheme.

Upon arrival at the optical interferometer, the wideband pulses from the ML-laser are equally split into two arms using a 50-50 optical splitter. The high-resolution pulse shaper then imparts a programmable transfer function (independently in amplitude and

phase) onto the pulses travelling across the top arm; while the other arm merely delays the signals that traverse through it. The PC and VOA are employed in the general design only to ensure perfect matching of the polarization state and optical power of the pulses travelling through the two interfering arms. Therefore, without any loss of generality we can neglect these components' effects in mathematical evaluations.

According to the above explanations, we can express the Fourier transform of the signals in Fig. 3.1 as:

$$A_{shaped}(\tilde{\omega}) \propto A_{ML}(\tilde{\omega}) \cdot H(\tilde{\omega}) \quad (3.1)$$

$$A_{in}(\tilde{\omega}) \propto A_{shaped}(\tilde{\omega}) + A_{ML}(\tilde{\omega}) \cdot e^{-j\omega\tau} \propto (H(\tilde{\omega}) + e^{-j(\tilde{\omega}+\omega_0)\tau}) \cdot A_{ML}(\tilde{\omega}) \quad (3.2)$$

where  $\tau$  is the delay applied using VDL and  $H(\tilde{\omega})$  is the shaper's programmable transfer function. To be completely general, we must keep in mind that  $\tilde{\omega} \in [-B/2, B/2]$ .

At this point, the spectrum of the optical waveform has been appropriately shaped via the programmable interferometric shaper, resulting in a field which we denote by its complex envelope  $a_{in}(t)$ . In order to map this arbitrariness to the time domain, FTM is utilized. Plugging (3.1) and (3.2) in the Fresnel integral, at the far-field limit, similar to conventional FTM, we have:

$$|a_{out}(t)|^2 \propto \left| A_{in} \left( \tilde{\omega} = \frac{-t}{\psi_2} \right) \right|^2 \quad (3.3)$$

However, satisfying the far-field condition in our setup is not as trivial as it seems, since as a result of the delay  $\tau$ , the signal  $a_{in}(t)$  now may potentially have a larger time aperture as compared to that of  $a_{shaped}(t)$ . To take into account this hidden, but critically important consideration in our calculations, we expand the Fresnel integral in terms of its components,  $a_{shaped}(t)$  and  $a_{ML}(t)$ , as follows:

$$a_{out}(t) \propto e^{-j\left(\frac{t^2}{2\psi_2}\right)} \times \left\{ \int a_{shaped}(t') e^{-j\left(\frac{t'^2}{2\psi_2}\right)} e^{j\left(\frac{tt'}{\psi_2}\right)} dt' + \int a_{ML}(t' - \tau) e^{-j\left(\frac{t'^2}{2\psi_2}\right)} e^{j\left(\frac{tt'}{\psi_2}\right)} dt' \right\} \quad (3.4)$$

Through (3.4), one can see that by choosing  $\psi_2$  large enough to satisfy the far-field limit for  $a_{shaped}(t)$ , the quadratic phase term is eliminated only from the first integral; whereas the requirement for the second integral appears to be more demanding and apparently dependent on the delay variable,  $\tau$ . With a change of variables and after reorganizing the phase terms, we can express the second integral in (3.4) as:

$$\begin{aligned} & \int a_{ML}(t' - \tau) e^{-j\left(\frac{t'^2}{2\psi_2}\right)} e^{j\left(\frac{tt'}{\psi_2}\right)} dt' \\ &= e^{-j\left(\frac{\tau^2}{2\psi_2}\right)} e^{j\left(\frac{t\tau}{\psi_2}\right)} \int_{\langle\sigma_{ML}\rangle} a_{ML}(t') e^{j\left(\frac{tt'}{\psi_2}\right)} e^{-j\left(\frac{(t'+2\tau)t'}{2\psi_2}\right)} dt' \end{aligned} \quad (3.5)$$

where  $\sigma_{ML}$  is the time aperture of the extremely short optical pulses, which is on the order of a hundred femtoseconds in our experiments. Using a similar argument to that of the far-field condition [50,51], the last phase term in the integral in (3.5) can be ignored assuming that:

$$\left| \frac{\sigma_{ML}(2\tau + \sigma_{ML})}{2\psi_2} \right| \simeq \left| \frac{\tau\sigma_{ML}}{\psi_2} \right| \ll \pi \quad (3.6)$$

Later, through our numerical and experimental results, we show that for generating waveforms in the MMW, microwave and sub-THz regions,  $\tau$  is required to take on values from a few tens to hundreds of picoseconds and more, which justifies the approximation  $|\tau| \gg \sigma_{ML} \simeq 0.1$  ps in (3.6).

Assuming (3.6) is satisfied, the last phase term in the integral in (3.5) is also negligible, and we have:

$$\begin{aligned}
& \int a_{ML}(t' - \tau) e^{-j\left(\frac{t'^2}{2\psi_2}\right)} e^{j\left(\frac{tt'}{\psi_2}\right)} dt' \\
& \simeq e^{-j\left(\frac{\tau^2}{2\psi_2}\right)} e^{j\left(\frac{t\tau}{\psi_2}\right)} \int_{(\sigma_{ML})} a_{ML}(t') e^{j\left(\frac{tt'}{\psi_2}\right)} dt' \\
& = e^{-j\left(\frac{\tau^2}{2\psi_2}\right)} \cdot e^{j\left(\frac{t\tau}{\psi_2}\right)} \cdot A_{ML}\left(\tilde{\omega} = \frac{-t}{\psi_2}\right)
\end{aligned} \tag{3.7}$$

From (3.4) and (3.7), when both the far-field condition for  $a_{shaped}(t)$  and the requirement in (3.6) are fulfilled, we have:

$$|a_{out}(t)|^2 \propto \left| A_{shaped}\left(\tilde{\omega} = \frac{-t}{\psi_2}\right) + e^{-j\left(\frac{\tau^2}{2\psi_2}\right)} \cdot e^{j\left(\frac{t\tau}{\psi_2}\right)} \cdot A_{ML}\left(\tilde{\omega} = \frac{-t}{\psi_2}\right) \right|^2 \tag{3.8}$$

We prove later in this section that the constraint in (3.6) is independent of, and thus not contradictory to, the far-field condition for  $a_{shaped}(t)$ , and is always satisfied for waveforms up to the sub-THz frequency regime.

With these assumptions in mind, by substituting (3.1) in (3.8), the following equation describes the photodetected RF waveform:

$$\begin{aligned}
e_{RF}(t) \propto |a_{out}(t)|^2 \propto & 1 + \left| H\left(\frac{-t}{\psi_2}\right) \right|^2 \\
& + 2 \left| H\left(\frac{-t}{\psi_2}\right) \right| \cdot \cos\left(\frac{t\tau}{\psi_2} - \angle H\left(\frac{-t}{\psi_2}\right) + \phi_0\right)
\end{aligned} \tag{3.9}$$

where  $\phi_0 = -\tau^2/2\psi_2$  is just a constant phase. Note here that in (3.9), we have dropped the  $|A_{ML}(\tilde{\omega})|$  terms, owing to the fact that the original spectrum is flat and frequency independent. Also  $H(\tilde{\omega})$  is decomposed into its independent phase and amplitude terms using the corresponding symbols.

The RF signal of the photodetector can be decomposed into two individual terms, a positive baseband component, namely  $1 + \left|H\left(\frac{-t}{\psi_2}\right)\right|^2$ , and a programmable passband component described as below:

$$e_{des}(t) \propto \left|H\left(\frac{-t}{\psi_2}\right)\right| \cdot \cos\left(\frac{t\tau}{\psi_2} - \angle H\left(\frac{-t}{\psi_2}\right) + \phi_0\right) \quad (3.10)$$

The shorthand notation  $e_{des}(t)$  is employed to emphasize that this component of the photodetected waveform is the *desired* signal and will be the main focus of this dissertation heron in.

Equation (3.10) demonstrated the ability of the proposed scheme to independently control the temporal amplitude, temporal phase and center frequency of  $e_{des}(t)$  through the pulse shaper amplitude, pulse shaper phase and the applied delay using VDL, respectively. More specifically, we have:

$$\text{Temporal Amplitude} \propto \left|H\left(\frac{-t}{\psi_2}\right)\right| \text{ a.u.} \quad (3.11a)$$

$$\text{Temporal Phase} = \frac{t\tau}{\psi_2} - \angle H\left(\frac{-t}{\psi_2}\right) + \phi_0 \text{ rad} \quad (3.11b)$$

$$\text{Center Frequency} = f_C - \left|\frac{\tau}{2\pi\psi_2}\right| \text{ Hz} \quad (3.11c)$$

The above three equations, clearly show the simplicity of the described RF-arbitrary waveform generation (RF-AWG) method. At the far-field limit, for a fixed value of dispersion, setting the appropriate value for  $\tau$  enables extremely wide-range center frequency tuning, while manipulating the phase and amplitude function of the pulse shaper enables independent control over the arbitrary amplitude and phase function of the generated signal.

At this point we are also able to present a clear proof regarding the satisfaction of (3.6). According to (3.11c), we can express  $\tau$  in terms of the desired center frequency ( $f_C$ ) and the dispersion amount ( $\psi_2$ ). This can be substituted in (3.6) and after some cancellations, the statement is changed to:

$$2f_C\sigma_{ML} \ll 1 \quad (3.12)$$

It is clear from (3.12) that this requirement is independent of  $\psi_2$  and is only governed by  $f_C$ . As a result, this constraint and the far-field condition can be simultaneously satisfied. Also, for  $\sigma_{ML} \simeq 0.1$  ps, center frequency values up to 500 GHz are still within the boundaries of (3.12), facilitating access to high-fidelity  $\mu$ -wave, MMW and sub-THz RF-AWG territory.

Moreover, in the next section, we show that our proposed RF-AWG scheme can actually achieve the upper bound TBWP limit ( $N$ ), showing that this is the first design (to our knowledge) that successfully engineers programmable RF waveforms with time-bandwidth products equal to the upper bound given by the number of spectrally resolved pulse shaper control elements (*resolution elements*). This is a direct result of creating the center frequency fringes of the desired signal using optical interferometry, which liberates the pulse shaper to devote all of its resolution elements solely to passband modulation features.

### 3.3 Numerical Analysis

To strengthen the mathematical evaluations provided in the previous section, appropriate numerical analysis, incorporating the Fresnel integral, is presented in this section. Although various waveforms are demonstrated, the main concentration is directed

toward two classes of interesting waveforms, specifically ultrabroadband continuous frequency-chirped electrical pulses, as well as wideband frequency-hopped spread spectrum (FHSS) sequences. To match our experimental apparatus (the results of which will be presented in later sections), we have assumed that the ML-laser covers the full optical C-band (5 THz bandwidth from 1520 nm to 1560 nm); the pulse shaper also spans the C-band with 10 GHz spectral resolution and 1 GHz addressability; and in most cases, ~25 km of Single-Mode Fiber (SMF) acts as the quadratic dispersive element with dispersion value of 393.6 ps/nm (i.e.,  $\psi_2 = -501.67 \text{ ps}^2$ ).

Note that here we distinguish between pulse shaper resolution and addressability: addressability refers to the frequency sweep across individual spatial light modulator pixels, whereas resolution refers to the minimum feature size that can be imprinted onto the output spectrum, limited by the finite optical spot size at the spatial light modulator plane. Distinguishing the difference between these two parameters allows us, in later sections of this report, to push the upper bound for TBWP, while accepting lower signal powers. In all simulations, the smooth phase and amplitude functions are represented as stair-step waveforms with 1 GHz steps (matching the 1 GHz addressability of the physical device); these are then convolved with a 10 GHz Gaussian to account for the finite spectral resolution, using Eq. (8.34) from [52].

### 3.3.1 Ultrabroadband Continuous Frequency Chirps

Generating microwave and millimeter wave continuous frequency-chirped pulses is desirable for high-resolution radar and sensing systems as well as other applications like biomedical imaging and physical chemistry [53-56]. Chirped pulses not only have the advantage of high temporal resolution similar to ultrashort electrical pulses, but they also

avoid many design issues like saturation and amplifier nonlinearity at the transmitter end. This is why the generation of this class of waveforms, specifically ultrabroadband linear frequency-chirps, has been an attractive research topic for various groups working on signal design.

In the first simulation, we study the generation of an ultrabroadband linear frequency-chirped pulse across a desired center frequency using our introduced technique. We aim to attain signals with the best possible compression ratio (i.e., the most compressed autocorrelation), which is directly proportional to the TBWP criterion of the generated waveform. It must be noted here that TBWP is also equal to the processing gain (for signal power) when a matched filter equivalent to the generated chirp is created. Fig. 3.2 shows the temporal and spectral representations for a simulated example. The delay variable is set to  $\tau = 189$  ps to realize a center frequency of  $f_c = 60$  GHz, while a spectral phase function of  $\angle H(\tilde{\omega}) = 2e^{-24}\tilde{\omega}^2$  rad is programmed onto the pulse shaper.

The instantaneous frequency information in Fig. 3.2(a) is defined based on the following definition:

$$f_{inst}(t) = \frac{1}{2\pi} \frac{d}{dt} \phi_{RF}(t) \quad (3.13)$$

where  $\phi_{RF}(t)$  is the temporal phase function of the generated RF waveform, corresponding to (3.11b) in radians and  $f_{inst}(t)$  has units of inverse seconds (or Hz). It is clear from the instantaneous frequency plot of Fig. 3.2(a) that the generated signal is a smooth constant-amplitude linear downchirp. This matches perfectly with our expectations, since from (3.11b) the temporal frequency of the desired waveform is proportional to the derivative of the applied pulse shaper phase function.

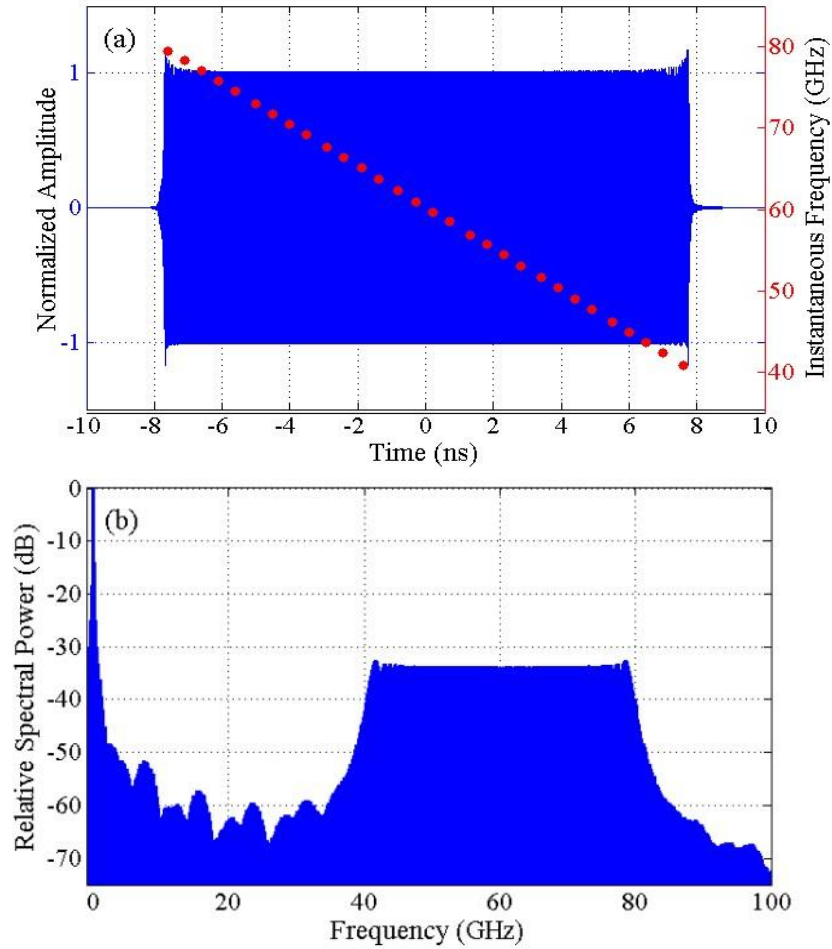


Figure 3.2: Ultrabroadband linear frequency downchirp simulation result – (a) DC-blocked temporal waveform ( $e_{des}$ ) and instantaneous frequency (b) Power spectrum of photodetected waveform ( $e_{PD}$ ).

It is necessary to note that the applied phase function is constrained by the finite spectral resolution, as explained in [46,52]. The finite spectral resolution results in a phase-to-amplitude conversion effect, which introduces an attenuation that becomes important when the spectral phase varies too rapidly (hence when the target RF frequency offset becomes too large). In the simulation reported here, we chose a quadratic phase function resulting in a maximum phase jump of  $\pi/8$  for adjacent 1 GHz-spaced addressable pixels,

corresponding to  $5\pi/4$  variation per 10 GHz resolution element. This value matches that used in our experiment reported in later sections and is selected based on the amount of amplitude attenuation we could practically tolerate and still be able to flatten out (equalize) the spectrum and then amplify back to adequate power levels at acceptable signal-to-noise. The equalization step is performed using the same pulse shaper by taking advantage of its programmable amplitude, which (aside from spectral resolution constraints) can be programmed independently of phase. In simulating this equalization, the shaper addressability and resolution are accounted for in the same way as described before.

From Fig. 3.2, the resultant photodetected signal has a time duration of 15.75 ns and a 3-dB bandwidth of 38 GHz, making the TBWP of the simulated linear frequency-chirped pulse 598.5. This value is, as expected, in the proximity of the maximum achievable TBWP using the aforementioned pulse shaper resolution (5 THz bandwidth divided by 10 GHz resolution yields 500 resolvable elements). The precise value of achievable TBWP depends on the amount of phase-to-amplitude conversion one is willing to accept in the experimental implementation.

These simulation results support our claim that the proposed interferometric scheme should provide TBWP twice that of what can be realized using conventional FTM methods [46]. The interferometric scheme provides further advantage for passband signals. This is due to the fact that, as elaborated in the previous section, for conventional, baseband FTM-based RF-AWG, the maximum TBWP is only achieved for a signal spanning from DC to the highest frequency generated. So, if one aims to generate a passband signal, quite a lot of TBWP will be sacrificed. To be more clear, in the case of the target signal spanning

from 41 GHz to 79 GHz (the result of our simulation in Fig. 3.2), the maximum TBWP that baseband FTM methods can achieve is roughly:

$$\frac{500}{2} \times \frac{38 \text{ GHz}}{79 \text{ GHz}} \simeq 120.25 \quad (3.14)$$

Therefore, in this specific example our proposed method achieves nearly 5 times more TBWP in comparison with baseband FTM-based RF-AWG schemes, including near field frequency-to-time mapping [24].

### 3.3.2 Wideband Frequency-Hopped Spread Spectrum Sequences

Another very interesting set of waveforms with applications in radar engineering, imaging and communications are FHSS sequences. A criterion often used for evaluating the compression performance of FHSS sequences is the auto-ambiguity function, defined as below [57,58]:

$$\chi(f, \tau) = \left| \int e(t) e^*(t - \tau) e^{-j2\pi ft} dt \right|^2 \quad (3.15)$$

This function not only measures the compression of a pulse in the time domain (corresponding to range), but also in frequency (corresponding to Doppler). The advantage of wideband implementation of these signals using our technique is that we allow the user to effortlessly design the range and velocity resolution within a wide span of values without any significant setup modification.

Table 3.1: Length 15 Costas sequence.

<b>Frequency Hop Sequence Ordering</b>
4, -3, 3, -5, -4, 0*, -2, -6, 1, 6, 5, 7, 2, -1, -7

\* Zero denotes no frequency shift

In this work we have chosen an FHSS sequence from a family of sequences proven to have optimal (thumbtack) auto-ambiguity compression. These frequency-coded signals are called Costas sequences and have a broad extent of applications in high-resolution ranging, detection and synchronization [57,58]. Here, a Costas sequence of length 15 and fundamental frequency of 1 GHz is created about a 30 GHz carrier frequency. This corresponds to programming a piecewise linear phase on the pulse shaper and setting  $\tau$  equal to 94.5 ps. The harmonic ordering for this sequence is tabulated in Table 3.1.

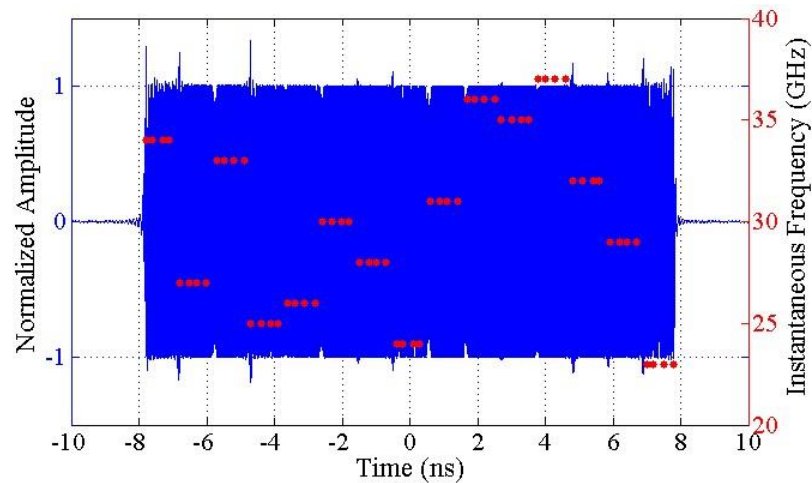


Figure 3.3: Wideband Costas sequence simulation result – DC-blocked temporal waveform ( $e_{des}$ ) and instantaneous frequency.

Fig. 3.3 illustrates the Costas sequence simulation results. Clear transitions in temporal frequency are observed about the 30 GHz frequency range. A practically flat amplitude is also visible for this signal, although it should be noted that the slight amplitude overshoots at the transitions are due to the finite resolution of the pulse shaper, which has been taken into account in all simulations.

### 3.4 Experimental Implementation and Results

In order to realize our proposed scheme experimentally, the system configuration should be enhanced to incorporate issues like power handling, stabilization, polarization matching, dispersion compensation, and noise reduction. Fig. 3.4 shows the resultant detailed experimental setup. The signal generation path is illustrated from left to right, starting at an erbium-doped fiber ring mode-locked laser and ending at a high-speed photodetector. The ML laser has a repetition rate of  $\sim 53$  MHz and spans 1520 nm to 1610 nm. In order to match the bandwidth to that of the pulse shaper, we added a home-made optical bandpass filter to sift out only the C-band (5 THz optical bandwidth) from the mode-locked laser output and flatten out the optical spectrum. An erbium-doped fiber amplifier and a polarization controller follow before pulses enter the interferometric shaping subsystem.

The interferometric shaping subsystem is composed of polarization maintaining (PM) components so as to prevent polarization drift and eliminate the need for polarization matching. A commercial PM pulse shaper (Finisar 1000SP) with spectral resolution of  $\sim 10$  GHz spanning the full optical C-band operates as the means for arbitrary waveform generation. Also, for stability purposes, a piezo-electric transducer (PZT) is implanted within the interferometer to act as an actively controllable fiber stretcher. The output pulses from the interferometric shaping subsystem are stretched in  $\sim 25$  km of SMF (total dispersion of  $\sim 393.6$  ps/nm) and amplified again before beating on a high-speed 50 GHz photodetector. All measurements are made using a 70 GHz digital sampling oscilloscope with  $50\Omega$  input impedance.

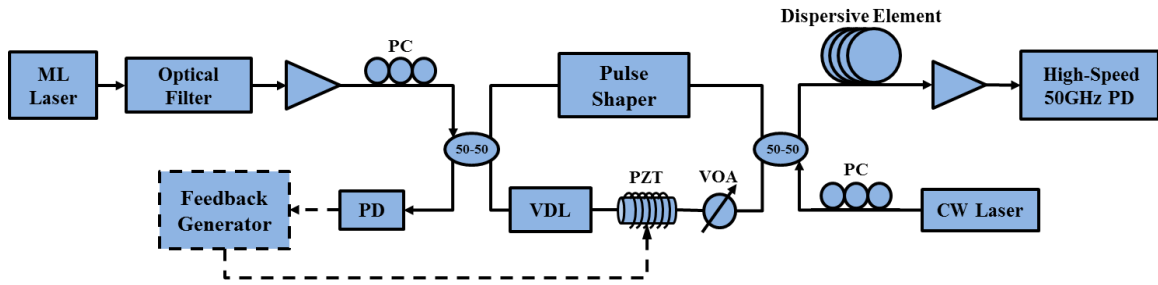


Figure 3.4: Detailed experimental setup.

The interferometer stabilization path flows from right to left inside the same configuration (shown beneath the generation path in Fig. 3.4). Details of the stabilization procedure and its components are explained in the next subsection.

### 3.4.1 Experimental Setup Stabilization

Regardless of the application, an optical interferometer requires modifications in order to enhance its stability against vibrations and relative temperature fluctuations between the two arms. It is usually important to maintain a constant phase difference between the two interfering arms. From our point of view, the main drawback of an unstable phase difference inside the interferometer is the repeatability of the generated waveforms. For instance, in spread spectrum settings, the compressibility of a series of wideband chirped signals is of great importance. This can be achieved using real-time or offline auto- and cross-correlation [57,58]. If the created waveforms are consistently repeatable, pulse compression can be implemented using only one stored copy of the sequence. However, in the presence of an unstable phase difference, either phase tracking must be implemented via digital signal processing or every single sequence element must be recorded, imposing substantially increasing system complexity.

In order to overcome issues arising due to unstable phase fluctuations, we resort to a simple feedback stabilization technique [59]. As depicted in Fig. 3.4, an independent CW optical wave, followed by a polarization controller, is fed into the interferometer from the opposite direction as a probing signal. By taking the opposite propagation direction, we have effectively allow frequency overlap between our CW signal and the mode-locked spectrum; while at the same time avoiding the need for extra optical filtering. The CW signal travels through the interferometer from right to left and after coupling out of the  $2 \times 2$  50-50 coupler impinges on an ordinary photodetector. The bandwidth of this photodetector is  $\sim 1$  GHz, which is more than adequate for detecting the slowly varying phase fluctuations in our setup, which if not compensated alter the photodetected intensity.

Using appropriate electrical feedback components and the piezo-electric fiber stretcher (PZT), we lock this intensity to a constant value and thus accomplish interferometer stability. With this improvement, we are able to stabilize the interferometer and achieve repeatable waveform results without RF phase drift, as shown in the following subsections.

### 3.4.2 Ultrabroadband Continuous Frequency-Chirps

In this subsection, we demonstrate waveforms similar to those simulated in Section 3.3, but reduced to  $f_c = 25$  GHz (corresponding to a delay of roughly 78.75 ps) in view of the frequency response of our photodetector. In order to create the linear chirping function, we apply the same phase-only function on the pulse shaper, i.e.,  $|H(\tilde{\omega})| = 1$  and  $\angle H(\tilde{\omega}) = 2e^{-24}\tilde{\omega}^2$ .

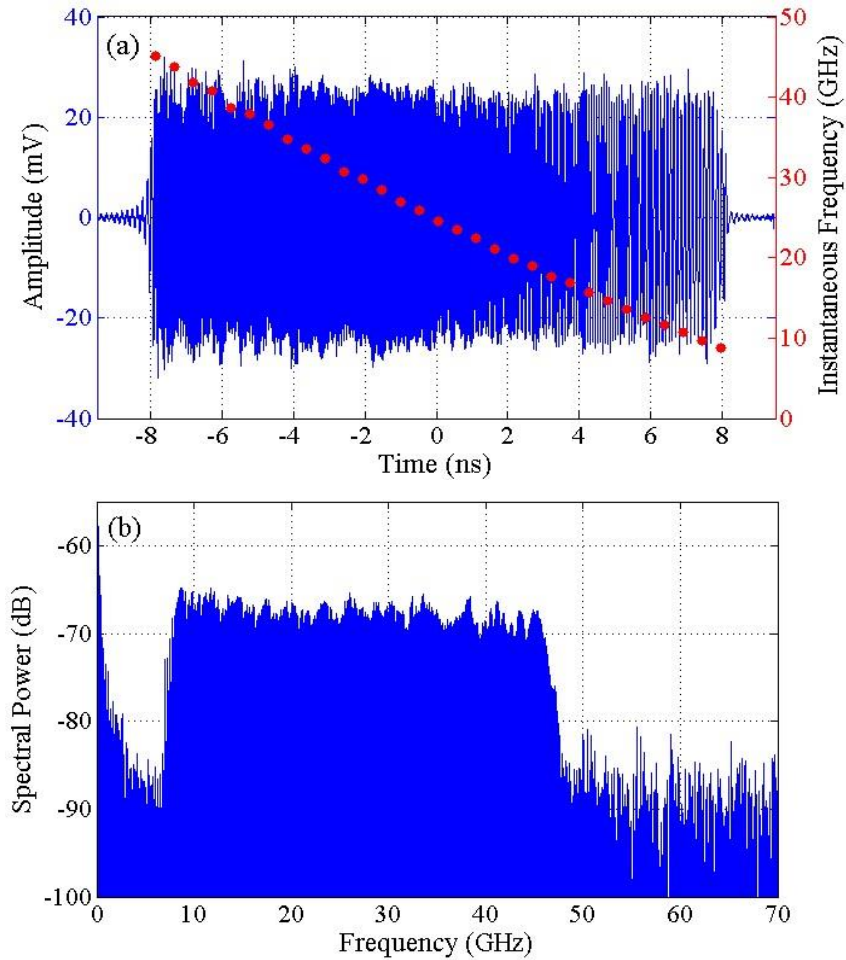


Figure 3.5: Ultrabroadband linear frequency downchirp experimental result – (a) DC-blocked temporal waveform ( $e_{des}$ ) and instantaneous frequency (b) Power spectrum.

Fig. 3.5 displays the temporal and spectral results for this experiment. The DC-blocked signal – denoted by  $e_{des}$  in our analytical evaluations – is depicted in Fig. 3.5(a) alongside its instantaneous frequency plot; while Fig. 3.5(b) shows the corresponding power spectrum of the total photodetected waveform. In addition to phase shaping, the pulse shaper is used to equalize the effect of phase-to-amplitude conversion, explained earlier, as well as spectral ripple present on the input laser and optical amplifier

nonuniformities across the spectrum. As a result the very flat temporal amplitude observed in Fig. 3.5(a) is obtained. Such spectral amplitude control can be further exploited for implementing applications like windowing and sidelobe suppression [57].

We remark that, the slight curve in the instantaneous frequency in Fig. 3.5(a) is due to higher-order dispersion (mainly 2<sup>nd</sup>) in the 25 km SMF and agrees with dispersion specifications of the fiber and experimental parameters published in [61]. We show in the next subsection that our scheme can also allow us to compensate for this undesirable higher-order dispersion and achieve a truly-linear downchirp.

From Fig. 3.5, the demonstrated waveform has a pulse duration of  $\sim 15.75$  ns and a 3-dB bandwidth of  $\sim 37.4$  GHz, yielding a total TBWP of  $\sim 589$ . As anticipated, this number is in the vicinity of the number of programmable spectral resolution elements on the aforementioned pulse-shaper.

Next, we show the repeatability of these engineered waveforms. In order to do so, 750 samples of the generated waveform in Fig. 3.5 were taken once every 10 seconds over the time period of approximately 2 hours. Fig. 3.6 displays the overlay of all the different samples from this batch. The waveforms are so closely similar that no distinction is apparent in a full scale view. Thus, Figs. 3.6(a) and 3.6(b) each show a zoomed-in view at the higher and lower frequency parts of these signals. Clearly, there are only very minor temporal distinctions between various sample waveforms. This leads to an average correlation coefficient [62] of 99.31% over all the 750 sample signals, while without stabilization, the correlation is extremely low due to the effects of RF phase drift.

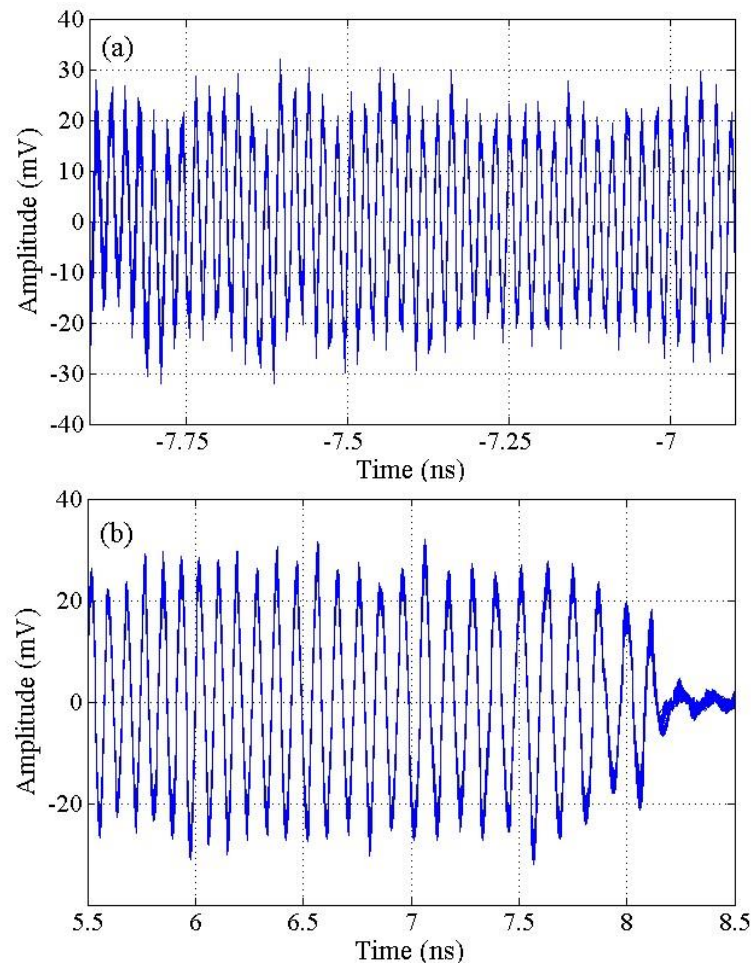


Figure 3.6: Overlaid temporal representation of 750 different sample measurements of the ultrawideband linear frequency downchirp in Fig. 3.5(a) – Zoomed-in views at (a) higher frequency region (b) lower frequency region.

From the cross-correlation perspective, this repeatability is even more evident since it shows that the still-existing minute temporal dissimilarities between different sample waveforms have insignificant effect when it comes to the compressibility of the different signals. Fig. 3.7 contains cross-correlation plots of all 750 waveforms with respect to a common reference. It is evident from the indistinguishable curves in this figure that all 750 signals have been successfully compressed from  $\sim 16$  ns to less than 30 ps and all

correlation plots match the autocorrelation of a single waveform very well. Also, a processing gain of  $\sim 27.7$  dB (i.e.,  $10 \log_{10}(589)$  power gain) is achieved through matched filtering using this signal. In other words, no distinct sign of cross-correlation distortion, peak displacement, attenuation or flipped polarity is witnessed.

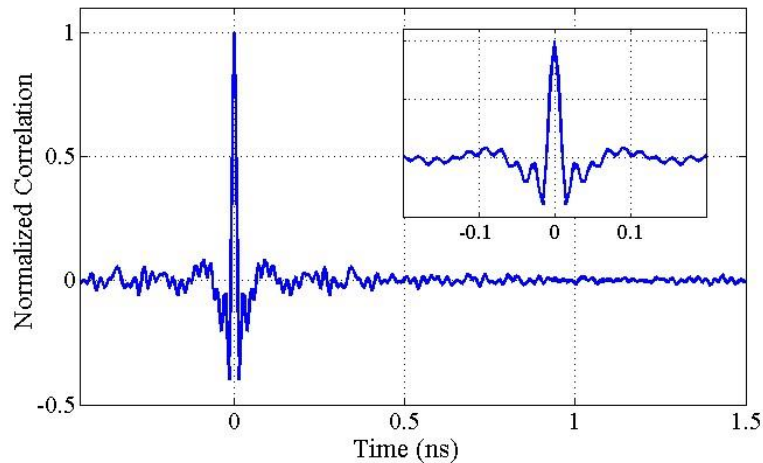


Figure 3.7: Overlaid cross-correlation plots of 750 different sample measurements of the ultrawideband linear frequency downchirp in Fig. 3.5 with respect to a common reference.

To further demonstrate the versatility of the presented technique, we have provided the result of two other experiments to implement other chirp functions. Fig. 3.8(a) illustrates a concave quadratic chirp across the 20-30 GHz frequency range. This signal can be created by merely applying a predefined 3<sup>rd</sup>-order phase function on the pulse shaper and adjusting VDL. Finally, Fig. 3.8(b) shows a down-chirp with sinusoidal frequency modulation [60].

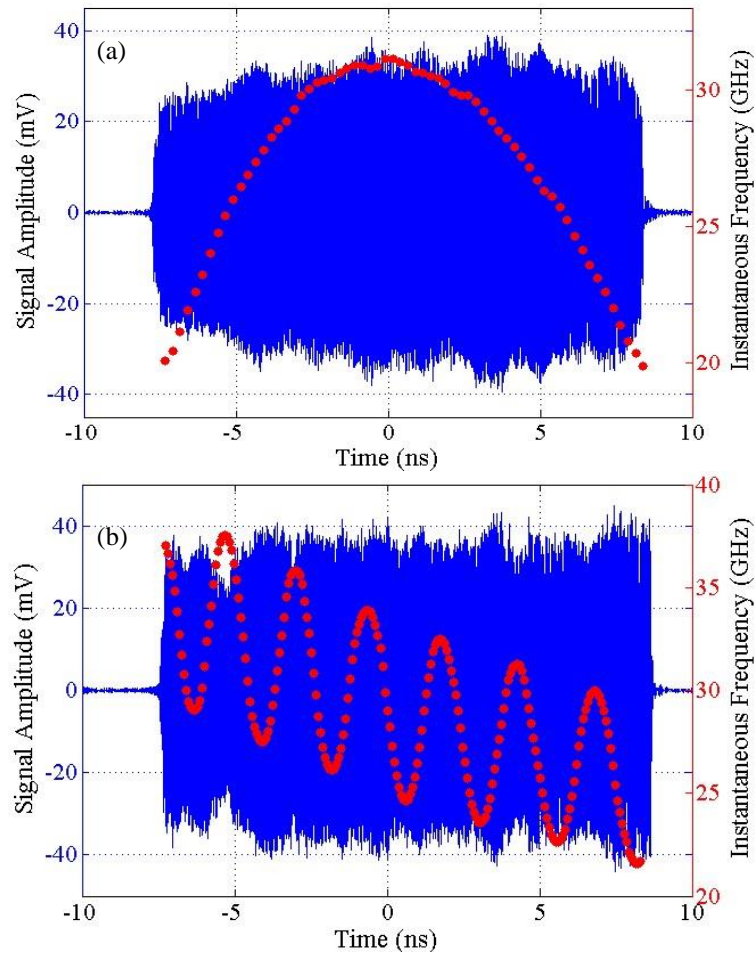


Figure 3.8: Overlaid cross-correlation plots of 750 different sample measurements of the ultrawideband linear frequency downchirp in Fig. 3.5 with respect to a common reference.

### 3.4.3 Higher-Order Dispersion Compensation

In the previous subsection we presented clear results regarding repeatable frequency-chirped waveforms with large TBWP values. However, as observed from Fig. 3.5(a), these chirps were not truly linear and did not agree 100% with our numerical analysis. This is apparent in the slight curve in the instantaneous frequency plot of Fig. 3.5(a). The main reason for this phenomenon is the existence of higher-order dispersion in

our experimental dispersive element block. In this section we show the capability of our proposed RF-AWG configuration to compensate these unwanted higher-order dispersion effects and experimentally achieve truly linear frequency-chirps.

As we discussed in our theoretical analysis, perfect frequency-to-time mapping requires the use of a purely 1<sup>st</sup>-order (quadratic phase) dispersive element. Nevertheless, since we are utilizing regular SMF for FTM, it is also expected that one observes the effect of a certain amount of higher-order dispersion. Based on the specifications of the utilized fiber spool as well as previous experimental analysis in our group on the same fiber [61], we expect this higher-order dispersive effect to be dominated by 2<sup>nd</sup>-order dispersion (cubic spectral phase).

Fig. 3.9(a) shows the spectrogram plot of a sample waveform generated from our setup without dispersion compensation, using the following definition of spectrogram [52]:

$$S_e(f, \tau) = \left| \int e_{des}(t) \cdot g(t - \tau) e^{-j2\pi ft} dt \right|^2 \quad (3.16)$$

where the gate function,  $g(t)$ , was chosen to be a Gaussian pulse with 500 ps pulse duration.

Ideally, in the presence of purely 1<sup>st</sup>-order dispersion, the waveform is expected to exhibit precise linear chirping behavior. The slightly arched chirping function of this waveform can be numerically calculated using the dispersion slope parameter (only cubic spectral phase) of the SMF spool. This expected instantaneous frequency curve is plotted on top of the spectrogram, accompanied by its time-varying instantaneous frequency function (time in ns and frequency in GHz). The extreme resemblance of these two curves verifies that, in agreement with our prior anticipations, the undesirable higher-order dispersion of our fiber spool is dominated by 2<sup>nd</sup>-order dispersion.

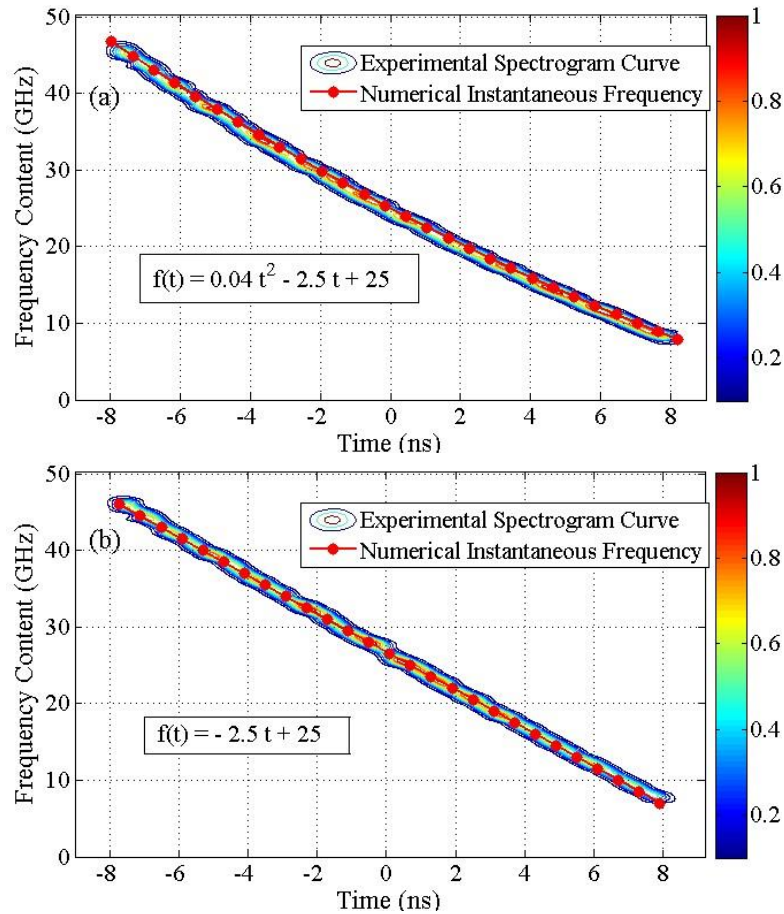


Figure 3.9: Experimental spectrogram curve and numerical instantaneous frequency of (a) Uncompensated linear frequency chirp (b) Dispersion compensated truly-linear frequency chirp.

Fig. 3.9(b) shows the result of compensating for the 2<sup>nd</sup>-order dispersion of the SMF spool as well as the numerical results for instantaneous frequency. In order to accomplish this dispersion compensation, an extra cubic phase was programmed onto the pulse shaper arm of our setup. This cubic phase was chosen to exactly complement the cubic spectral phase due to the 2<sup>nd</sup>-order dispersion of the SMF and ensure accurate FTM after passing through. From Fig. 3.9(b), one can observe that the quadratic temporal frequency term has

been entirely eliminated within the precision of our measurement. Moreover, it should be noted that our compensation scheme is not limited to residual cubic phase; our configuration allows compensation of any higher-order residual spectral phase function within the spectral resolution limits of the pulse shaper.

#### 3.4.4 Wideband Frequency-Hopped Spread Spectrum Sequences

In this experiment we show the possibility of utilizing the proposed RF-AWG technique to generate Costas sequences. Here, we specifically implement the length 15 Costas sequence described in Section 3.3.2 and Table 3.1.

In this test, the carrier frequency is set at  $f_C = 10$  GHz to emphasize the tunability of the delay parameter in our setup and allow better visualization of the results; while the fundamental frequency of the sequence is 1 GHz to match the results from simulation. In order to realize this sequence, we apply a piecewise linear phase function onto the pulse shaper, where the slope of each section is proportional to each specific harmonic of the Costas array. Of course, as mentioned in the previous subsection, some minor phase compensation is necessary to pre-compensate higher-order dispersion effects.

Fig. 3.10 shows the corresponding unwrapped phase function applied to the pulse shaper. It can be recognized from this figure, that at larger harmonic deviations, larger slope values must be implemented. Due to the finite pulse shaper resolution, this creates slight attenuation at high harmonics as a result of the phase-to-amplitude conversion effect [52]. These slight attenuations at high frequency deviations can be compensated for by applying some attenuation (no more than 2dB) at other optical frequency regions using the amplitude function of the same pulse shaper.

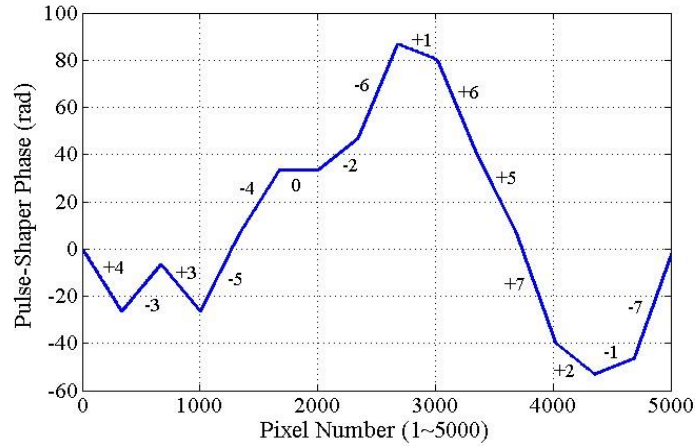


Figure 3.10: Applied unwrapped phase for Costas experiment and corresponding frequency harmonics (Actual phase applied to pulse shaper is modulo  $2\pi$ ).

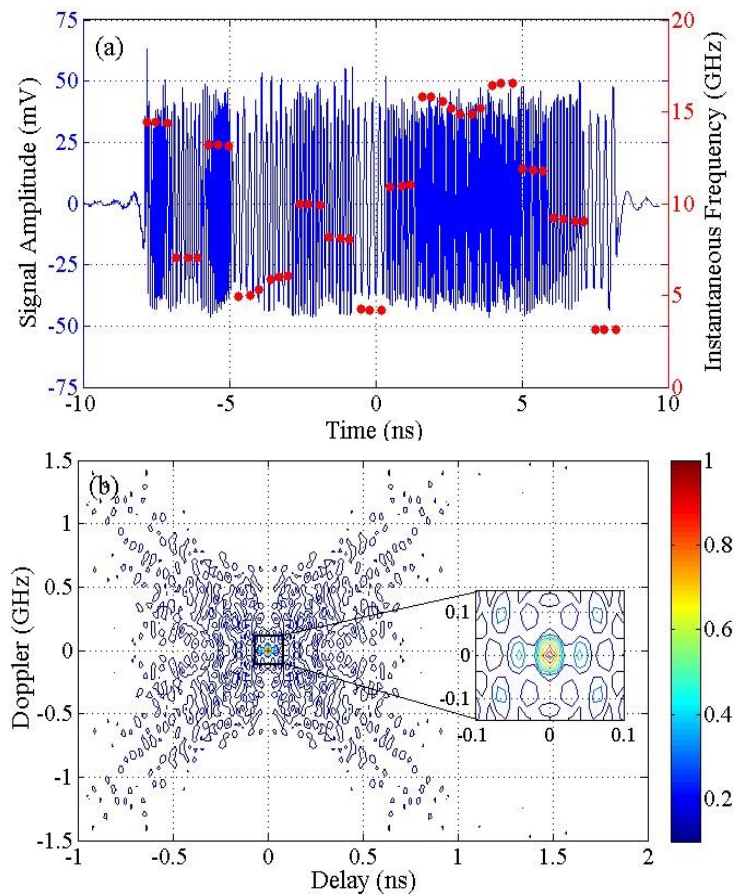


Figure 3.11: Wideband Costas sequence experimental result – (a) DC-blocked temporal waveform ( $e_{des}$ ) and instantaneous frequency (b) Normalized contour plot of autoambiguity function versus delay and Doppler.

Figure 3.11 shows the generated 16ns-long waveform for this experiment. In Fig. 3.11(a), the sequence is overlaid with its instantaneous frequency plot versus time. An almost smooth amplitude is distinctly visible, although as predicted, slight overshoots are present at discontinuities in the pulse shaper phase function. It is clear that the transitions are close to what we expect; spaced out evenly in time and frequency. To further show the performance characteristics of the generated Costas signal, its auto-ambiguity function was calculated offline. Fig. 3.11(b) shows this normalized auto-ambiguity, calculated using (3.15). This function resembles the nice thumbtack ambiguity that is expected from the Costas sequence. The main lobe of the auto-ambiguity function has a full-width half-maximum (FWHM) of  $\sim 15$  ps in delay and  $\sim 36$  MHz in Doppler. It must be noted that the relatively coarse Doppler resolution is as expected due to the still small temporal duration of the signals implemented [57,58]. As shown in later chapters, this RF-AWG technique can be combined with the waveform switching scheme presented in [63] to increase the repeat-free temporal duration of the generated signals from nanoseconds to microsecond and even millisecond scale. This should enable much finer frequency resolution, potentially below the KHz level, of interest for many practical applications.

## **4. ENABLING HIGH-SPEED DATA MODULATION FOR RF-ARBITRARY WAVEFORM GENERATION AND APPLICATION IN TIME APERTURE EXPANSION**

### **4.1 Introduction**

As elaborated in previous chapters, the main underlying component in all FTM-based RF-AWG schemes, including our novel interferometric technique, is an optical pulse shaper. Optical pulse shapers are well-developed, commercially available with very high resolutions, and often consist of an array of liquid crystal spatial light modulators (SLMs). Although spectral tailoring techniques based on fiber grating structures or simple on-chip optical pulse shapers have also been recently demonstrated [64-69], in most implementations spectral shaping is indeed carried out using SLMs, usually based on liquid crystal technology [70,71]. By manipulating the drive voltage to these liquid crystal modulators, the optical properties of each pixel is changed, resulting in the spectral shaping of the input optical waveform. Although current pulse shapers are programmable in both amplitude and phase, their update speed is relatively slow (on the order of milliseconds), making them incompatible with most practical data modulation rates. Thus, photonic-assisted RF-AWG techniques require some other means of restructuring in order to implement the additional option of high-speed data modulation or waveform update [72].

RF-photonic techniques have also been extensively utilized to enable high-speed and high-complexity data modulation for wired/wireless communications, especially in the

MMW and sub-terahertz frequency regimes [12, 73-75]. These systems typically modulate two or more appropriately-spaced optical carriers in order to implement data modulation on single/multiple RF carriers at high frequency bands. Nevertheless, the combination of high-speed data modulation and RF-arbitrary waveform generation has seen little attention.

Enabling high-speed data modulation on the generated RF-AWG waveforms not only allows the possibility of high-speed data communications over ultrabroadband channels, but also offers potential for utilizing these programmable waveforms in applications such as long-range unambiguous radar and covert wireless communications with high coding gains in highly dispersive and multipath environments. As an example, our group has previously reported a technique that utilizes two optical pulse shapers and allows high-speed binary data modulation of photonic-assisted RF-AWG, with experimental demonstrations of their applications in highly-dispersive ultrabroadband RF channel sounding and high resolution RF ranging exhibiting an extended non-ambiguous range [63, 76,77].

In this chapter, in Section 4.2, we first introduce a novel modification to our presented interferometric RF-AWG setup, enabling high-speed phase and amplitude modulation capability on the individual ultrabroadband RF arbitrary waveforms. This scheme was originally introduced by us in a publication in *Optics Express* in 2015 [72]. This data modulation scheme is completely independent of the RF-AWG stage, allowing immediate incorporation of real-time data modulation on the generated RF waveforms. In Section 4.3, we report direct experimental measurements of these phase- and amplitude-modulated ultrabroadband waveform sequences with frequency content from ~2 GHz to ~52 GHz, spanning more than 4.7 octaves.

In the last section, we utilize the new data modulation capability of our RF-AWG setup and present a novel pseudo-random phase coding scheme that circumvents the small time aperture limitation of photonics-based RF-AWG systems [27]. Regular photonics-based RF-AWG setups typically generate waveforms with time durations from a few hundreds of picoseconds up to several tens of nanoseconds, which is too short for many applications like unambiguous ranging. To overcome this issue, in this section, we present a simple photonics-based pseudorandom phase-coding scheme resulting in time aperture expansion of the generated RF arbitrary waveforms. This capability allows an increase in the nanosecond-level time aperture achieved by conventional photonic-assisted RF-AWG schemes to several microseconds and beyond, with corresponding increase in time-bandwidth product. This strategy is mathematically proven and experimentally implemented on ultrabroadband chirps spanning  $\sim 2$  to  $\sim 52$  GHz. These results were originally discussed in our publication in the *IEEE Journal of Quantum Electronics* in early 2016 [27].

## 4.2 Setup Configuration

The schematic for our modified RF-AWG system is depicted in Fig. 4.1. Similar to the setup of Fig. 3.1, the system consists of an ultrafast pulsed laser source, an optical interferometric subsystem, a quadratic dispersive element, and a high-speed PD. However, in this design the optical interferometer has a dual utility. The bottom arm of the interferometer includes the high-resolution optical pulse shaper and variable optical delay line (VDL) that provide RF-arbitrary waveform generation. The top arm includes high-speed optical phase and intensity modulators (PM and IM), which are used to achieve

programmable phase and amplitude modulation on individual RF waveforms within the generated sequence. Although similar results can be achieved using an optical in-phase/quadrature (I/Q) modulator, here we simply consider an IM and PM already available in our laboratory in series. Two independent electrical pattern streams, synchronized with the repetition rate of the optical source, are utilized to apply multilevel sequences to drive the optical modulators. Since at this stage the optical pulses are very short (less than a few hundred femtoseconds) and have not stretched through dispersive fiber, reasonable amounts of timing jitter (less than a few hundred picoseconds) in the electrical patterns driving the IM/PM pair should have little effect on the waveform generated.

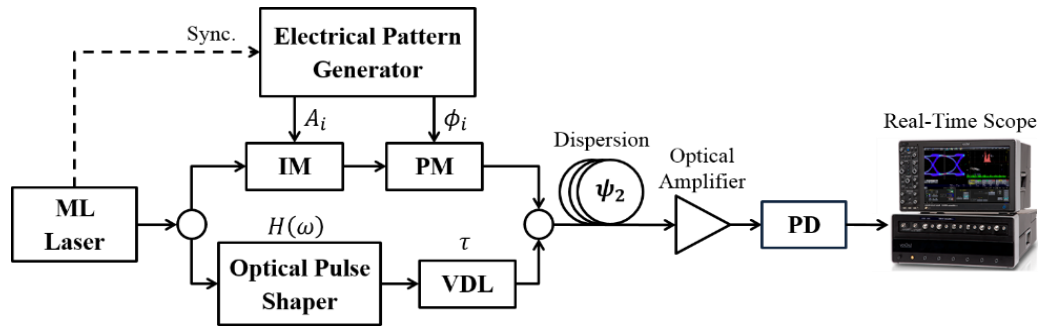


Figure 4.1: Schematic for modified interferometric RF-AWG scheme.

According to the mathematical analysis provided in Chapter 3, in the far-field limit, the passband generated RF waveform,  $e_{RF}(t)$ , has the following profile:

$$e_{RF}(t) \propto \sum_i A_i \cdot \left| H \left( \frac{-(t - iT)}{\psi_2} \right) \right| \cdot \cos \left( \frac{(t - iT)\tau}{\psi_2} - \angle H \left( \frac{-(t - iT)}{\psi_2} \right) - \phi_i \right) \quad (4.1)$$

where  $H(\tilde{\omega}) = |H(\tilde{\omega})|\angle H(\tilde{\omega})$  is the pulse shaper spectral transfer function,  $T$  is the pulsed laser repetition period,  $\tau$  is the variable delay,  $\psi_2$  is the value of dispersion and the  $A_i$ 's and  $\phi_i$ 's are individual elements of the amplitude/phase sequences encoded using the IM/PM pair. Additional baseband terms at the output of the PD are assumed to be filtered using a high pass RF filter and the excess constant phase term (refer to Eq. (3.9)) is dropped from this equation for simplicity.

As observed from (4.1),  $e_{RF}(t)$  is a sequence of phase- and amplitude-modulated programmable RF waveforms with the same repetition rate as the pulsed laser. The center frequency and temporal profile of the waveform is set according to the relations described in Chapter 3 Eq. (3.11). Furthermore, the driving voltages to the modulator pair control the relative phase and amplitude of each individual waveform within the generated sequence, independent from the RF-AWG stage. That is, the design of the arbitrary waveform, its center frequency, and an overall complex digital data modulation are controlled independently. This feature allows the simple implementation of various complex data modulation sequences, by adjusting the signal patterns driving the modulator pair. It is important to note that the effect of the modulators only appears in the amplitude and phase modulation parameters,  $A_i$  and  $\phi_i$ , and does not modify the RF-AWG process.

In the following section we present experimental results demonstrating generation of ultrabroadband RF-arbitrary waveforms with frequency content up to  $\sim 52$  GHz and spanning more than 4.7 octaves. We then overlay high-speed programmable data modulation, choosing as examples M-ary phase shift-keying (PSK) and quadrature amplitude modulation (QAM), in both cases with up to 16 levels (4 bits) per symbol. Although the center frequency and bandwidth of the generated RF waveforms can be easily

scaled either to higher (with appropriate photodetection technology) or lower values, in this work we choose to show results that achieve the largest frequency content consistent with our available experimental equipment (photodetector and waveform digitizer).

### 4.3 Experimental Results

In these experiments, we utilize a self-referenced mode-locked fiber laser (Menlo Systems FC1500-250-WG) with 250 MHz repetition rate and 15 dBm average power as the pulsed source. The pulses from this laser cover the full optical C-band (1525-1565 nm), which is also the operating range of our high-resolution optical pulse shaper (Finisar 1000SP) which features 1 GHz addressability and  $\sim 10$  GHz resolution. The optical phase and intensity modulators each have a modulation bandwidth of  $\sim 10$  GHz with a half-wave voltage of 2.9 V and 3.5 V at 1 GHz, respectively. The output pulses from the interferometric subsystem are stretched in  $\sim 6$  km of single-mode fiber (SMF with total dispersion of  $\sim 100$  ps/nm) and amplified (to  $\sim 10$  dBm average power) in an erbium-doped fiber amplifier before beating on a high-speed photodetector ( $\sim 52$  GHz 3-dB bandwidth). The length of fiber is precisely chosen such that the generated RF arbitrary waveforms each span the available 4 ns time aperture, set by the repetition rate of the ML laser. Finally, the RF waveform is filtered with a 50 kHz high pass filter and measured on a 65 GHz real-time oscilloscope with  $50\Omega$  input impedance.

#### 4.3.1 Ultrabroadband Chirp Generation

First, we provide experimental results for the case where no modulation is applied, i.e.,  $\phi_i = 0$  and  $A_i = 1$  for all indices. Figure 4.2 illustrates a 60 ns-long measurement result for an ultrabroadband linear down-chirped RF waveform sequence, generated by

applying a quadratic phase function in the pulse shaping stage, as well as compensating for the excess higher-order dispersion of the SMF spool [46]. Each individual signal has a time duration of  $\sim 4$  ns, while covering a 50 GHz 3-dB bandwidth from  $\sim 2$  GHz to  $\sim 52$  GHz, or equivalently  $\sim 4.7$  octaves frequency span. Here, the average generated RF power is  $\sim -0.45$  dBm, which can be increased by amplifying more at the optical amplification stage and using a photodetector with higher optical power handling. The chirped pulses have a repetition rate of 250 MHz, equal to that of the ML laser. The spectrogram of a single 4ns-long waveform from Fig. 4.2(b) is calculated offline using a 200 ps Gaussian gate function and plotted in Fig. 4.2(c), showing close-to-perfect linearity of the RF waveform's instantaneous frequency versus time.

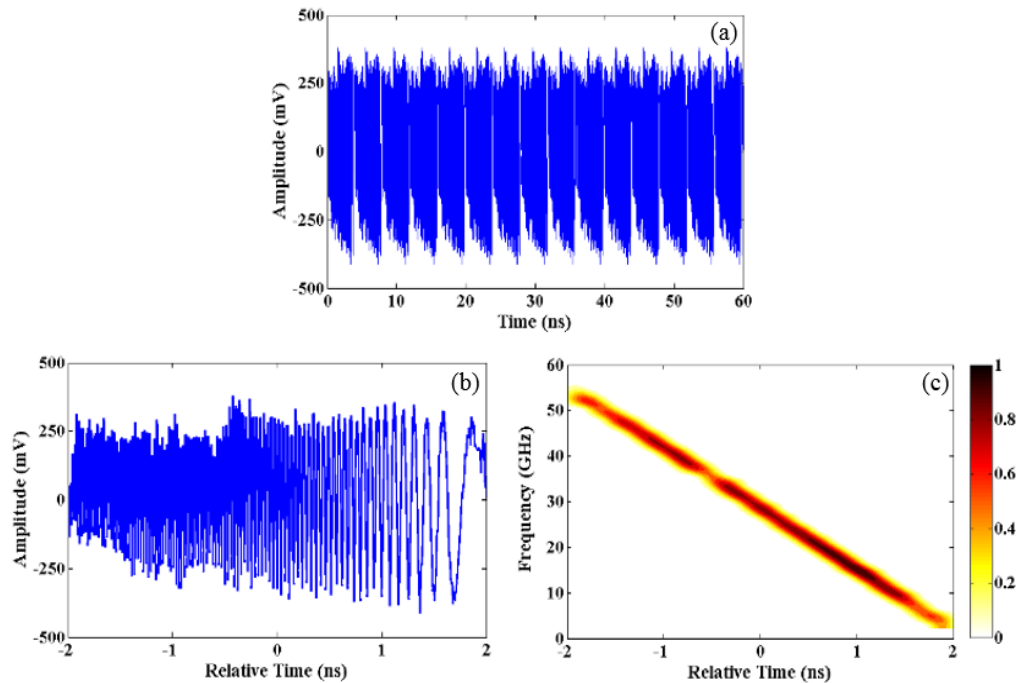


Figure 4.2: Periodic repetition of ultrabroadband linear down-chirp waveform. (a) 60 ns-long real-time measurement of the generated sequence. (b) Temporal profile of an individual 4 ns-long, 50 GHz bandwidth RF chirp. (c) Normalized spectrogram plot of an individual RF chirp.

In the next subsections we demonstrate sequences in which the ultrabroadband linear down-chirp waveform of Fig. 4.2 is repeated, now adding programmable phase and amplitude modulation synchronized to the waveform repetition period.

### 4.3.2 Programmable Phase Modulation

To demonstrate programmable phase modulation, the  $A_i$  values are all set to 1 by biasing the IM at maximum transmission. Figure 4.3 shows the results of modulating a four-level drive signal to the PM in order to achieve  $0^\circ$ ,  $90^\circ$ ,  $180^\circ$  and  $270^\circ$  phase shift on the waveform of Fig. 4.2. To provide a clear illustration of the phase modulation effect, this figure includes zoom-in views to two 0.3 ns-long frames of the generated waveforms.

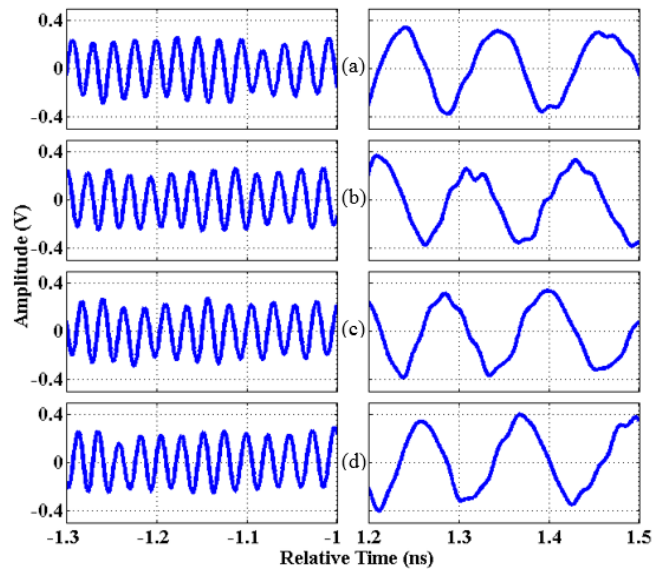


Figure 4.3: Zoom-in views of the generated ultrabroadband RF waveforms with (a)  $0^\circ$ , (b)  $90^\circ$ , (c)  $180^\circ$ , and (d)  $270^\circ$  phase shift.

It is worth mentioning that through the use of a high-speed PM, we can arbitrarily set the relative phase of individual waveforms within the generated RF sequence, independently, as expected from the derivation in (4.1).

This phase modulation capability allows us to implement various phase-shift keying (PSK) schemes on the generated programmable RF waveforms. Figure 4.4 shows the measurement result for a binary-PSK (BPSK) data modulation experiment using this scheme. In this experiment, the ultrabroadband linear down-chirps of Fig. 4.2 are randomly modulated at 250 Mbps by a binary sequence of length 1000. A color-coded 60 ns window of the resultant 4  $\mu$ s-long measurement is plotted in Fig. 4.4(a), while Fig. 4.4(b) shows, within the same time range, the electrical data signal driving the optical phase modulator (normalized to the corresponding  $V_\pi$ ). To clearly observe the 180° phase shifts between the generated antipodal BPSK signals, two individual anti-phase chirps are overlaid in the plot of Fig. 4.4(c), alongside zoom-in views.

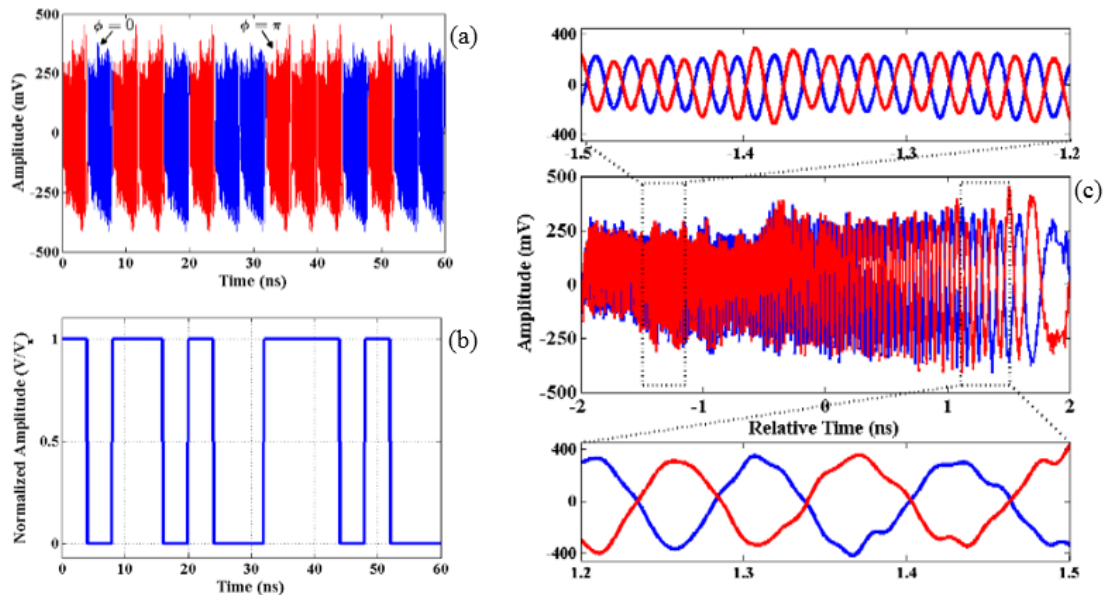


Figure 4.4: Ultrabroadband BPSK measurement results – (a) Color-coded 60ns window of 4 $\mu$ s-long BPSK sequence. (b) Normalized bi-level electrical signal at the input of the phase modulator ( $V_\pi = 2.9$ V). (c) Overlay of generated antipodal chirps and zoom-ins.

To demonstrate higher-order modulation, we also carried out various experiments for quadrature-PSK (QPSK) and 16-level PSK on the same ultrabroadband signal. In all experiments, we use a length 1000 M-ary data sequence to drive the PM. For example, QPSK is accomplished by applying 4-level data sequences to switch between the waveforms of Fig. 4.3. It must be noted that from the application perspective, this preprogrammed sequence can be replaced by a real-time data sequence to be directly modulated, as different symbols, on the ultrabroadband signal. Also, such higher-order modulation increases the communication data rate. Thus, our BPSK, QPSK and 16-PSK experiments have bit rates of 250 Mbps, 500 Mbps and 1 Gbps, respectively (1, 2, and 4 bit per symbol multiplied by the 250 MHz symbol rate).

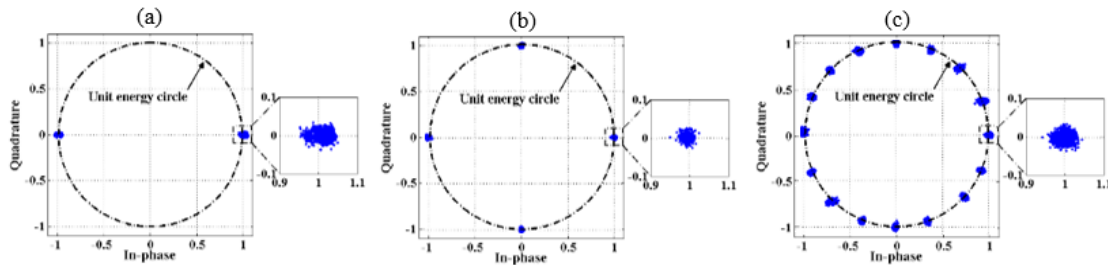


Figure 4.5: Calculated signal constellations from long real-time measurements of various PSK scenarios and zoom-ins: (a) BPSK, (b) QPSK, (c) 16-PSK.

To test the quality of ultrabroadband PSK modulation, we process the  $4\mu\text{s}$ -long PSK sequence measurements to yield constellation plots, shown in Fig. 4.5. Each data point in these plots is the result of offline decoding of the amplitude and phase of each 4ns-long chirp in the PSK sequence. The amplitude of each waveform is derived by computing the square root of its total energy and normalizing it by the average computed amplitude over all waveforms in the sequence. To obtain the phase, we first assign zero phase to a reference

waveform from the sequence. Then, for each chirp, we run an iterative procedure to decode the phase. In each step, we apply a constant phase shift to the chirp in the Fourier domain. Then, the phase-shifted signal is cross-correlated with the reference in the time domain and the peak value of cross-correlation is stored. This process is continued with a phase step of  $0.5^\circ$  from  $0^\circ$  to  $360^\circ$ . Finally, the inverse of the phase shift value that provides the maximum cross-correlation peak is assigned as the decoded phase of the each specific waveform. The constellation plot results indicate a high level of accuracy in phase shift keying modulation, with average error vector magnitudes (EVM [78]) over all the symbols calculated to be 2.36%, 2.01% and 3.22%, for BPSK, QPSK and 16-PSK, respectively. The slight errors are attributed to limitations in PM drive signal quality, noise induced in the optical amplification and photodetection stages, as well as a contribution from the real-time oscilloscope. Also, the small timing jitter between the two fiber-optic interferometer arms, may contribute slightly to the phase error. As discussed in Section 3.4.1 by implementing a feedback stabilizer system and piezo-electric fiber stretcher, this small amount of jitter can be even further suppressed to negligible values.

### **4.3.3 Programmable Phase and Amplitude Modulation**

Going beyond the phase-only modulation demonstrated in the previous section, the setup of Fig. 4.1 is capable of simultaneous phase and amplitude modulation. As an example Fig. 4.6 exhibits results for an 8-level rectangular quadrature amplitude modulation (QAM) experiment (3 bits per symbol). Figure 4.6(a) shows the modulated waveform over a 60 ns time interval (15 individual chirp waveforms) in which all the symbols from the 8-QAM constellation appear at least once. The individual waveforms in the sequence are labeled to indicate their amplitude and phase. The corresponding drive

signals to the IM and PM are normalized to the respective  $V_\pi$  values and plotted in Figs. 4.6(b) and 4.6(c). Note that the IM is initially biased at maximum transmission; and the IM drive signal of Fig. 4.6(b) corresponds to the extra voltage applied to the modulator in order to reduce the transmitted power for certain symbols. In contrast to the phase modulation case, the IM drive signal requires equalization to compensate for the nonlinearity of conventional optical IMs. Alternatively, the IM/PM pair can be replaced with a linear I/Q modulator to obtain similar results without the requirement of an equalization stage [79].

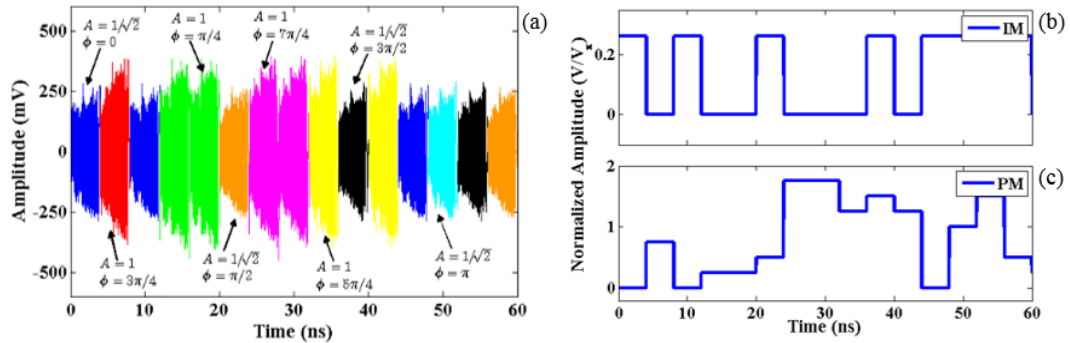


Figure 4.6: Ultrabroadband 8-QAM measurement results – (a) Color-coded 60ns window of 4 $\mu$ s-long 8-QAM sequence. (b) Normalized electrical drive signal at the input of the IM ( $V_\pi = 3.5\text{V}$ ), and (c) normalized electrical drive signal at the input of the PM ( $V_\pi = 2.9\text{V}$ ).

Similar to the previous section, we take a 4  $\mu$ s-long 8-QAM measurement and perform offline demodulation in order to plot the 8-point signal constellation in Fig. 4.7(a). Additionally, Figs. 4.7(b) and 4.7(c) show results for rectangular and circular 16-QAM experiments [80], both corresponding to four bits per symbol. The average EVM values over all symbols for Figs. 4.7(a)–(c) are 2.56%, 3.01% and 3.21 %, respectively. These error values show that the quality of the phase- and amplitude-modulated waveforms

remains similar to the quality of phase-only modulation results presented earlier. Also, increasing the number of constellation points in the modulated sequence does not seem to affect the phase and amplitude modulation quality and may potentially be extended beyond the 16 symbols shown. Clearly, however, signal-to-noise considerations will eventually limit the number of useful modulation levels.

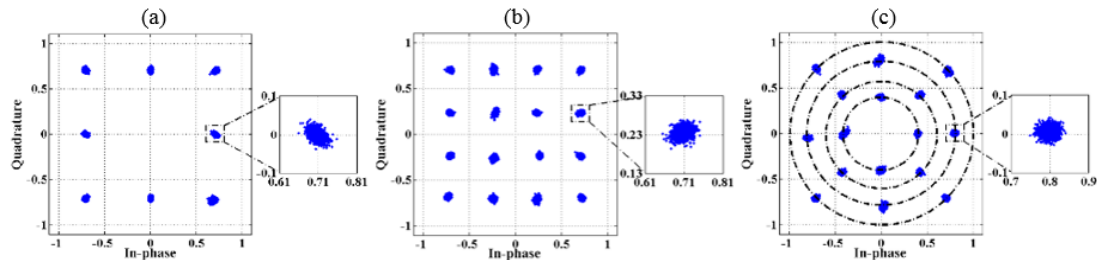


Figure 4.7: Calculated signal constellation plots from long real-time measurements of various quadrature amplitude modulation scenarios and zoom-ins: (a) Rectangular 8-QAM, (b) Rectangular 16-QAM, and (c) Non-rectangular (circular) 16-QAM.

#### 4.4 Time Aperture Expanded RF-AWG

As discussed earlier, although the TBWP capability of photonic-assisted RF-AWG schemes has now reached a level appropriate for some spread spectrum applications, photonic RF-AWG techniques still suffer from the problem of limited time apertures, typically in the low nanosecond range. This limitation inhibits the use of the generated waveforms in applications like long-range radar, Doppler radar, channel sounding and compensation of long communication channels, and more. Early examples of RF-photonic waveform generation work trying to address this issue are reported in [42,43], where line-by-line optical pulse shaping accompanied by ultrafast switching is utilized to construct frequency-hopped microwave pulses with indefinite record lengths and controllable RF

spectra. Recently, Y. Li et al. reported a novel photonic spread spectrum radio-frequency waveform generation technique that combines FTM-based RF-AWG and pseudo-noise (PN) waveform switching, implemented in the optical domain using an electro-optic modulator-based switch. This scheme increases the repeat-free time aperture of FTM-based RF-AWG essentially arbitrarily, up to several microseconds and beyond [63].

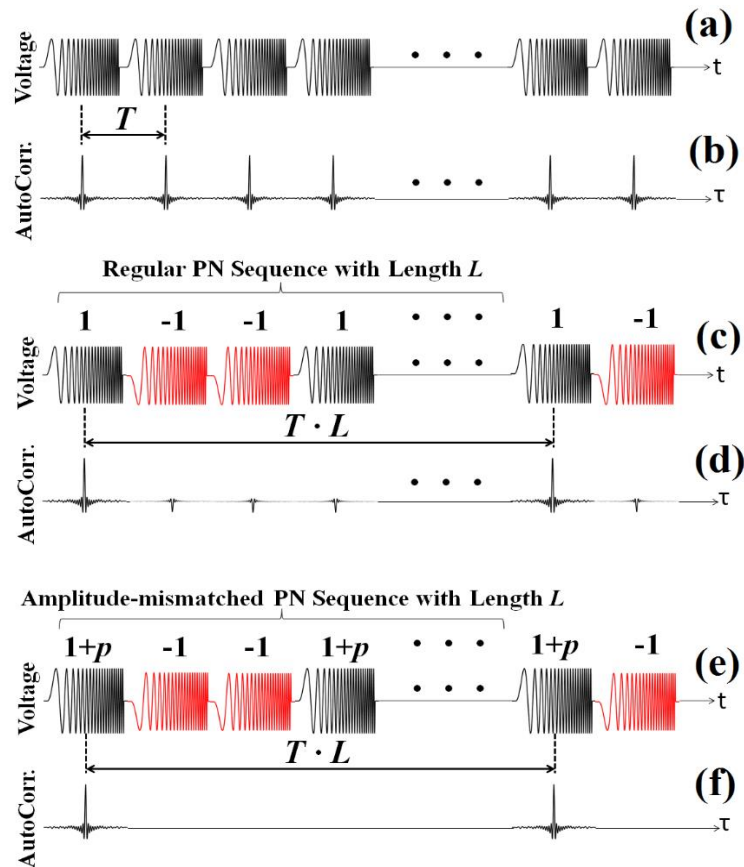


Figure 4.8: Schematic diagram of time aperture expansion RF-AWG, adapted from [63] – (a) Repetitive linear up-chirp waveform train with period  $T$ . (b) Autocorrelation function of (a). (c) Chirp train in (a) modulated by a length  $L$  regular PN sequence. Polarity of chirps is either maintained (black) or flipped (red). (d) Autocorrelation function of (c), spacing of  $T$  between low-power peaks. (e) Chirp train in (a) modulated by a length  $L$  amplitude-mismatched PN sequence. Peak-to-peak amplitude of the polarity-maintained chirps in (c) is adjusted to  $1+p$ , where  $p$  is a PN length dependent value. (f) Autocorrelation function of (e).

Figure 4.8 shows the principle of operation. In the absence of PN coding, the output of the photonic RF-AWG system is comprised of programmable RF waveforms (linear frequency chirped waveform for instance, as shown in Fig. 4.8(a)), constrained to repeat at the fixed repetition rate of the utilized ML laser ( $T$ ). Consequently, after pulse compression, achieved by autocorrelation, we observe short peaks occurring every  $T$  seconds, Fig. 4.8(b). When a length  $L$  binary PN sequence [80] is modulated onto such repetitive waveform (Fig. 4.8(c)), its repetition period can be extended to  $T \cdot L$ , which is the repeat period of the applied PN sequence. From the autocorrelation perspective, large autocorrelation peaks are now observed only at multiples of  $T \cdot L$ , while still there exists some small peaks with negative power at the original locations, Fig. 4.8(d). In [63], a mathematical relation is presented for a slight amplitude-detuning ( $p = 2/\sqrt{L + 1}$ ) of the applied PN sequence (the PN sequence now takes on values  $1+p$  and  $-1$ , as opposed to  $1$  and  $-1$  conventionally). This detuning factor allows the suppression of the residual unwanted peaks, achieving true expansion of the repeat-free time aperture, schematically seen in Figs. 4.8(e) and 4.8(f). As a result, tunable time aperture expansion is experimentally demonstrated for ultrabroadband microwave signals with frequency content of up to 20 GHz, from 4 nanoseconds up to several microseconds.

Although the described amplitude-detuned PN coding scheme allows arbitrarily-increased repetition periods, this scheme incurs some loss of power, especially when the length of the PN sequence is short. For example, to expand the repetition period by a factor of 15 results in a  $p$  value of  $1/2$ , corresponding to  $\sim 30\%$  average power decrease. This is a significant disadvantage for many applications, considering the peak-voltage limited nature of typical RF transmitters. To tackle this problem, in this section we propose a novel

time aperture expansion technique based on modulation of the basis waveforms by phase-detuned PN sequences.

#### 4.4.1 Principle

The principle of this technique is illustrated in Figs. 4.9(a) and 4.9(b). In addition to the polarity flipping sketched in Fig. 4.8(c), which is essentially a phase shift of  $\pi$ , here, a small phase detuning of  $\Delta\phi$  is additionally introduced. The phase-detuned PN sequence takes on phase values 0 and  $\pi + \Delta\phi$ , with constant amplitude.

In the next few paragraphs, we prove that this technique can allow ideal time aperture expansion, similar to what could be achieved using the amplitude-detuning technique of [63]. With this setting, residual unwanted autocorrelation peaks disappear, leaving only strong peaks separated by  $T \cdot L$ . We also show that this phase-detuned PN modulation scheme allows arbitrary expansion of the repetition period while preserving the average power of the output waveform under a peak-voltage-limited transmitter.

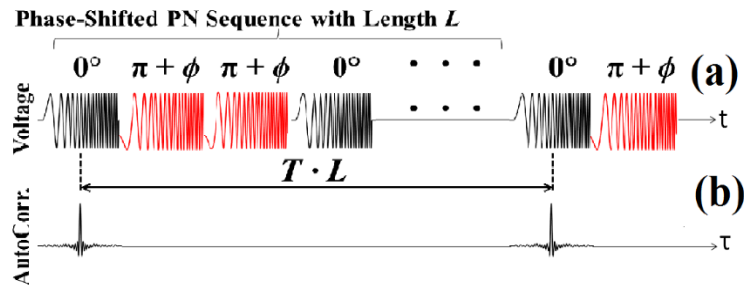


Figure 4.9: Schematic diagram of time aperture expansion RF-AWG via phase-detuning – (a) Chimp train in Fig. 4.8(a) modulated by a length  $L$  phase-shifted PN sequence. An excess phase shift of  $\Delta\phi$  is applied to antipodal waveforms. It is shown later that this value depends on the PN sequence length according to Eq. (4.9). (b) Autocorrelation function of (a).

We note that the implementation of the discussed phase-detuning can be simply carried out using the modified setup of Fig. 4.1 and by only taking advantage of the phase control via the embedded phase modulator.

Assuming a repeating optical pulse train from a pulsed laser source is fed into the generation setup, resulting in arbitrarily-tailored RF waveforms that repeat periodically at the laser repetition rate. This RF waveform sequence,  $s(t)$ , is expressed as:

$$s(t) = \sum_i w(t - iT) \quad (4.2)$$

where  $w(t)$  is the temporal profile of each spread spectrum waveform with circular autocorrelation function  $R_w(\tau)$ , and  $T$  is the repetition period. As a result, the autocorrelation function of  $s(t)$ ,  $R_s(\tau)$ , equals:

$$R_s(\tau) = \int s(t) \cdot s(t + \tau) dt = \sum_i R_w(\tau - iT) \quad (4.3)$$

It is important to mention that for the continuous RF signal,  $w(t)$ , the autocorrelation is defined as below:

$$R_w(\tau) = \int w(t) \cdot w(t + \tau) dt \quad (4.4)$$

Clearly from (4.4), we observe that in the absence of coding, due to the fact that  $w(t)$  is repeating itself with period  $T$ , the autocorrelation function of the total waveform is just a repetitive sum of the autocorrelation of a single waveform,  $w(t)$ . However, we may use simple coding schemes on each waveform to suppress these repeating autocorrelation peaks for a longer duration and combine the power into the main autocorrelation peak at zero delay [63]. Binary ( $\pm 1$ ) PN sequences of length  $L = 2^m - 1$  [80], have a thumb-tack like circular (or periodic) autocorrelation, i.e.:

$$\begin{aligned}
r_{PN}[m] &= \sum_{i=1}^L PN[i] \cdot \overline{PN}[(i+m) \bmod L] \\
&= \begin{cases} L & m = 0, \pm L, \pm 2L, \dots \\ -1 & \text{elsewhere} \end{cases}
\end{aligned} \tag{4.5}$$

where  $PN[i]$  is the binary pseudorandom sequence of repetition length  $L$ , and  $r_{PN}[m]$  is its discrete circular autocorrelation function. The bar sign in  $\overline{PN}$  denotes the complex conjugate function.

In order to modulate this sequence on the repetitive pulse sequence of (4.2), we must phase shift certain pulses by  $\pi$  according to  $PN[i]$ . However, that would result in a non-zero correlation floor with a value of -1, as seen in (4.5). In the following derivations, we prove that by detuning the phase shift slightly from  $\pi$ , we can achieve perfect autocorrelation with zero correlation floor. This modified phase-detuned PN sequence is referred to as  $PN'[i]$  and is composed as below:

$$PN'[i] = \frac{1 + e^{j\Delta\phi}}{2} PN[i] + \frac{1 - e^{j\Delta\phi}}{2} U[i] \tag{4.6}$$

where  $\Delta\phi$  is the constant phase detuning value in radians and  $U$  is a unit sequence of length  $L$  defined as  $U[i] = 1$ , for all  $1 \leq i \leq L$ . As a result,  $PN'[i]$  has the same pattern as  $PN[i]$ , but instead of having a phase shift of  $\pi$  at certain delay values, it exhibits phase shifts of  $\pi + \Delta\phi$ , making a complex-valued sequence.

After some mathematical calculations, the discrete circular autocorrelation of  $PN'[i]$  can be expressed as:

$$r_{PN'}[m] = \frac{1 + \cos \Delta\phi}{2} r_{PN}[m] + \frac{1 - \cos \Delta\phi}{2} r_U[m] + \frac{j \sin \Delta\phi}{2} r_{PN,U}[m] - \frac{j \sin \Delta\phi}{2} r_{U,PN}[m] \quad (4.7)$$

where  $r_{PN}[m]$  and  $r_U[m]$  are the discrete circular autocorrelation functions of  $PN[i]$  and  $U[i]$ , while  $r_{PN,U}[m]$  and  $r_{U,PN}[m]$  are the discrete circular cross-correlations between the two sequences. Since both  $PN[i]$  and  $U[i]$  are real-valued sequences, the last two terms in (4.7) cancel out. Also,  $r_U[m]$  is equal to  $L$  for all values of delay, thus plugging in (4.5) into (4.7) results in:

$$r_{PN'}[m] = \begin{cases} L & m = 0, \pm L, \pm 2L, \dots \\ \frac{1}{2}(L-1) - \frac{1}{2}(L+1) \cos \Delta\phi & \text{elsewhere} \end{cases} \quad (4.8)$$

Clearly, by appropriately choosing the phase detuning parameter, we are now able to create a zero floor at unwanted delays in (4.8). This is achieved at  $\Delta\phi$  given as follows:

$$\Delta\phi = \cos^{-1} \left( \frac{L-1}{L+1} \right) \quad (4.9)$$

If this sequence,  $PN'[i]$ , is utilized to modulate the phase of the generated spread spectrum pulse sequence, we can completely null the unwanted peaks, thereby achieving perfect time aperture expansion. The autocorrelation function of the new waveform,  $s'(t)$ , can now be expressed as:

$$R_{s'}(\tau) = \sum_i L \cdot R_w(\tau - iT) \quad (4.10)$$

Equation (4.10) indicates that the modulation perfectly increases the temporal repeat-free period of the new waveform by a factor of  $L$ . Also, the temporal profile of the basis waveform,  $w(t)$ , i.e., the temporal profile within a single period  $T$ , is not disturbed, leaving the RF bandwidth preserved. As a result, the spread spectrum waveform generation which controls the shape and RF bandwidth, and the PN modulation which determines the repeat-free time aperture, are kept independent while arbitrarily large TBWPs are realized.

In the next subsection, we utilize the setup of Fig. 4.1 and the above mathematical derivations for phase-detuning to experimentally demonstrate arbitrary time aperture expansion of ultrabroadband programmable RF waveforms spanning from  $\sim 2$  to  $\sim 52$  GHz.

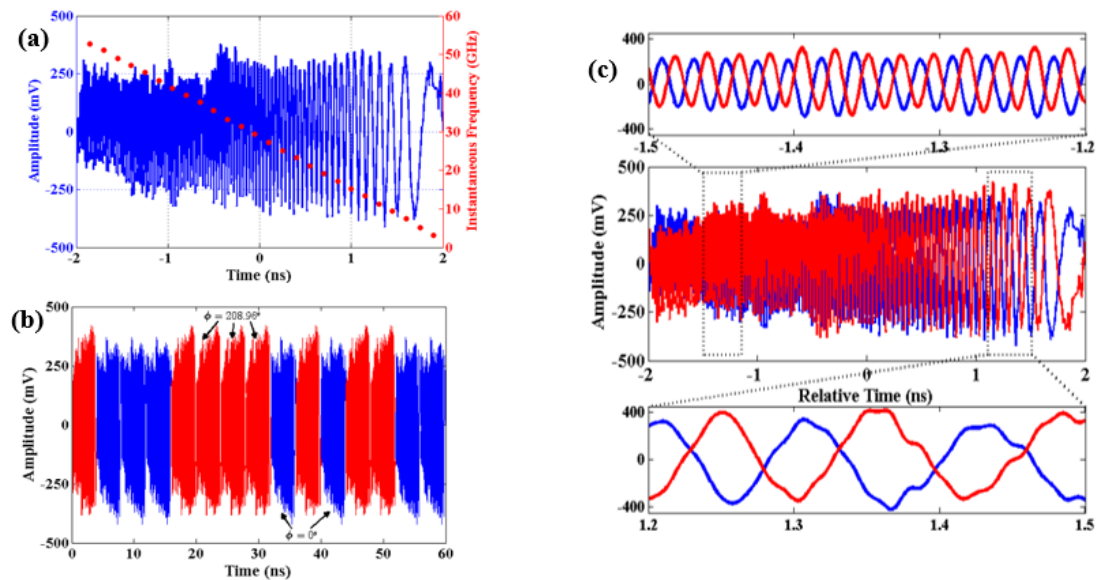


Figure 4.10: Measurement results of ultrabroadband linear down-chirp spanning 2-52 GHz – (a) Single waveform and its instantaneous frequency plot. (b) Color-coded 60 ns window of 180 ns-long measurement of length-15 phase-detuned PN coding according to Eq. (4.9). (c) Overlay of two phase-coded basis waveforms of (b) and zoom-in views.

#### 4.4.2 Experimental results

Previously, we showed the generation and measurement of phase- and amplitude-coded ultrabroadband signals covering the 4.7 octave frequency range of 2-52 GHz. Figure 4.10 shows the result of time aperture expansion using our novel phase-detuned PN coding scheme. In Fig. 4.10(a) a single ultrabroadband downchirp waveform along with its computed instantaneous frequency plot is illustrated. By applying a quadratic spectral phase function on the optical pulse shaper in the setup of Fig. 4.1, a linearly-decreasing frequency function is achieved across the center frequency of 27 GHz, which is set by tuning the VDL. In the absence of phase coding, this RF waveform repeats at the repetition rate of the ML laser (250 MHz), making the repeat-free time aperture 4 ns and the TBWP of the generated RF waveform 200 (50 GHz  $\times$  4 ns). To demonstrate time aperture expansion via the phase-detuned PN modulation technique, we program the pattern generator with a length 15 phase-detuned PN sequence and apply a phase detuning parameter of  $\Delta\phi = 28.96^\circ$ , as derived from (4.9). Figure 4.10(b) shows a color-coded 60 ns window of a 180 ns-long measurement for this experiment. The corresponding phase values for each basis waveform are also indicated in the figure. To provide a clearer observation, the two phase-coded basis waveforms from this sequence are overlaid in Fig. 4.10(c) along with zoom-in views. The detuning from a pure  $\pi$  phase modulation is easily observed.

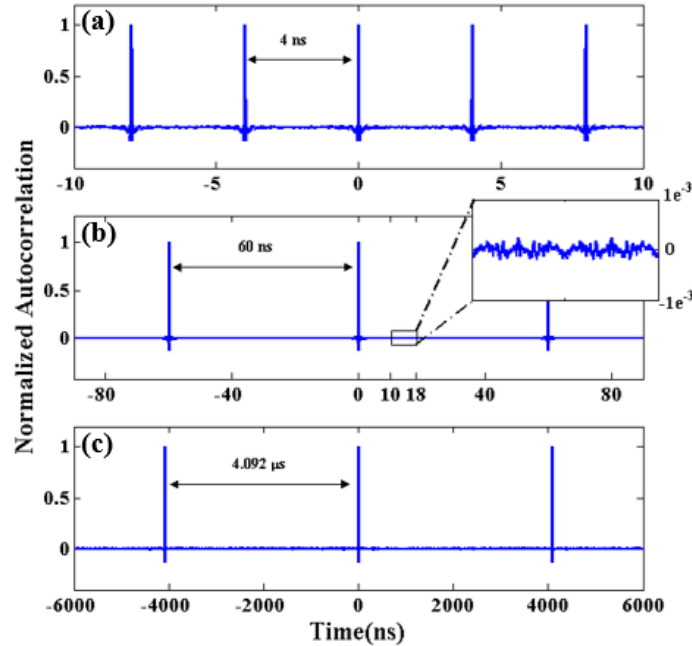


Figure 4.11: Normalized autocorrelation functions of generated ultrabroadband chirp sequences. (a) No Modulation, (b) Length 15 phase-detuned PN modulation, (c) Length 1023 phase-detuned PN modulation.

To evaluate temporal period expansion, we compute the circular autocorrelation of the 180 ns-long measurement as well as that of a same length measurement of RF-AWG in the absence of coding. In Fig. 4.11(a), the normalized autocorrelation of the unmodulated waveform has a period of 4 ns, the same as the laser repetition period. In contrast, as shown in Fig. 4.11(b), we have achieved an autocorrelation with strong peaks separated by 60 ns, corresponding to an increase in period by a factor of the PN sequence length (15 here). In the absence of phase detuning, we expect to observe weak autocorrelation peaks with a normalized amplitude of  $-1/15$  occurring every 4 ns. Consequently, a peak extinction ratio of  $\sim -11.76$  dB is anticipated. This value is defined as the ratio between the strongest amplitude of the remaining unwanted peaks and the strong peak at zero delay. However, as observed from the magnified view of Fig. 4.11(b), phase detuning suppresses these

peaks down to smaller than  $3e^{-4}$ , or equivalently  $\sim -35.23$  dB. To show the potential of increasing the repeat-free time aperture even further, we extend the length of the PN sequence and take real-time measurements of the generated waveforms. Fig. 4.11(c) is the computed autocorrelation function of the generated chirped waveform with a length-1023 phase-detuned PN sequence modulation. In this case, the time aperture is increased to more than 4 microseconds.

Lastly, it is worth noting that from the frequency domain perspective, time aperture expansion is equivalent to having a frequency spectrum with finer spaced modes, which can be utilized for high-resolution channel sounding experiments as well as Doppler radar [57,78]. For the examples of Fig. 4.11, the generated RF-AWG power spectra have frequency resolution of 250 MHz,  $\sim 16.67$  MHz and  $\sim 244.38$  KHz, respectively.

## **5. W-BAND ARBITRARY WAVEFORM GENERATION WITH ULTRA-HIGH TIME-BANDWIDTH PRODUCTS AND APPLICATION IN HIGH-RESOLUTION RANGING**

### **5.1 Introduction**

As mentioned in the previous chapters, until now, photonic-assisted RF-AWG methods have been confined to waveforms less than  $\sim 40$  GHz [24,46], mainly limited by photodetector technology; hence experimental results in higher frequency bands are largely absent. In Chapter 4, we introduced a novel passband RF-AWG that is inherently not limited to low frequencies and demonstrated some MMW generation examples. In this chapter, we aim to increase the frequency range of the generated RF-arbitrary waveforms to the 75-110 GHz, termed W-band, showing how this technique can be extended to much higher frequency ranges with advanced ultrahigh-speed photodetector technology [81-84].

Utilizing a specially-engineered high-power near-ballistic uni-traveling-carrier photodiode (NBUTC-PD) based photonic transmitter-mixer [84], we demonstrate the synthesis, wireless transmission and detection of arbitrary RF waveforms in the W-band enabled by our proposed photonic-assisted RF-AWG scheme. In doing so, we generate, for the first time, ultrabroadband waveforms covering the whole W-band region with a maximal time-bandwidth product (TBP) of 600 supported by the pulse shaping element. The generated waveforms are further analyzed in terms of repeatability and phase-noise; demonstrating phase-noise characteristics substantially superior to that of a state-of-the-art

electronic arbitrary waveform generator. Finally, as an application example, we demonstrate high-resolution ranging experiments that achieve range resolution down to an unprecedented 3.9 millimeters with potential for arbitrarily long unambiguous multi-target detection range, here demonstrated to over 5 meters (10 m round-trip). These results were originally published by us in *Optica* in late 2014 [77].

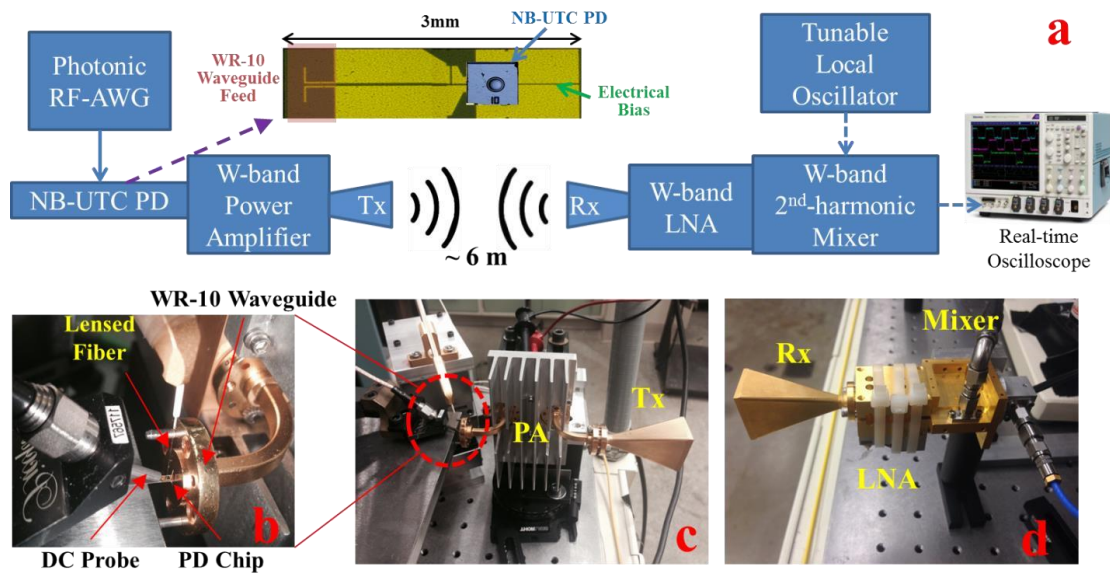


Figure 5.1: W-band experimental setup – (a) Schematic of waveform generation, transmission and measurement. NBUTC-PD: near-ballistic uni-travelling-carrier photodetector. Tx: transmitter antenna. Rx: receiver antenna. LNA: low noise amplifier. (b) Close-up of optical-to-electrical conversion block, followed by Tx feed. (c) Transmitter block. (d) Receiver block.

## 5.2 W-band Experimental Setup and Components

Figure 5.1 illustrates our W-band experimental arrangement. Optically-tailored waveforms from the photonic RF-AWG setup of Fig. 3.1 are directed to an NBUTC-PD based photonic-transmitter mixer (PTM) [85], Fig. 5.1(a). Here, the adopted PD with a

5  $\mu\text{m}$  active diameter has a 175 GHz optical-to-electrical (O-E) 3-dB bandwidth and saturation current of  $\sim 16$  mA. This component was provided to us as a result of a collaboration with National Central University of Taiwan (NCU), under the supervision of Prof. Jin-Wei Shi. The device also has an improved DC responsivity, now reaching  $\sim 0.25$  A/W, and saves the required optical power during high-output-power operation.

Detailed photographs of the PTM chip as well as the optical and electrical instrumentation apparatus are shown in Figs. 5.1(a)–(d). The PTM is embedded in a WR-10 waveguide feed to excite a W-band power amplifier followed by a horn transmit antenna (Tx). For the first experiment, the receiver side is placed  $\sim 6$  meters away in line-of-sight (LOS), where a receive horn antenna (Rx), W-band low noise amplifier (Millitech LNA10-02150, 20 dB gain,  $\sim 5$  dB noise figure) and 2<sup>nd</sup>-harmonic mixer (Virginia Diodes WR10SHM,  $\sim 17$  GHz bandwidth, 7 dB conversion loss) – driven by a local oscillator (Agilent E8257D-550) with frequency varied from 35 GHz to 50 GHz – are used to collect, amplify and down-convert the received waveforms and observe on our 20 GHz real-time oscilloscope (Tektronix DSA72004B).

### 5.3 W-band Arbitrary Waveform Generation

Using our novel interferometric RF-AWG scheme in our W-band configuration from Fig. 5.1(a), we program the pulse shaper to generate an ultrabroadband linear frequency-chirped electrical waveform from 110 GHz down to 70 GHz, encompassing the full W-band spectrum. To do so, a home-built erbium-doped fiber-ring mode-locked laser with  $\sim 53$  MHz repetition rate is used as the input source. Same as before, we utilize a commercial pulse shaper (Finisar 1000S) with spectral resolution of  $\sim 10$  GHz and

operating wavelength in C-band. The dispersive medium is simply a ~25 km spool of single mode fiber (SMF, total dispersion of ~393.6 ps/nm), resulting in a time aperture of ~16ns after FTM. In order to have a linear down-chirp covering 70-100 GHz, a quadratic phase-only function,  $\angle H(\tilde{\omega}) = 2e^{-24}\tilde{\omega}^2$ , is applied onto the pulse shaper; while the variable delay is set to  $\tau = 283.5$  ps, corresponding to a center frequency of 90 GHz.

Since the measurement apparatus only has ~17 GHz intermediate frequency (IF) bandwidth (mainly limited by the subharmonic mixer), the entire waveform cannot be measured at once. Consequently, different measurements of the same waveform using various local oscillator (LO) frequencies between 60 GHz to 100 GHz are separately obtained, 5 of which are depicted in Fig. 5.2(a). These down-converted pulses each contain partial information about the generated signal and are the principal tools for reconstructing the complete W-band chirp.

Each LO measurement is digitally up-converted to its corresponding frequency, aligned in phase via offline processing, and combined with the other measurements to reconstruct the whole generated W-band linear down-chirp. Although the synthesizer LO frequencies are highly precise, their relative phases are not controlled. This results in phase misalignment in the down-converted waveforms measured with different LO frequencies. In order to be able to correctly combine these measurements to reconstruct the total waveform, phase alignment is required. This is carried out off-line by iteratively phase shifting each measurement (other than the first) and maximizing its cross-correlation with the first (reference) measurement. It is important to reemphasize that the need for phase alignment results only from the lack of phase synchronism of the free-running LO that we tune to different frequencies and is not inherent to the generation scheme itself.

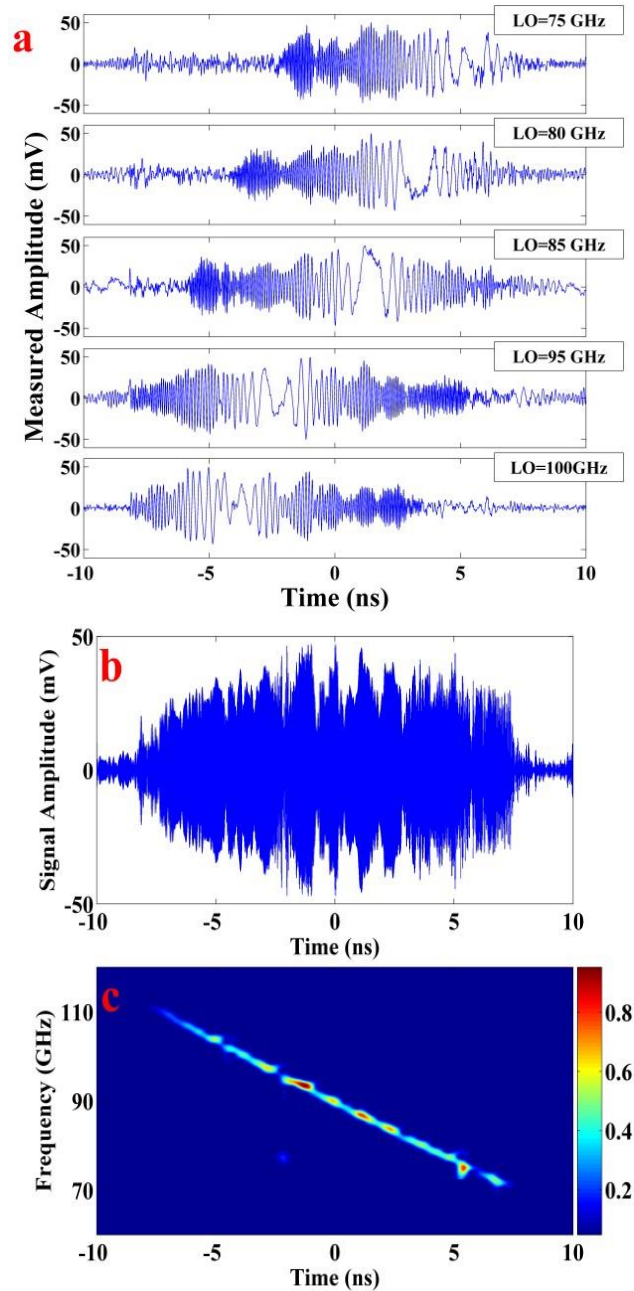


Figure 5.2: W-band RF-arbitrary waveform generation – (a) Down-converted measurements using various local oscillator (LO) frequencies. (b),(c) Reconstructed W-band waveform and spectrogram of ultrabroadband linear down-chirp.

The final reconstructed W-band chirp is illustrated in Fig. 5.2(b). The signal stretches over  $\sim 15$  ns time aperture, consistent with the  $\sim 40$  nm optical bandwidth and  $\sim 394$  ps/nm dispersion. The slight amplitude fluctuations are mainly due to the spectral ripple in the optical domain, which in principle may be equalized using the pulse shaper's attenuation control. Furthermore, the spectrogram of the generated ultrabroadband chirp is plotted in Fig. 5.2(c). Here, the close-to-linear down-slope of the spectrograms clearly indicates the ability to achieve the target frequency chirp in the W-band, covering 70-110 GHz. As a result, a TBP of  $\sim 600$  ( $40\text{GHz} \times 15\text{ns}$ ) is achieved in this experiment. Compared to previous demonstrations in the W-band [86-88], to our knowledge, this is the first experimental demonstration of achieving arbitrary waveforms with such high TBP values, while covering the full W-band spectrum.

As we showed in the previous chapters, the utilized scheme is not limited to chirp generation and can be reconfigured to attain truly arbitrary waveform generation. To demonstrate this capability, a wideband Costas sequence implementation is also carried out in the W-band. The length-15 Costas sequence has a fundamental frequency of 1 GHz and is created about a 90 GHz ( $\tau = 283.5$ ) carrier frequency. The harmonic ordering for this sequence is tabulated below:

Table 5.1: Length 15 Costas sequence.

<b>Frequency Hop Sequence Ordering</b>
7, 0*, -3, -5, 5, -7, -4, 2, 1, 3, 4, -1, 6, -2, -6

\* Zero denotes no frequency shift

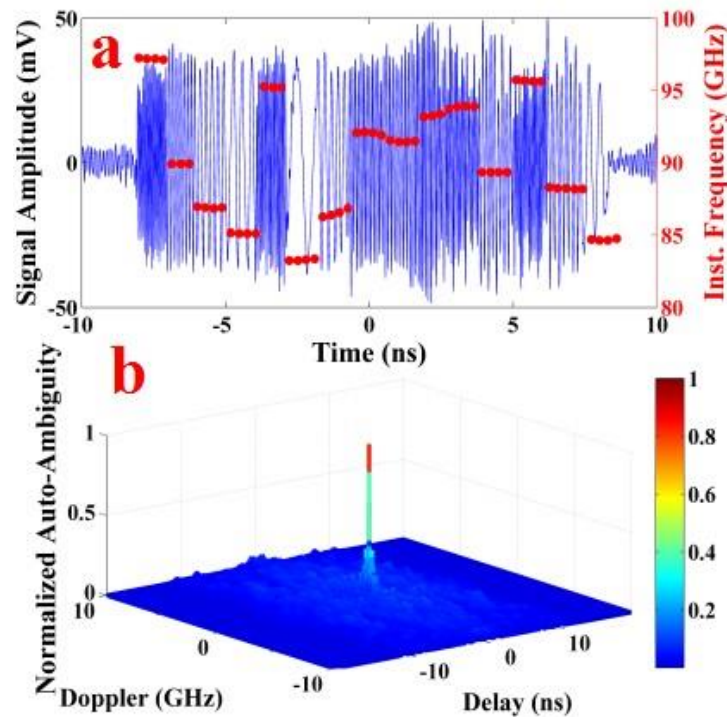


Figure 5.3: W-band Costas Implementation – (a) Reconstructed frequency-hopped Costas sequence (plotted in baseband) and corresponding instantaneous frequency. (b) Computed auto-ambiguity function of the waveform in (a).

Figure 5.3(a) illustrates the reconstructed temporal profile of this waveform; plotted after down-conversion to baseband for clear observation of frequency transitions alongside its instantaneous frequency. Clear frequency transitions accompanied by a nearly flat temporal profile are observed. The waveform's auto-ambiguity function is also computed and plotted in Fig. 5.3(b). The desirable property of a sharp thumbtack-shaped auto-ambiguity function is clearly observed in Fig. 5.3(b). Also, the main lobe of the auto-ambiguity has a full-width-half-maximum (FWHM) of 15 ps in delay and 36 MHz in Doppler. We note that in this experimental implementation the relatively coarse frequency resolution is a direct result of the short (nanosecond scale) time aperture of the generated

pulses, limited in part by the repetition period ( $\sim 18.9$  ns) of the mode-locked laser at the front end, rendering it unsuitable for unambiguous long-range sensing and detection. However, by utilizing the time aperture expansion scheme of Chapter 4, one may achieve much finer frequency resolution, with time aperture selectable up to microseconds and beyond, which accommodates many practical applications.

#### **5.4 W-band RF-AWG Phase-Noise Analysis**

From the application point of view, strong repeatability and low jitter are major requirements for the generated waveforms. Several experiments have investigated the special case of photonic-assisted generation of MMW frequency chirp waveforms, either by beating a CW laser with a second CW laser subject to rapid frequency tuning [87,88] or with a mode-locked pulse chirped under dispersive propagation [25]. However, the repeatability of the resulting waveforms is compromised, either due to the poor frequency sweep stability in the former case or due to phase drifts between the short pulse and CW lasers in the latter. Furthermore, phase-noise characteristics have not been reported for either scheme. In contrast, our approach - presented for the W-band - benefits from both the excellent repeatability of FTM-based OAWG approaches [35,89], as we showed before, and from the low jitter potential of mode-locked laser sources [90,91].

In order to evaluate the phase-noise characteristic of our RF-AWG apparatus, we utilized the interferometric radio-frequency arbitrary waveform generation (RF-AWG) setup of Fig. 3.1, programmed to generate single-tone RF pulses at 80 GHz. The key components of this setup are: a self-referenced mode-locked fiber laser (Menlo Systems FC1500-250-WG, 250 MHz repetition rate, synchronized to a stable 10 MHz external

clock); a high-resolution commercial pulse shaper (Finisar 1000S, 40 nm operating bandwidth, 10 GHz resolution); ~6.6 km of dispersive medium (SMF, total dispersion ~100 ps/nm); and a high-speed near-ballistic uni-travelling-carrier photodiode (NBUTCPD). The amount of dispersion is carefully fine-tuned such that 4 ns, 80 GHz waveform bursts, one from each mode-locked laser pulse, line up in phase with each other in a continuous fashion, thus artificially creating an almost continuous single-frequency RF tone at 80 GHz.

Since we were not able to measure this signal directly with the scope, the generated waveform was down-converted with our second-harmonic W-band mixer driven with a local oscillator signal set to 39 GHz (equivalent to 78 GHz down-conversion), as in Fig. 5.1. Setting the LO to 78 GHz allowed slightly higher conversion efficiency and harmonic extinction up to ~15 dB. Moreover, the local oscillator was synchronized to the same stable 10 MHz clock signal that was used to synchronize the repetition rate of the mode-locked laser.

Figure 5.4(a) depicts the temporal profile of the down-converted signal measured with a 20 GHz real-time oscilloscope. A near single frequency tone is clearly observed, although some modulation that repeats at the 4 ns laser period remains. The frequency of the measured signal in baseband is 2 GHz, which given the 78 GHz LO, corresponds to an original W-band signal at 80 GHz.

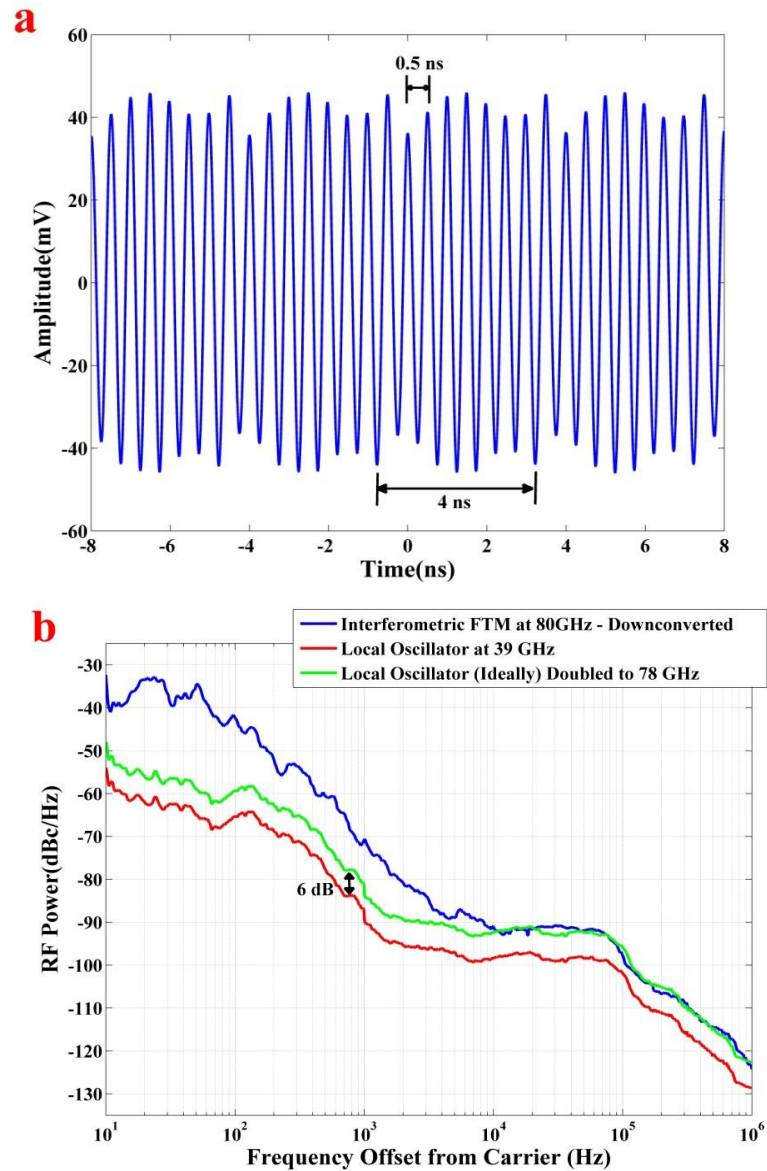


Figure 5.4: Phase-noise measurement results – (a) Temporal profile of the down-converted 80 GHz waveform (LO =  $2 \times 39$  GHz). (b) Phase-noise measurements of the down-converted 80 GHz waveform (in blue), utilized LO frequency at 39 GHz (in red), and its ideal projection to 78 GHz (in green).

The down-converted 2 GHz signal was then directed to an RF spectrum analyzer, equipped with a phase-noise measurement utility. Single-sideband (SSB) phase-noise

measurements are then carried out on this waveform from 10 Hz to 1 MHz using the following equation:

$$\mathcal{L}(f) = \frac{\text{Power within 1Hz bandwidth at frequency } f}{\text{Total Signal Power}} \quad (5.1)$$

The result of phase-noise analysis on this down-converted signal is presented in Fig. 5.4(b), blue curve. It is necessary to emphasize again that the obtained plot is the phase-noise curve for the down-converted signal; where the down-conversion stage may add to the phase-noise of the original 80 GHz signal. In order to achieve a better understanding of this effect, we also measured the phase-noise of the local oscillator (39 GHz) driving the mixer and overlaid it with the previous measurement in Fig. 5.4(b), red curve. Also, since we are using a second-harmonic mixer, ideally, the 78 GHz LO frequency should have  $20 \log_{10}(2) = 6$  dB higher phase-noise than the driving 39 GHz signal coming from the generator [92]. This curve is also plotted in the same figure in green. Specifically, as we observe from comparing these two curves, at frequency deviations above 10 kHz, phase-noise is dominated by the LO signal, and not that of the W-band tone generated through our RF-AWG scheme.

Next, to provide comparison with modern electronic RF arbitrary waveform generator systems, we utilized a Tektronix AWG7000A (9.6 GHz analog bandwidth at 6 dB) and programmed it to generate a continuous 5 GHz RF tone. We must note that due to the fact that the current state-of-the-art electronic AWG systems cannot generate W-band signals directly, we were forced to use phase-noise measurements of this 5 GHz signal and project it to the W-band (namely 80 GHz) by assuming ideal up-conversion of this signal.

Also, to provide a fair comparison, we clocked the electronic AWG device with the same stable 10 MHz used for our W-band generation and phase-noise measurements.

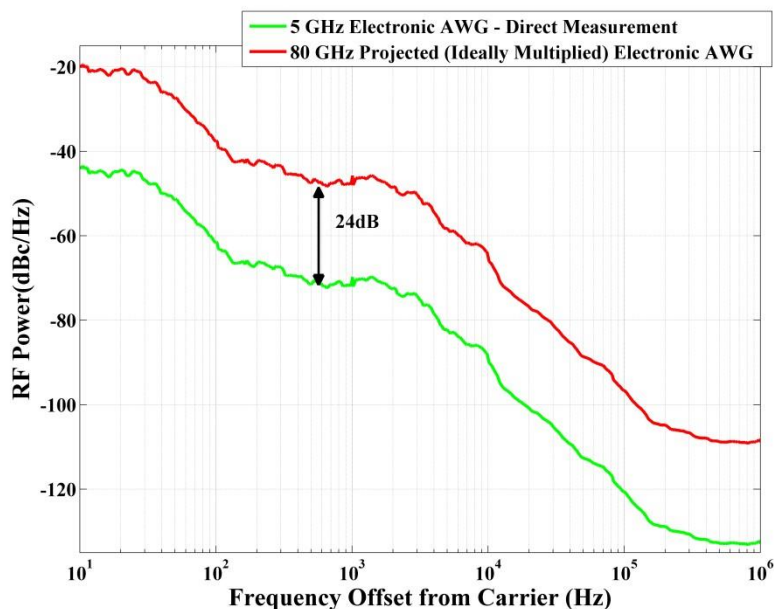


Figure 5.5: Phase-noise measurement of a 5 GHz RF signal generated using state-of-the-art electronic AWG and its projection to 80 GHz assuming ideal up-conversion.

Next, to provide comparison with modern electronic RF arbitrary waveform generator systems, we utilized a Tektronix AWG7000A (9.6 GHz analog bandwidth at 6 dB) and programed it to generate a continuous 5 GHz RF tone. We must note that due to the fact that the current state-of-the-art electronic AWG systems cannot generate W-band signals directly, we were forced to use phase-noise measurements of this 5 GHz signal and project it to the W-band (namely 80 GHz) by assuming ideal up-conversion of this signal. Also, to provide a fair comparison, we clocked the electronic AWG device with the same stable 10 MHz used for our W-band generation and phase-noise measurements.

Figure 5.5 shows the phase-noise curve of this 5 GHz waveform. In this plot, we have assumed ideal frequency multiplication effect on the phase-noise [92], meaning that this increase of  $20 \log_{10}(80 \text{ GHz} / 5 \text{ GHz}) = 24 \text{ dB}$  is the best case scenario when the 5 GHz signal is multiplied up to 80 GHz. In reality, the actual phase-noise is slightly degraded in practical electronic or photonic-assisted [86] frequency multiplication.

Finally, Fig. 5.6 illustrates the projected phase-noise of the 80 GHz signal that would be generated from the frequency-multiplied electronic AWG overlaid with the phase-noise measurement of our photonic-assisted RF-AWG setup at the same 80 GHz frequency from Fig. 5.4(b). This plot clearly shows that our scheme's phase-noise for W-band generation substantially outperforms that projected for a frequency-multiplied commercial electronic arbitrary waveform generator at all offset frequencies measured. According to the measurement, the phase-noise advantage of our scheme is as high as 35 dB (at ~3.5 kHz offset). We reiterate that because our phase-noise measurement of the down-converted photonic generated 80 GHz signal is limited by the LO over much of the high frequency range, its actual phase-noise advantage may be substantially better than suggested by Fig. 5.6.

As a final note, we point out that although the phase-noise advantages of mode-locked laser based generation of single frequency RF tones has been much explored [90,91], particularly around 10 GHz, the measurement presented here is the first to our knowledge confirming the potential for strong phase-noise advantage in photonic arbitrary waveform generation.

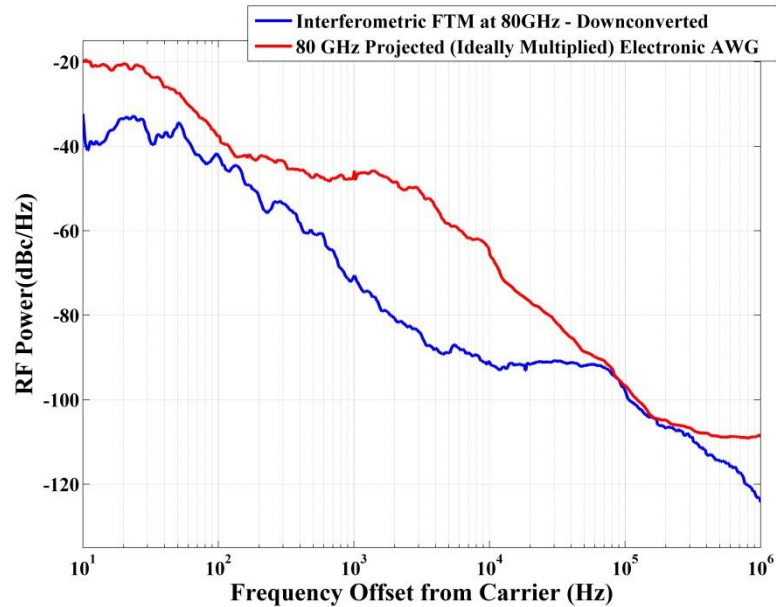


Figure 5.6: Comparison between the projected phase-noise of state-of-the-art electronic AWG versus down-converted phase-noise of our photonic-assisted RF-AWG, both at 80 GHz.

## 5.5 Ultrafine-Resolution Ranging in W-band

As an application example of the presented RF-AWG in W-band, we conduct a multi-target high-resolution ranging experiment. The schematic block diagram of this setup is outlined in Fig. 5.7(a). Instead of directly facing each other, the transmitter and receiver blocks in Fig. 5.1(a) are now positioned approximately side by side. In the ranging environment, four reflective aluminum objects are placed within the antenna beams as targets. A small reflective sphere, a double-plate reflector set, consisting of two flat sheets B1 and B2, and a final reflector C, placed  $\sim 5.2$  meters away. Some photographs of the ranging configuration are also provided in Figs. 5.7(b)–(d).

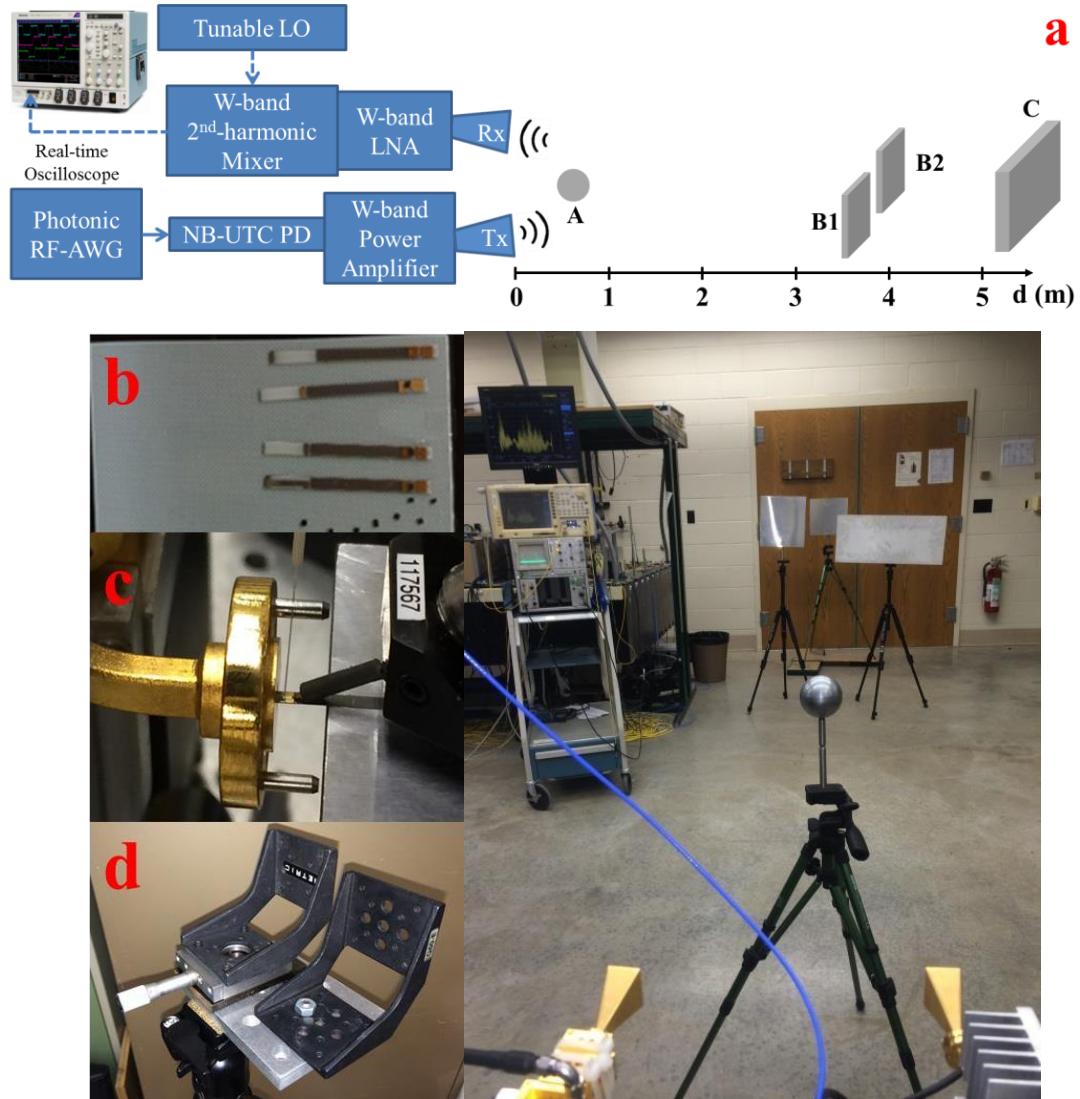


Figure 5.7: Ultra-high resolution W-band ranging experiments. – (a) Setup schematic (b) NBUTC-PD chips. (c) Electrical and optical probing configuration. (d) Tunable double-plate reflector set. (e) Photograph of an example ranging experiment with all 4 objects in the beam path (from Tx-Rx pair point-of-view).

The generated W-band linear down-chirp waveform (70-100 GHz), described in Figs. 5.2(b) and 5.2(c) is employed as a sensing waveform. In order to conduct ranging, we first measure the waveform of Fig. 5.2 via multiple LO measurements (using the real-time oscilloscope) and with only one reflector placed in the beam direction. The reference

reflector is then be removed, and all targets are placed in the environment. The new waveform at the receiver is measured and cross-correlated offline with the reference. The obtained cross-correlations are plotted versus both round-trip time ( $\Delta t$ ) and range displacement with respect to the transceiver ( $\Delta z = c\Delta t/2$ , where  $c$  is the speed of light).

First, according to Figs. 5.7(a) and 5.7(d), we have four targets in the environments. The results from correlation measurements, obtained using the linearly-chirped sounding waveform, are presented in Fig. 5.8. To demonstrate the importance of time aperture expansion, we use two waveform sequences for ranging; one which is un-modulated, and the other which is modulated with a length-15 modified PN sequence coding to expand the unambiguous ranging to over 60 nanoseconds, corresponding to Figs. 5.8(a) and 5.8(b).

As demonstrated in Fig. 5.8(a), when PN-modulated chirps are transmitted, three main reflection peaks can be distinguished in the correlation result. The first peak, with roughly 0.2 normalized cross-correlation power, has a round-trip time of 2.114 ns, corresponding to a range displacement of 31.71 cm with respect to the transceiver. The relatively low peak height is due to the small target cross section of the aluminum ball compared to the other objects. By magnification of the peak around  $\sim 25$  ns (3.75 m) in Fig. 5.8(b), as shown in Fig. 5.8(c), we discover that it actually consists of two distinct peaks reflected from sheets B1 and B2. The 0.19 ns temporal difference between these two peaks indicates that the sheets are separated by 28.5 mm. Finally, there is a single peak from sheet C at 34.66 ns (5.2 m) with a lower peak height compared with those of the double-plate set because of more path loss through a longer propagation distance.

In contrast, when the unmodulated waveform is utilized, reflection peaks repeat themselves every 4 ns, the repetition period of the laser. Since the round-trip time span of

these four objects is much longer ( $\sim 35$  ns), this creates ambiguity in determining the actual position of the reflectors, Fig. 5.8(a). Furthermore, we barely distinguish the reflection peak of the small metal sphere in Fig. 5.8(a) since it is completely submerged in the sidelobes of other stronger reflectors. These results serve as convincing evidence that we are able to increase the unambiguous range of detection through our arbitrary expansion of the repetition period of the sensing waveform.

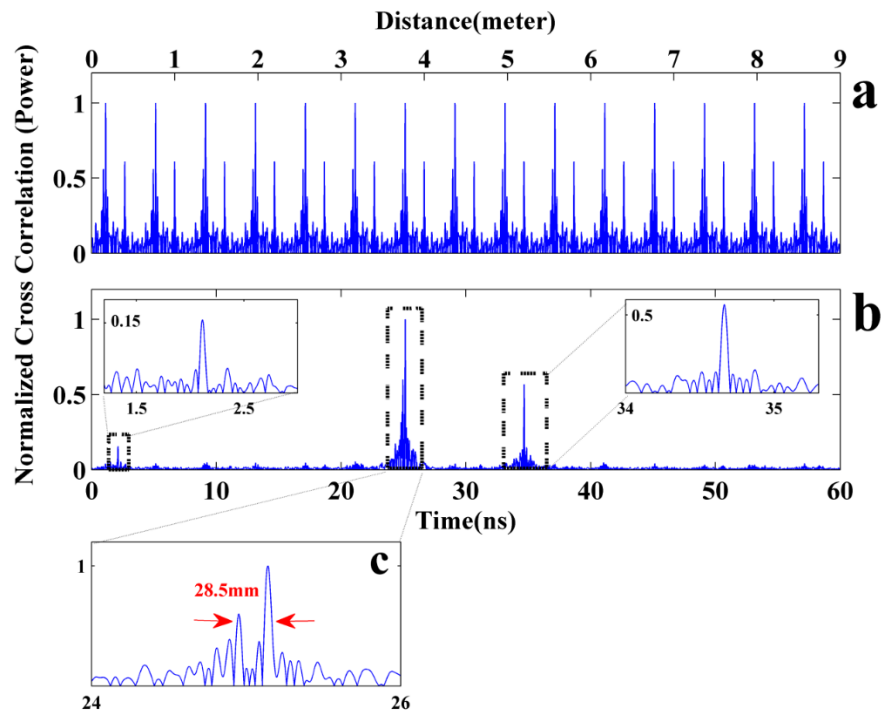


Figure 5.8: High-resolution W-band multi-target ranging experimental results – (a) Ranging results with un-modulated sensing waveform. (b) Ranging results with length-15 modified PN-modulated sensing waveform. (c) Magnified view from 24-26 ns of (b).

For our ultrafine resolution ranging experiments, reflector C is used for reference characterization and then removed and only the double-plate reflector set with fine tunability of relative distance between the two targets is positioned about 3.8m from the

Tx-Rx antenna pair. A photograph of this tunable double-plate reflector is provided in Fig. 5.7(d). To demonstrate the range resolution of this setup, we gradually decrease the separation between the two flat sheets B1 and B2 and repeat the ranging procedure. By taking measurements with multiple LO's, we are able to circumvent the 17 GHz bandwidth limit of the mixer and achieve even finer resolution.

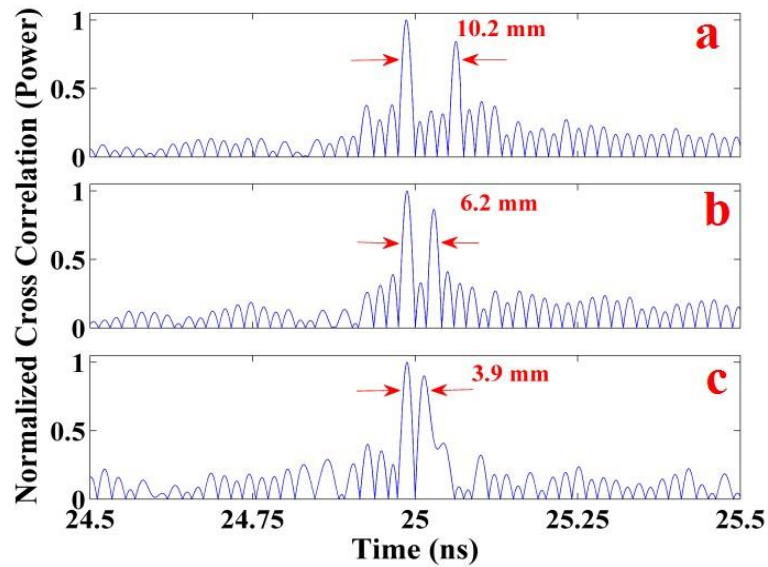


Figure 5.9: Ultrafine resolution W-band ranging experimental results – (a) ~10 mm target separation. (b) ~6 mm target separation. (c) ~4 mm target separation.

We first place the two reflectors roughly 10 mm from each other and retrieve their relative distance via cross-correlation. The cross-correlation plot is depicted in Fig. 5.9(a). The time difference between the two peaks yields a 10.2 mm distance between the two objects. Next we move the objects closer to each other and generate new cross-correlations. The results of placing the objects at ~6 mm and ~4 mm are illustrated in Figs. 5.9(b) and 5.8(c). In each case the cross-correlation peak pairs are clearly distinct and differentiable from the background noise and sidelobes. Figure 5.9(c) depicts the finest depth resolution

we were able to experimentally obtain. The 3.9 mm separation is very close to the theoretical limit for a 30 GHz ranging chirp.

To our knowledge, the achieved 3.9 mm range resolution is significantly better than previous demonstrations in the W-band [11,54,94], including both electrical and photonic-assisted schemes. It also improves, but to a lesser extent, on resolutions reported for experiments with signals generated electronically in considerably higher MMW and sub-THz frequency bands [9,10]. By generating sensing waveforms with comparable bandwidths but at substantially lower center frequencies (~90 GHz as compared with ~600 GHz), we provide a practical way to overcome the excessive path loss and atmospheric absorption of the higher frequency regions, without sacrificing range resolution, while still avoiding the congestion in the microwave and low MMW regime. Further details comparing our scheme with previous works are provided in Table 5.2. We must also point out that the arbitrariness of our generated waveforms can provide added opportunities for optimization of the sensing waveform, such as windowing for sidelobe suppression and Doppler-immune radar [57,58].

Table 5.2: Comparison of prominent MMW and sub-THz ranging systems.

RF Ranging System	Center Frequency (GHz)	Bandwidth (GHz)	Sensing Waveform	Range Resolution (cm)
Ref. [11]	94	12	Short Pulse	1.2
Ref. [54]	95	0.84	Linear Chirp	30
Ref. [94]	94	0.8	FMCW*	19
Ref. [9]	590	29	FMCW	0.5
Ref. [10]	675	26	FMCW	0.58
This Work	85	30	Linear Chirp	0.39

\* FMCW: Frequency-modulated continuous-wave radar

## 6. ULTRABROADBAND RADIO-FREQUENCY ARBITRARY WAVEFORMS IN DENSE MULTIPATH ENVIRONMENTS

### 6.1 Introduction

A very important application of ultrabroadband RF arbitrary waveforms is overcoming RF channel dispersion and multipath [49]. A significant amount of research has been conducted in the characterization and compensation of multipath and dispersion in ultrabroadband channels via RF-AWG [93-98]. As a prominent example, a recent study in our group extensively explored various channel pre-compensation (or beamforming) techniques in highly-dense multipath environments for the frequencies of up to 12 GHz [49]. These evaluations demonstrate that the availability of ultrabroadband arbitrary RF waveforms allow us not only to compensate highly-complex multipath and dispersive environments, but also implement temporal and spatial focusing between the transmitter and receiver, giving rise to new applications like high-speed covert communications.

Antenna dispersion and reflections from various objects in the RF environment are the main disadvantages of ultrabroadband wireless channels, especially indoors. Figure 6.1 shows an example of 12 GHz channel measurement performed in our laboratory. In this channel, omni-directional transmitter (Tx) and receiver (Rx) antennas (ELECTROMETRICS EM-6865) are placed in two separate rooms (~12 m separation) in a non-line-of-sight (NLOS) configuration, as in Fig. 6.1(a). Because of reflections from the walls, cabinets and large metallic surfaces present in the environment, a short pulse excitation at

the transmitter would result in a complex combination of various replicas of the pulse with different amplitudes and delays at the receiver, as seen in Fig. 6.1(b). In the frequency domain, due to this multipath effect, the channel would have undesirable spectral fades and frequency-dependent spectral phase content, Fig. 6.1(c).

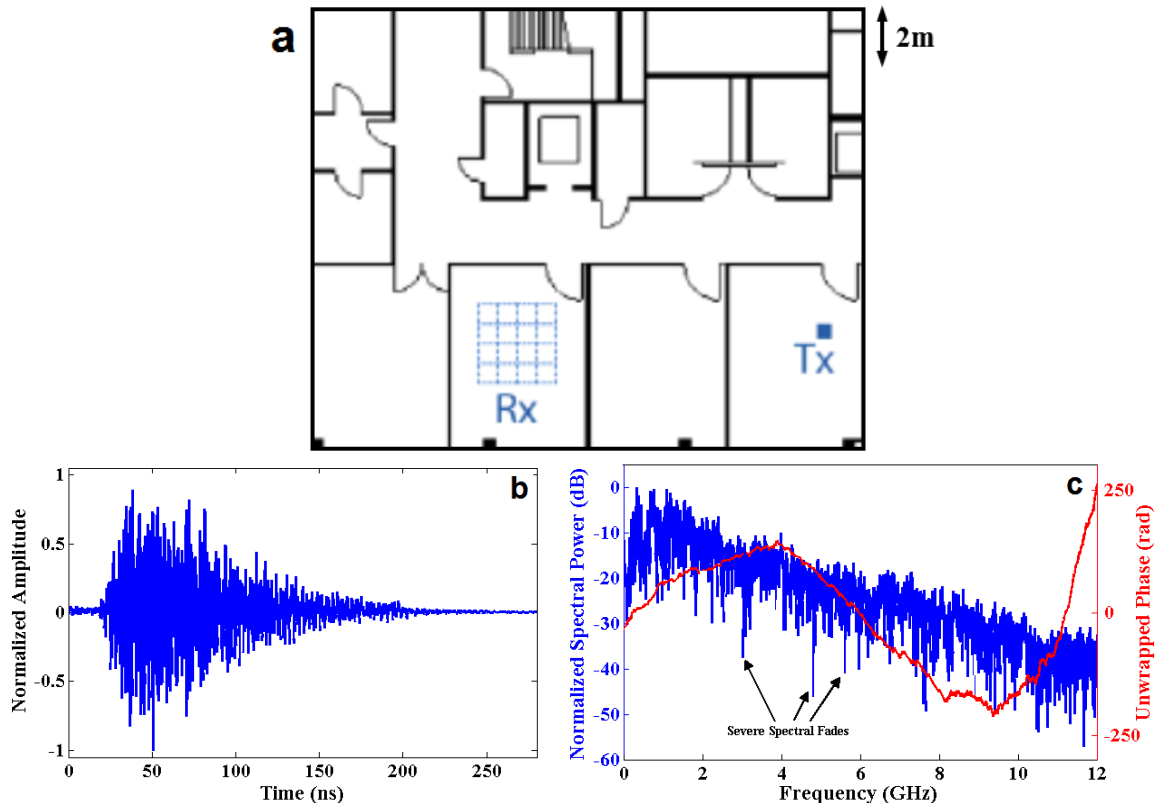


Figure 6.1: Highly-dense multipath channel measurement – (a) Bird’s eye view of the laboratory environment. Tx: Transmitter, Rx: Receiver (on 80cm  $\times$  80cm positioner grid). (b) Channel impulse response. (c) Channel spectral content.

In order to measure the channel impulse response of Fig. 6.1, we use spread-spectrum channel sounding [49], where an ultrabroadband frequency-chirped RF signal is propagated through the channel. After being detected at the receiver and deconvolved with the original transmitted waveform the multipath channel impulse response is fully obtained.

For this measurement and all other experiments in this chapter, we use the commercially available Tektronix arbitrary waveform generator (AWG-7122B) in interleaving mode as the programmable electrical source. The 24 GS/s sampling rate of the AWG provides sufficient bandwidth to probe channels up to 12 GHz.

To characterize the multipath channel, as well as provide comparison for various beamforming techniques described later in this chapter, we introduce the following commonly known metrics:

$$\text{RMS Delay Spread} = \left( \frac{\int_0^T d\tau (\tau - \bar{\tau})^2 |s(\tau)|^2}{\int_0^T d\tau |s(\tau)|^2} \right)^{1/2} \quad (6.1)$$

where,

$$\bar{\tau} = \frac{\int_0^T d\tau \tau |s(\tau)|^2}{\int_0^T d\tau |s(\tau)|^2} \quad (6.2)$$

In (6.1) and (6.2),  $s(\tau)$  is the impulse response of the channel at delay  $\tau$  relative to the first detectable arriving signal. Also,  $T$  is the approximate total duration the channel and  $\bar{\tau}$  is the weighted average delay. In general, channel characteristic metrics strongly depend on the selected noise floor level. This threshold level should be as low as possible to capture all the real energies, but high enough to avoid noise effects [53]. In our calculations, we define a 40 dB threshold level with respect to the maximum detected power and set all components below this level equal to zero. To reduce noise even further, in each measurement we averaged over a large number of waveforms (typically 1000) and bring the measurement noise floor sufficiently down. In a practical system this level of accuracy is not required, and one would not perform such averaging mainly due to its time cost. In the case of the multipath channel of Fig. 6.1(b), the channel impulse response extends to ~150 ns and utilizing (6.1), an RMS delay spread of 25.36 ns is calculated.

Another important parameter, especially to quantify the time compression of various beamforming techniques, is the temporal peak-to-average power ratio (PAPR), described as below [49]:

$$\text{Temporal PAPR} = 10 \log_{10} \left( \frac{\max\{|s(t)|^2\}}{\frac{1}{T} \int_0^T d\tau |s(\tau)|^2} \right) \quad (6.3)$$

The temporal PAPR metric (reported in decibels) is especially important for receivers in which decision making is directly based on thresholding. To provide a fair comparison, in the results presented in this chapter, we measure the PAPR over a 150 ns time window ( $T$ ) for all channels and 300 ns time window for the compressed channels as they are twice as large (a direct result of convolution). The multipath channel of Fig. 6.1(b) has a relatively low temporal PAPR value of 16.48 dB.

In Section 6.2, we describe common ultrabroadband RF channel pre-compensation schemes, such as time reversal, that utilize the channel impulse response information to spatio-temporally compress ultrabroadband multipath channels. This procedure transfers all the receiver complexity to the transmitter site, and since RF-arbitrary waveform generation is more mature for ultrabroadband systems than their filter/receiver counterparts, allows the advancement of many broadband and ultrabroadband applications. We also conduct experiments over the ultrabroadband channel of Fig. 6.1 and provide comparison between the aforementioned temporal focusing criteria, as well as similar spatial focusing measures, for the uncompensated versus compensated channels.

In Section 6.3, we conduct experiments over the same ultrabroadband channel up to 12 GHz, by further taking advantage of a multiple antenna system. In recent years intensive research has been performed to explore the opportunities of multiple antenna

systems in connection with sophisticated transmit beamforming schemes over broadband and ultrabroadband channels [49]. The addition of multiple antenna techniques can potentially allow achieving increased information rate and better temporal/spatial focusing compared to that possible with a single transmit-receive antenna pair [99-107]. Most previous works in multiple antenna beamforming systems are based on modelling and simulation. For example, [106,107] mathematically analyze various performance advantages of time reversal beamforming for multiple-input single-output (MISO) systems as compared to their single-input single-output (SISO) counterpart. This gives a basic prediction of MISO capabilities when the measured data are noise free and the estimated impulse responses are perfectly accurate. A few researchers have also studied MISO systems in the ultra-wideband (UWB) frequency regime experimentally by applying transmit beamforming [49,103,104].

Here, we evaluate and analyze both experimentally and theoretically the characteristics of MISO systems using our RF-AWG infrastructures in a dense multipath laboratory environment over the frequency range of up to 12 GHz. The spatial and temporal focusing gain of our 4 transmitter – 1 receiver ( $4 \times 1$ ) beamforming MISO system over the original SISO beamforming channel are reported in Section 6.3 and various findings are recounted. In Section 6.4, we provide in-depth mathematical and numerical analysis of the temporal focusing gain of MISO beamforming by providing general models. Finally, extensive simulations using the IEEE 802.15.4a standard [108], derived for UWB channels, are conducted to confirm our findings.

## 6.2 Channel Pre-Compensation via RF-AWG

As briefly introduced in the previous section, subsequent to channel measurement, ultrabroadband multipath channels can be spatio-temporally compressed by pre-compensation (or beamforming) techniques, enabled through RF-AWG. Time Reversal (TR) is the most common of such pre-compensation schemes, which was originally proposed as a solution to compensate the distortion of inhomogeneous acoustic environments [109,110]. As its name suggests, in TR, the channel impulse response is reversed (and conjugated for complex channels) in the time domain, and used as a pre-matched-filter at the transmitter. By propagating the time-reversed waveform through the channel, multipath components add up coherently at the receiver at a particular time, resulting in high temporal focusing. Additionally, for highly-dense multipath environments, such as that of Fig. 6.1, it is experimentally shown that TR exhibits strong spatial focusing, which can be used for high-speed covert communication applications and frequency re-use in multi-user systems. The received channel response from TR can be modeled as below (\* and  $\star$  denote complex conjugate and convolution, respectively):

$$y_{TR}(t) = h_{sys}^*(-t) \star h_{sys}(t) \quad (6.4)$$

$$Y_{TR}(f) = H_{sys}^*(f) \cdot H_{sys}(f) = |H_{sys}(f)|^2 \quad (6.5)$$

where,  $y_{TR}(t)$  and  $h_{sys}(t)$  are the time-reversed and original channel responses; while  $Y_{TR}(f)$  and  $H_{sys}(f)$  are their Fourier representations.

Another technique that was introduced for multipath channel beamforming in 2013 by A. Dezfouliyan et al., is called Phase Compensation (PC) [48]. PC pre- and post-filters have been extensively used in optical communications and ultrafast optics, mainly referred

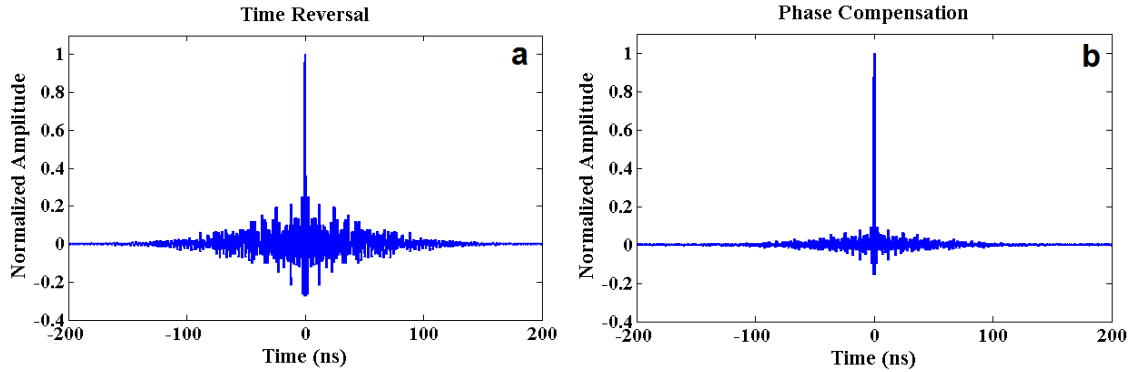


Figure 6.2: Beamforming in the NLOS multipath environment of Fig. 6.1 – (a) Time reversal (TR). (b) Phase compensation (PC).

to there as phase conjugation [52]. Also, similar techniques to PC have been previously used to compensate distortions due to spectral phase variations of certain broadband RF antennas [111,112]. In PC, the transmitted waveform is chosen such that it only compensates for the spectral phase of the channel, i.e.:

$$Y_{PC}(f) = \frac{H_{sys}^*(f)}{|H_{sys}(f)|} \cdot H_{sys}(f) = |H_{sys}(f)| \quad (6.6)$$

where,  $Y_{PC}(f)$  is the phase-compensated channel impulse response in the Fourier domain.

Figure 6.2 compares TR and PC for the NLOS multipath environment of Fig. 6.1(a) when the receive antenna is placed at the center of the grid. Clearly, a very good temporal compression is achieved for both schemes in comparison to Fig. 6.1(b). Although TR is theoretically proven to have maximal signal-to-noise (SNR) performance (not shown here as each plot is normalized to its own peak voltage), it does not fare as well as PC in terms of sidelobe suppression after channel compensation. This is due to the larger roll-off and steeper spectral dips of TR compared to PC and is extensively investigated in [48,49]. Further comparisons of TR and PC techniques in multipath channel compensation have also been mathematically and experimentally analyzed in [49].

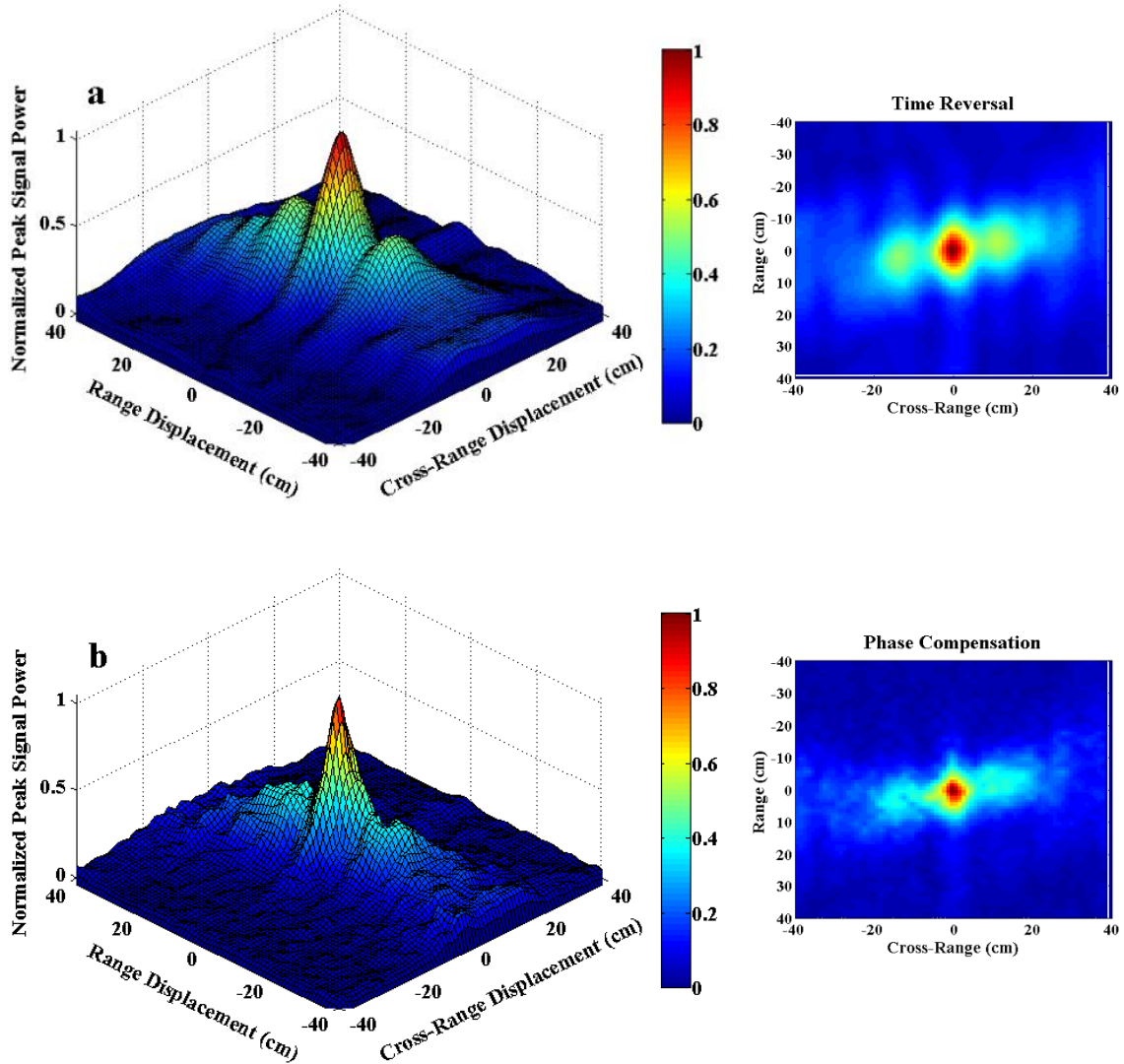


Figure 6.3: Spatial focusing in the NLOS multipath ultra-wideband channel of Fig. 6.1(a) (right: 3D view, left: bird's eye view) – (a) Time reversal (TR). (b) Phase compensation (PC).

As well as temporal focusing, a very appealing feature of dense multipath channels is the spatial focusing one can achieve via TR or PC, meaning that minor displacements of the receiver position, would highly reduce the compression gain of these schemes [49]. This effect is a result of the high uncorrelatedness of two channels with receivers placed only a few wavelengths away from each other. Figure 6.3 illustrates this spatial focusing

for both TR and PC in the  $80\text{cm} \times 80\text{cm}$  grid of Fig. 6.1(a) with a 1 cm resolution. Each plot depicts the normalized received peak power at a specific displacement of the receiver with respect to its original position (center of grid in Fig. 6.1(a)). Here too, we observe that PC outperforms TR, however, the absolute received power values for PC are again lower than that of TR, which is due to the fact that TR results in maximal SNR. This is why the measurements in Fig. 6.3(b) are noisier and less smooth than those of Fig. 6.3(a).

Table 6.1 quantifies the space-time focusing performance of the aforementioned pre-compensation schemes, as compared to the uncompensated channel for the multipath environment of Fig. 6.1. The temporal metrics, RMS delay spread and temporal PAPR, are averaged over 100 different channel realizations, where the transmitter is kept fixed and the receiver is moved to a different grid location. Similar to the definition of RMS delay spread, Eqs. (6.1) and (6.2), and temporal PAPR, Eq. (6.3), in this table we define the following two parameters to quantify the spatial focusing performance:

$$\text{RMS Radial Spread} = \left( \frac{\sum_x \sum_y (x^2 + y^2) P(x, y) \delta x \delta y}{\sum_x \sum_y P(x, y) \delta x \delta y} \right)^{1/2} \quad (6.7)$$

$$\text{Spatial Peak to Average Ratio} = 10 \log_{10} \left( \frac{\max(P(x, y))}{\frac{1}{\Delta x \Delta y} \sum_x \sum_y P(x, y) \delta x \delta y} \right) \quad (6.8)$$

where  $P(x, y)$  is the 2-dimensional matrix of Fig. 6.3;  $x$  and  $y$  are the range and cross-range grid point locations spanning  $-\Delta x/2$  to  $\Delta x/2$  and  $-\Delta y/2$  and  $\Delta y/2$ , respectively; and  $\delta x = \delta y = 1$  cm are the resolution of the grid points.

By analyzing the data of Table 6.1, the benefits of utilizing TR and PC as compared with the uncompensated channel can be clearly noticed. For example, looking at the spatial PAPR numbers, there is practically no spatial focusing when the multipath channel is left

uncompensated, whereas with pre-compensation strong focusing can be achieved. Also, the clear advantage of PC over TR can be observed in all four of our temporal and spatial metrics. However, we must not forget the fact that TR is optimal in terms of SNR (or signal power), which may become more important in high-noise scenarios.

Table 6.1: Comparison of spatio-temporal focusing performance of uncompensated multipath channel, time reversal and phase compensation in the multipath environment of Fig. 6.1. The temporal metrics are averaged over 100 different channel realizations.

Experiment	RMS Delay Spread (ns)	Temporal PAPR (dB)	RMS Radial Spread (cm)	Spatial PAPR (dB)
Uncompensated Channel	25.46	16.48	45.63	0.67
Time Reversal	20.73	25.24	35.17	7.89
Phase Compensation	11.72	31.59	28.03	10.69

### 6.3 Experimental Study of Multiple Antenna Beamforming

As discussed in Section 6.1, combining multiple antenna systems with transmit beamforming can provide further enhancement of the spatio-temporal focusing characteristics of ultrabroadband systems [49, 99-107]. In this section, we present an experimental analysis of a 4×1 MISO beamforming system in our highly-dense multipath laboratory environment. Similar to before, the frequency range of these experiments is limited by our RF equipment to 2-12 GHz (the low frequency limit is the rated cut-off of our RF antennae). We compare the space-time focusing performance of the MISO setup with our previous SISO experiments (as presented in Section 6.2) for both TR and PC scenarios and clearly point out the gained advantages.

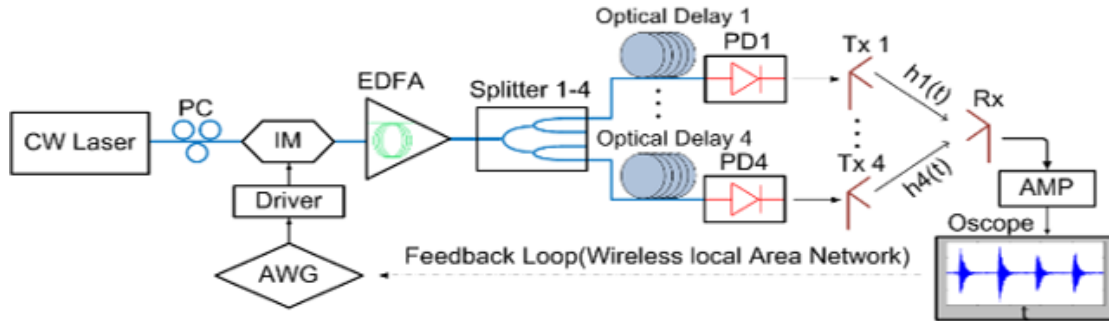


Figure 6.4: Block diagram of the MISO testbed. Inset in bottom right shows the received waveform as a result of chirp excitation. As shown in [49] on page 65.

### 6.3.1 Experimental Setup

Figure 6.4 depicts the block diagram for our  $4 \times 1$  MISO experimental testbed, developed by A. Dezfouliyan in 2013 [49]. The Tektronix AWG-7122B is used in interleaving mode as the programmable electrical source to implement various beamforming schemes. However, the device can only provide one electrical output in interleaving mode, which would normally suffice for testing of single transmit antenna configurations. To extend the capabilities of the AWG to study multiple antenna systems, we program a sequence of four different waveforms (e.g., TR signals for different channels in the MISO configuration) with relative delays longer than the total duration of each wireless channel. The electrical signal from the AWG is mapped to the optical domain by modulating a continuous-wave (CW) optical source (at  $1.55 \mu\text{m}$ ) through an intensity modulator (IM). The optical signal is amplified using an erbium-doped fiber amplifier (EDFA) and then split to drive four different photodiodes (PD), each connected to a different transmit antenna. The individual transmit waveforms are aligned in time using optical fiber delay lines such that they arrive at the single receive antenna in synchronism.

This way we can concurrently excite different antennas with different transmit waveforms by using one single arbitrary waveform generator [49].

Similar to our SISO experiments, wideband omni-directional antennas (ELECTRO-METRICS EM-6865 2-18 GHz) are used as transmitters and receiver. For our experiments, the four transmit antennas are spaced 75 cm apart from each other in the cross-range direction. The output from Rx is passed through a low noise amplifier (BNZ 120UC) with 31 dB gain and directly measured on our 20 GHz real-time oscilloscope.

### 6.3.2 MISO Beamforming Experiment and Results

The first step of the experiment is to measure the 4 channels between each transmitter and the receiver. To do so, a 100 ns-long linear frequency-chirped waveform defined over DC-12 GHz is programmed on the AWG. We then excite the MISO channel with this spread-spectrum signal and record the received response on the Rx oscilloscope. As the relative optical delays in the MISO setup are set to be larger than the temporal duration of each channel (each less than 200 ns), the received waveform would consist of 4 disjoint parts corresponding to MISO channels  $h_1(t)$ - $h_4(t)$  (see inset of Fig. 6.4). Thus, the impulse response information of all four channels, as well as the relative delays from the optical delay lines, can be obtained from a single scope trace at Rx after deconvolution.

After obtaining the complete impulse response of all channels, we program the waveform on the AWG to implement beamforming on each individual channel and sum up coherently at the receiver location. Initially, time reversal is implemented on the MISO setup and the results are shown in Fig. 6.5(a). To show an example of the achieved array gain and better temporal focusing of MISO systems compared to SISO, we turned off all transmitters except from transmitter 1. The received response from applying TR over  $h_1(t)$

is shown in Fig. 6.5(b). As we see from these figures, a peak amplitude gain factor of  $\sim 3.9$  (peak power gain of  $\sim 11.82$  dB) is achieved through MISO, roughly as expected for a four antenna system. On the other hand, the sidelobes of each individual time-reversed channel do not necessarily add up coherently, which should result in an increased temporal PAPR after MISO. According to (6.3), the temporal PAPR for Fig. 6.5(a) is computed to be 27.66 dB and is  $\sim 2.48$  dB higher than the average PAPR of each individual TR channel, which shows better sidelobe suppression of MISO configuration compared to SISO.

Similar to the results of Fig. 6.5, we perform PC in the  $4 \times 1$  MISO configuration and plot the measurement results in Fig. 6.6(a). Also to compare, Fig. 6.6(b) shows PC implementation for the case when only transmitter 1 is on. Here too, we observe a temporal PAPR gain as a result of MISO excitation, however, to a lesser extent of  $\sim 1.24$  dB. This is because the original PC channels are pretty compressed with most of the power concentrated in the peak of the phase-compensated channel and the sidelobes are less important. This finding will be explained mathematically in the next section.

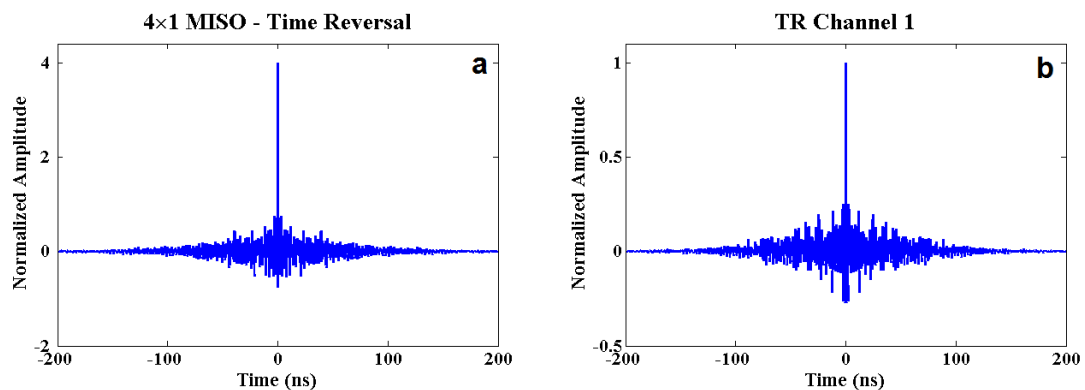


Figure 6.5: TR temporal focusing comparisons – (a)  $4 \times 1$  MISO configuration and (b) TR for only channel 1,  $h_1(t)$ . Amplitudes are normalized to the peak voltage level measured at Rx from only a single antenna TR excitation.

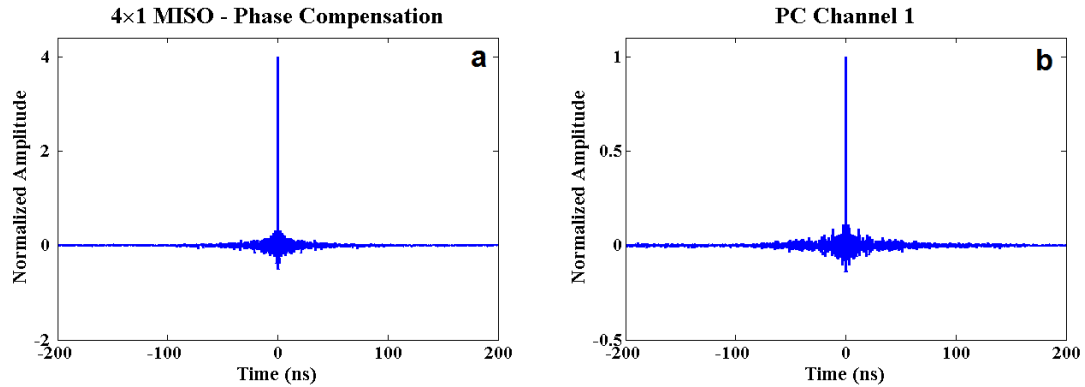


Figure 6.6: PC temporal focusing comparisons – (a)  $4 \times 1$  MISO configuration and (b) PC for only channel 1,  $h_1(t)$ . Amplitudes are normalized to the peak voltage level measured at Rx from only a single antenna PC excitation.

Finally, we perform spatial focusing analysis experiments over our  $80\text{cm} \times 80\text{cm}$  grid at the receiver site for both MISO TR and MISO PC. These results are plotted in Fig. 6.7. As compared to Fig. 6.3, from these plots, we notice enhanced spatial focusing as a result of utilizing the  $4 \times 1$  MISO system, especially in the cross-range wings.

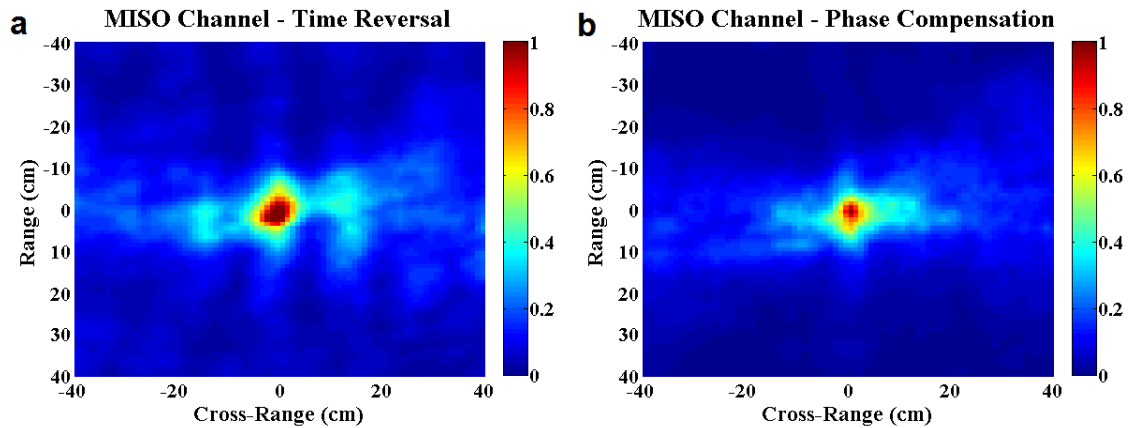


Figure 6.7: Spatial focusing comparisons in  $4 \times 1$  MISO configuration – (a) Time reversal and (b) Phase compensation.

Table 6.2: Comparison of spatio-temporal focusing performance of MISO and SISO beamforming experiment in the multipath environment of Fig. 6.1. The temporal metrics are averaged over 100 different channel realizations.

Experiment	RMS Delay Spread (ns)	Temporal PAPR (dB)	RMS Radial Spread (cm)	Spatial PAPR (dB)
SISO Time Reversal	20.71	25.18	35.17	7.89
MISO Time Reversal	17.80	27.66	29.57	10.34
SISO Phase Compensation	11.52	31.68	28.03	10.69
MISO Phase Compensation	9.93	32.92	26.22	12.60

Table 6.2 summarizes the four spatio-temporal parameters for our  $4 \times 1$  MISO experiments as compared to their SISO counterparts (averaged over the 4 individual SISO channels) in the multipath environment of Fig. 6.1. The temporal metrics, RMS delay spread and temporal PAPR, are averaged over 100 different channel realizations. To obtain these 100 beamforming channels, the transmitter is kept fixed and the receiver is moved to a different grid location and the uncompensated channel responses for all 4 transmitters are measured. Later, using offline computing, SISO and MISO beamforming is implemented and the metrics of Table 6.2 are calculated. To further confirm the generality of these results, we performed complete MISO experiments in the same environment for different receiver locations in the grid of Fig. 6.1 and obtained very similar results in terms of PAPR gain and RMS delay spread reduction. Implementing MISO definitely enhances the space-time focusing performance of both beamforming schemes in all aspects. This is due to the fact that by lining up the peaks of the individual compressed channel responses, we intelligently cause a coherent addition at the space-time origin (zero delay and zero spatial displacement), whereas the sidelobes of the pre-compensated channels are not necessarily programmed to line up. As a result, in the ideal case, simple intuition leads us to expect the

sidelobes (in both temporal and spatial domains) to add up incoherently leading to a narrower spatio-temporal profile. However, the achieved gain from implementing MISO is not quite as large as one may intuitively expect. For example, from the point-of-view of temporal PAPR, it may be natural to expect an approximate 6 dB gain from our  $4 \times 1$  MISO setup as the peak power is enhanced by a factor of 16, while assuming the sidelobes add up incoherently, they should only exhibit a factor of 4 gain. This observation is extensively evaluated mathematically in the next section.

#### 6.4 Theoretical Study of PAPR Gain in MISO Beamforming Systems

To facilitate the mathematical derivations in this section, we assume an  $N \times 1$  MISO beamforming system [113]. All  $N$  channels are assumed to cover the same frequency range, have approximately similar characteristics in terms of temporal duration ( $T$ ), peak and average power, and designated as  $h_1(t)$ ,  $h_2(t)$  to  $h_N(t)$ . According to (6.4), each time-reversed channel can be expressed as:

$$y_{TR_i}(t) = h_i(t) \star h_i^*(-t) = \int_{\tau} h_i(\tau) \cdot h_i^*(\tau - t) d\tau \quad (6.9)$$

$$Y_{TR_i}(f) = |H_i(f)|^2 \quad (6.10)$$

After MISO, these time-reversed channels are configured to add up coherently such that:

$$y_{MISO}(t) = \sum_{i=1}^N y_{TR_i}(t) \quad (6.11)$$

To compute the temporal PAPR, the peak and average channel power need to be quantified. For all channels, we define the time  $t = 0$  as the instant when the channels have maximal power. Thus, we can say:

$$P_{peak}^i = y_{TR_i}^2(t = 0) \quad (6.12)$$

Also, the average power for each channel is computed according to:

$$P_{avg}^i = \langle y_{TR_i}^2(t) \rangle = \frac{1}{T} \int_{-T/2}^{T/2} y_{TR_i}^2(\tau) d\tau \quad (6.13)$$

The symbols  $\langle \rangle$  are shorthand for the time averaging operation.

The PAPR of each individual TR channel is:

$$PAPR^i = 10 \log_{10} \left( \frac{y_{TR_i}^2(0)}{\langle y_{TR_i}^2(t) \rangle} \right) \quad (6.14)$$

Using (6.12) and (6.13) to compute the peak and average power of the resultant  $N \times 1$  MISO channel, we have:

$$P_{peak}^{MISO} = \left( \sum_{i=1}^N P_{peak}^i \right)^2 \simeq N^2 \times P_{peak}^{SISO} = N^2 \times y_{TR}^2(0) \quad (6.15)$$

$$\begin{aligned} P_{avg}^{MISO} &= \sum_{i=1}^N \langle y_{TR_i}^2(t) \rangle + \sum_{i=1}^N \sum_{\substack{j=1 \\ j \neq i}}^N \langle y_{TR_i}(t) \cdot y_{TR_j}(t) \rangle \\ &\simeq N \times P_{avg}^{SISO} + \sum_{i=1}^N \sum_{\substack{j=1 \\ j \neq i}}^N \langle y_{TR_i}(t) \cdot y_{TR_j}(t) \rangle \end{aligned} \quad (6.16)$$

$$PAPR^{MISO} \simeq 10 \log_{10} \left( \frac{N^2 \times P_{peak}^{SISO}}{N \times P_{avg}^{SISO} + \sum_{i \neq j} \langle y_{TR_i}(t) \cdot y_{TR_j}(t) \rangle} \right) \quad (6.17)$$

In simplifying (6.15) and (6.16), we have made the assumption that all individual time-reversed channels have the same peak power ( $P_{peak}^{SISO}$ ), as well as the same average power ( $P_{avg}^{SISO}$ ) at the receiver location. Also, note that the terms  $\langle y_{TR_i}(t) \cdot y_{TR_j}(t) \rangle$  are the cross-correlation coefficients between each two TR channels. We will refer to these terms as  $C_{ij}$  from now on.

At this time, we can justify the statement made in the previous section that for a  $4 \times 1$  MISO beamforming system, it is ideally expected to achieve a PAPR gain of  $\sim 6$  dB.

If all  $C_{ij}$ 's are equal to zero, i.e., the cross-correlation coefficient of all TR channels is zero the MISO PAPR equals:  $10 \log_{10}(N) + PAPR^{SISO}$ . By substituting  $N = 4$ , we see that by going from SISO to MISO, the temporal PAPR will increase by 6 dB.

However, we will show later that although this is a natural expectation to have, it is very hard to satisfy the requirements for achieving this limit, i.e.,  $C_{ij} = 0$  for all  $i \neq j$ . Hence, in the next few paragraphs in this section, we focus on these  $C_{ij}$ 's.  $C_{ij}$  can be expressed as a convolution equation computed at time  $t = 0$ :

$$C_{ij} = \frac{1}{T} \int_{-T/2}^{T/2} y_{TR_i}(\tau) y_{TR_j}(\tau) d\tau = \frac{1}{T} y_{TR_i}(t) \star y_{TR_j}(-t) \Big|_{t=0} \quad (6.18)$$

By using Fourier analysis, (6.18) can be expressed as:

$$C_{ij} = \frac{1}{T} \times \int_{-\infty}^{\infty} df Y_{TR_i}(f) Y_{TR_j}(f) \quad (6.19)$$

Equation (6.5) can further simplify (6.19), relating it to the original multipath channels, as:

$$C_{ij} = \frac{1}{T} \times \int_{-\infty}^{\infty} df |H_i(f)|^2 \cdot |H_j(f)|^2 \quad (6.20)$$

A similar relationship can be obtained for MISO PC beamforming for the cross-correlations values as below:

$$C_{ij} = \frac{1}{T} \times \int_{-\infty}^{\infty} df |H_i(f)| |H_j(f)| \quad (6.21)$$

As we observe from (6.20) and (6.21), in order for  $C_{ij}$ 's to be equal to zero for all  $i \neq j$ , the intersection of any two multipath channel must be zero. That means the fades of one channel must exactly line up with the maximum transmission regions of all others. This is a very hard requirement to meet, which is why the 6 dB limit is a very hard gain to achieve.

Specifically for time reversal, (6.20) can be simplified even more in the time domain. If we consider  $R_{ij}(\tau)$  as the cross-correlation function between the two original channels,  $h_i(t)$  and  $h_j(t)$ , that is:

$$R_{ij}(\tau) = \int_{-\infty}^{\infty} h_i(t) h_j(t - \tau) dt \quad (6.22)$$

The Fourier transform of  $R_{ij}(\tau)$  is:  $H_i(f) \cdot H_j^*(f)$ . Thus, according to Parseval's equality, (6.20) can also be expressed as:

$$C_{ij} = \frac{1}{T} \times \int_{-\infty}^{\infty} d\tau R_{ij}^2(\tau) = \langle R_{ij}^2(\tau) \rangle \quad (6.23)$$

According to (6.20) and (6.21), it is clear that the cross-correlation coefficients ( $C_{ij}$ 's) are the summation of non-negative values and in order for  $C_{ij}$  to be equal to zero or negligible to other terms in (6.17), the two channels must have zero correlation at all time instances. This is practically impossible and basically the reason why we achieved a MISO gain of only 2.48 dB instead of the ideal 6 dB in the previous section.

Tables 6.3 and 6.4 report the cross-correlation coefficients ( $C_{ij}$ ) for our MISO beamforming experiments in Section 6.3, calculated offline for all mutual channels using (6.20) and (6.21). All reported values are normalized to their corresponding SISO (TR or PC) channels' average power ( $P_{avg}^{SISO}$ ). To further provide a clear comparison with the original uncompensated channels, in Table 6.5, we also provide the normalized correlation coefficients for all measured channels prior to beamforming.

Table 6.3: Mathematical analysis of channel cross-correlations ( $C_{ij}$ ) for the MISO TR experiments of Section 6.3, normalized to SISO channels' average power ( $P_{avg}^{SISO}$ ).

Normalized Channel Correlations	TR Channel 1	TR Channel 2	TR Channel 3	TR Channel 4
TR Channel 1	–	0.41	0.38	0.34
TR Channel 2	0.41	–	0.49	0.42
TR Channel 3	0.38	0.49	–	0.47
TR Channel 4	0.34	0.42	0.47	–

Table 6.4: Mathematical analysis of channel cross-correlations ( $C_{ij}$ ) for the MISO PC experiments of Section 6.3, normalized to SISO channels' average power ( $P_{avg}^{SISO}$ ).

Normalized Channel Correlations	PC Channel 1	PC Channel 2	PC Channel 3	PC Channel 4
PC Channel 1	–	0.70	0.67	0.63
PC Channel 2	0.70	–	0.68	0.66
PC Channel 3	0.67	0.68	–	0.67
PC Channel 4	0.63	0.66	0.67	–

Table 6.5: Normalized correlation coefficients for the uncompensated multipath channels in the experiments of Section 6.3.

Normalized Channel Correlations	Channel 1	Channel 2	Channel 3	Channel 4
Channel 1	–	0.049	0.042	0.024
Channel 2	0.049	–	0.035	0.031
Channel 3	0.042	0.035	–	0.042
Channel 4	0.024	0.031	0.042	–

Although, according to Table 6.5, the original uncompensated multipath channels are highly uncorrelated with correlation coefficients of less than 5%, but the beamforming channels have a high correlation coefficient of up to ~50% for TR and up to 70% for PC. In the MISO TR experiment, the sum of the off-diagonal cross-correlation terms amounts to 5.02 times the average power of each individual SISO channel. In other words, according to (6.17),  $\sum_{i \neq j} \langle y_{TR_i}(t) \cdot y_{TR_j}(t) \rangle = \sum_{i \neq j} C_{ij} = 5.02 \times P_{avg}^{SISO}$ . Thus, plugging in the values of Table 6.3 in (6.17), we have:

$$PAPR^{MISO} = 10 \log_{10} \left( \frac{16 \times P_{peak}^{SISO}}{4 \times P_{avg}^{SISO} + 5.02 \times P_{avg}^{SISO}} \right) \simeq 2.50 + PAPR^{SISO} \quad (6.24)$$

The expected 2.50 dB gain from (6.24) is very close to the experimental result from Section 6.3, 2.48 dB. This confirms that our experiments were very close to expectation and the fact that we could not achieve 6 dB gain was not a limitation set by the experimental environment and not by experimental deficiencies. As anticipated, the more correlated the beamforming channels are, the worse this PAPR gain would be. One way to increase the PAPR gain is to decorrelate the channels even more by physically spacing out the antennas or utilizing polarization diversity [114].

Finally, to evaluate the capabilities of MISO beamforming beyond our specific laboratory environment, we compare their performance based on 15,000 simulated channels using channel models 3, 4, 7 and 8 of IEEE 802.15.4a standard (LOS and NLOS indoor office/laboratory and industrial/factory environments) [108]. These channels were defined over a 10 meter Tx/Rx antenna separation and frequency range of 2-10 GHz. Table 6.6 shows the statistical results of the RMS delay and the temporal PAPR for the uncompensated, TR, PC,  $4 \times 1$  MISO TR, and MISO PC channels. Similar to our

experiments, it is also observed in these results that for both cases of LOS and NLOS, the PAPR gain is lower than the simple 6 dB value and as the channel models do not have any spatial correlations embedded, it seems that this just stems from the nature of beamforming over these dense multipath channels. Furthermore, in all simulations, we see that the MISO gain for PC is considerably less than the MISO gain for TR, which is because of the fact that the original four compensated PC channels have a higher concentration of power in their main lobes compared to their TR counterparts.

Table 6.6: 4×1 MISO beamforming simulations based on channel models 3, 4, 7 and 8 of the IEEE 802.15.4a standard (LOS and NLOS indoor office/factory environment).

	<b>Indoor Office/Laboratory Environment</b>		<b>Industrial/Factory Environment</b>	
	<b>LOS (#3)</b>	<b>NLOS (#4)</b>	<b>LOS (#7)</b>	<b>NLOS (#8)</b>
Original Channel PAPR (dB)	30.80 (std 0.82)	20.73 (std 0.88)	26.23 (std 1.05)	20.21 (std 0.77)
Time-Reversed Channel PAPR (dB)	31.16 (std 0.21)	28.18 (std 0.20)	32.94 (std 0.21)	27.32 (std 0.08)
4×1 TR MISO Channel PAPR (dB)	33.07 (std 0.19)	31.23 (std 0.26)	34.38 (std 0.20)	31.96 (std 0.07)
Phase-Compensated Channel PAPR (dB)	32.28 (std 0.15)	30.14 (std 0.17)	33.29 (std 0.17)	29.14 (std 0.10)
4×1 PC MISO Channel PAPR (dB)	33.76 (std 0.15)	31.67 (std 0.11)	34.56 (std 0.16)	32.88 (std 0.10)
Original Channel RMS Delay (ns)	13.73 (std 1.42)	20.57 (std 1.48)	9.82 (std 1.77)	58.42 (std 3.44)
Time-Reversed Channel RMS Delay	12.62 (std 1.46)	19.14 (std 1.42)	10.83 (std 1.78)	56.29 (std 2.99)
4×1 TR MISO Channel RMS Delay	8.86 (std 0.99)	13.09 (std 0.96)	7.98 (std 1.16)	31.67 (std 1.79)
Phase-Compensated Channel RMS Delay	10.71 (std 1.41)	14.32 (std 1.31)	8.88 (std 1.30)	36.13 (std 2.78)
4×1 PC MISO Channel RMS Delay	7.48 (std 1.21)	10.12 (std 1.13)	3.06 (std 1.21)	24.12 (std 2.62)

std: Standard deviation

To compare with our MISO TR experimental results, in the NLOS indoor office/laboratory channels, the simulated MISO TR temporal compression gain (3.05 dB) is larger than observed experimentally. This suggests that for our experiments, there may be some spatial correlations that add to the cross-channel correlations and reduce the ideal performance of MISO. This point clearly shows the importance of experimental implementations from the application perspective.

## 7. SUMMARY AND CONCLUDING REMARKS

In this dissertation we presented a novel photonics-based RF-arbitrary waveform generation setup capable of generating programmable microwave, millimeter-wave and sub-terahertz waveforms with high time-bandwidth product capability for ultrabroadband applications. The presented setup is optimized to resolve limitations of previous electrical and photonic-assisted RF-AWG systems, such as maximum achievable center frequency, reduced performance in passband scenarios, low time-bandwidth product, limited temporal duration, high timing jitter, and incorporation of real-time data modulation. As a result, various ultrabroadband programmable RF waveforms are generated across different frequency bands, such as 2-52 GHz and 70-110 GHz.

In the latter part of the dissertation, RF-AWG systems are utilized in two ultrabroadband RF application settings, namely high-resolution W-band ranging and dense multipath channel compensation. The first application demonstration is conducted using our developed photonics-based RF-AWG generation system in millimeter-wave frequencies and the second using a commercially available electronic RF-arbitrary waveform generator in the low microwaves. Through these experiments, we demonstrate that current RF-AWG techniques have reached an acceptable level of maturity to be directly exploited in different ultrabroadband applications.

In our simple W-band (75-110 GHz) ranging experiments, by allowing, for the first time, RF-arbitrary waveform generation covering the full 40 GHz bandwidth using our scheme, we achieved a record range resolution of 3.9 mm. The achieved range resolution is not only significantly better than previous demonstrations in the W-band region, but also improves, although to a lesser extent, on resolutions reported for experiments with signals generated electronically in considerably higher MMW and sub-THz frequency bands. By generating sensing waveforms with comparable bandwidths but at substantially lower center frequencies ( $\sim 90$  GHz as compared with  $\sim 600$  GHz), we provide a practical way to overcome the excessive path loss and atmospheric absorption of the higher frequency regions, without sacrificing range resolution, while still avoiding the congestion in the microwave and low MMW regime.

In Chapter 6, we utilize RF-AWG to analyze and compensate highly-dense ultrawideband electrical channels below 12 GHz. Two pre-compensation beamforming schemes are experimentally implemented over the ultrabroadband microwave channel using RF-AWG. We further utilize our RF-AWG infrastructures to analyze the temporal and spatial focusing characteristics of these channels in single- and multiple-antenna scenarios. Lastly, a mathematical assessment is provided to derive the equations that govern the limits to the temporal focusing gain of these schemes (specifically temporal PAPR) in MISO beamforming systems and simulations based on the UWB channel model further confirm our findings.

Although photonics-based ultrabroadband RF-AWG techniques have matured to an acceptable degree, in most implementations they are carried out using bulk optic equipment. Recently several steps have been taken to implement these devices with much

lower performance characteristics using integrated fiber/waveguide grating structures or on-chip optical pulse shapers (e.g. using Silicon microring resonators) for RF-AWG [64-69], but they are still at a very low level of maturity and require more research attention. This is an essentially important step for scaling down the size of the setups through integration would promote potential applications of RF-AWG with small footprint and handheld devices.

Finally, we note that such waveform generation techniques would generally be considered as transmitter technologies, as they are used to provide arbitrary waveforms at a wireless or radar transmitter. Photonic signal processing may also be applied advantageously as a receiver technology, i.e., for real-time processing of radar return signals or incoming communications waveforms. In the context of systems employing ultrabroadband arbitrary waveform transmission, photonically implemented phase filters offer a potentially attractive solution for realizing pulse compression functionality in the receiver. Early RF photonic phase filters based on hyperfine resolution optical pulse shapers have been demonstrated for compression of photonically generated RF waveforms with TBWPs of order ten but with time apertures  $<1$  ns [115,116]. Newer RF photonic phase filters based on dispersive propagation of optical frequency comb sources are capable of larger TBWP and have recently been demonstrated for compression of electronically generated spread spectrum signals [117,118]. In the future we anticipate systems in which photonics will be used both for generation and wireless transmission of large TBWP radio frequency signals and for subsequent real-time pulse compression processing in the receiver.

## LIST OF REFERENCES

## LIST OF REFERENCES

- [1] G.R. Aiello and G.D. Rogerson, "Ultra-wideband wireless systems," *Microwave Magazine, IEEE*, vol. 4, pp. 36-47, 2003.
- [2] A. Goldsmith, *Wireless Communications*: Cambridge University Press, 2005.
- [3] T. Nagatsuma, N. Kukutsu, and Y. Kado, "Photonic generation of millimeter and terahertz Waves and its applications," *AUTOMATIKA: Journal for Control, Measurement, Electronics, Computing and Communications*, vol. 49, 2008.
- [4] J. Federici and L. Moeller, "Review of terahertz and subterahertz wireless communications," *Journal of Applied Physics*, vol. 107, pp. 111101, 2010.
- [5] J.W. Shi, C.B. Huang, and C.L. Pan, "Millimeter-wave photonic wireless links for very high data rate communication," *NPG Asia Materials*, vol. 3, pp. 41-48, 2011.
- [6] N.W. Chen, J.W. Shi, H.J. Tsai, J.M. Wun, F.M. Kuo, J. Hesler, T.W. Crowe, and J.E. Bowers, "Design and demonstration of ultra-fast W-band photonic transmitter-mixer and detectors for 25 Gbits/sec error-free wireless linking," *Optics Express*, vol. 20, pp. 21223-21234, 2012.
- [7] X.Y. Li, Z. Dong, J.J. Yu, N. Chi, Y.F. Shao, and G.K. Chang, "Fiber-wireless transmission system of 108 Gb/s data over 80 km fiber and 2x2 multiple-input multiple-output wireless links at 100 GHz W-band frequency," *Optics Letters*, vol. 37, pp. 5106-5108, 2012.
- [8] S. Koenig, D. Lopez-Diaz, J. Antes, F. Boes, R. Henneberger, A. Leuther, A. Tessmann, R. Schmogrow, D. Hillerkuss, R. Palmer, T. Zwick, C. Koos, W. Freude, O. Ambacher, J. Leuthold, and I. Kallfass, "Wireless sub-THz communication system with high data rate," *Nature Photonics*, vol. 7, pp. 977-981, 2013.
- [9] K.B. Cooper, R.J. Dengler, N. Llombart, T. Bryllert, G. Chattopadhyay, E. Schlecht, J. Gill, C. Lee, A. Skalare, I. Mehdi, and P.H. Siegel, "Penetrating 3-D Imaging at 4-and 25-m Range Using a Submillimeter-Wave Radar," *IEEE Transaction on Microwave Theory and Techniques*, vol. 56, pp. 2771-2778, 2008.
- [10] K.B. Cooper, R.J. Dengler, N. Llombart, A. Talukder, A.V. Panangadan, C.S. Peay, I. Mehdi, and P.H. Siegel, "Fast, high-resolution terahertz radar imaging at 25 meters," *Proc. SPIE*, vol. 7671, pp. 76710Y-8, 2010.

- [11] T.F. Tseng, J.M. Wun, W. Chen, S.W. Peng, J.W. Shi, and C.K. Sun, "High-depth-resolution 3-dimensional radar-imaging system based on a few-cycle W-band photonic millimeter-wave pulse generator," *Optics Express*, vol. 21, pp. 14109-14119, 2013.
- [12] T. Nagatsuma, S. Horiguchi, Y. Minamikata, Y. Yoshimizu, S. Hisatake, S. Kuwano, N. Yoshimoto, J. Terada, and H. Takahashi, "Terahertz wireless communications based on photonics technologies," *Optics Express*, vol. 21, pp. 23736-23747, 2013.
- [13] R.W. McMillan, "Terahertz imaging, millimeter-wave radar," *NATO Security through Science Series*, vol. 2, pp. 243-268, 2006.
- [14] M. Tonouchi, "Cutting-edge terahertz technology," *Nature Photonics*, vol. 1, pp. 97-105, 2007.
- [15] J.A. Zeitler and L.F. Gladden, "In-vitro tomography and non-destructive imaging at depth of pharmaceutical solid dosage forms," *European Journal of Pharmaceutics and Biopharmaceutics*, vol. 71, pp. 2-22, 2009.
- [16] D.M. Sheen, J.L. Fernandes, J.R. Tedeschi, D.L. McMakin, A.M. Jones, W.M. Lechelt, and R.H. Severtsen, "Wide-bandwidth, wide-beamwidth, high-resolution, millimeter-wave imaging for concealed weapon detection," *Passive and Active Millimeter-Wave Imaging XVI, Proc. SPIE*, vol. 8715, pp. 871509-871519, 2013.
- [17] H.J. Hansen, "Standoff detection using millimeter and submillimeter wave spectroscopy," *Proc. IEEE*, vol. 95, pp. 1691-1704, 2007.
- [18] L. Chao, M.N. Afsar, and K.A. Korolev, "Millimeter Wave Dielectric Spectroscopy and Breast Cancer Imaging," *European Microwave Integrated Circuits Conference (EuMIC)*, pp. 572-575, 2012.
- [19] J.L. Neill, B.J. Harris, A.L. Steber, K.O. Douglass, D.F. Plusquellic, and B.H. Pate, "Segmented chirped-pulse Fourier transform submillimeter spectroscopy for broadband gas analysis," *Optics Express*, vol. 21, pp. 19743-19749, 2013.
- [20] A.P. Colombo, Y. Zhou, K. Prozument, S.L. Coy, and R.W. Field, "Chirped-pulse millimeter-wave spectroscopy: Spectrum, dynamics, and manipulation of Rydberg-Rydberg transitions," *Journal of Chemical Physics*, vol. 138, pp. 014301, 2013.
- [21] Federal Communications Commission (FCC) reports and regulations – <http://www.fcc.gov>.
- [22] S. Hardy, "Keysight Technologies Offers 65-GSa/s, 20-GHz arbitrary waveform generator," *Lightwave Online*, vol.31, 2014.

- [23] V. Torres-Company, J. Lancis, P. Andrés, and L. Chen, "20 GHz arbitrary radio-frequency waveform generator based on incoherent pulse shaping," *Optics Express*, vol. 16, pp. 21564-21569, 2008.
- [24] A. Dezfouliyan and A. Weiner, "Photonic synthesis of high fidelity microwave arbitrary waveforms using near field frequency to time mapping," *Optics Express*, vol. 21, pp. 22974-22987, 2013.
- [25] H.B. Gao, C. Lei, M.H. Chen, F.J. Xing, H.W. Chen, and S.Z. Xie, "A simple photonic generation of linearly chirped microwave pulse with large time-bandwidth product and high compression ratio," *Optics Express*, vol. 21, pp. 23107-23115, 2013.
- [26] F. Zhang, X. Ge, and S. Pan, "Background-free pulsed microwave signal generation based on spectral shaping and frequency-to-time mapping," *Photonics Research*, vol. 2, pp. B5-B10, 2014.
- [27] A. Rashidinejad, Y. Li, and A.M. Weiner, "Recent advances in programmable photonic-assisted ultrabroadband radio-frequency arbitrary waveform generation," *IEEE Journal of Quantum Electronics*, vol. 52, pp. 1-17, 2016.
- [28] A.J. Seeds and K. Williams, "Microwave photonics," *IEEE Journal of Lightwave Technology*, vol. 24, pp. 4628-4641, 2006.
- [29] J. Capmany and D. Novak, "Microwave photonics combines two worlds," *Nature Photonics*, vol. 1, pp. 319-330, 2007.
- [30] T. Nagatsuma and Y. Kado, "Microwave photonic devices and their applications to communications and measurements," *PIERS Online*, vol. 4, pp. 376380, 2008.
- [31] J.D. McKinney and A.M. Weiner, "Photonic synthesis of ultrabroadband arbitrary electromagnetic waveforms," in *Microwave Photonics*, 2nd ed. C.H. Lee, Ed. USA: CRC Press, 2013, pp. 243-306.
- [32] J.P. Yao, "Photonic generation of microwave arbitrary waveforms," *Optics Communications*, vol. 284, pp. 3723-3736, 2011.
- [33] J.D. McKinney, D.E. Leaird, and A.M. Weiner, "Millimeter-wave arbitrary waveform generation with a direct space-to-time pulse shaper," *Optics Letters*, vol. 27, pp. 1345-1347, 2002.
- [34] J. Chou, Y. Han, and B. Jalali, "Adaptive RF-photonic arbitrary waveform generator," *IEEE Photonics Technology Letters*, vol. 15, pp. 581-583, 2003.
- [35] I. Lin, J.D. McKinney, and A.M. Weiner, "Photonic synthesis of broadband microwave arbitrary waveforms applicable to ultra-wideband communication," *IEEE Microwave and Wireless Components Letters*, vol. 15, pp. 226- 228, 2005.

- [36] J.D. McKinney, "Background-free arbitrary waveform generation via polarization pulse shaping," *IEEE Photonics Technology Letters*, vol. 22, pp. 1193-1195, 2010.
- [37] W. Chao and J.P. Yao, "Photonic generation of chirped millimeter-wave pulses based on nonlinear frequency-to-time mapping in a nonlinearly chirped fiber Bragg grating," *IEEE Transaction on Microwave Theory and Techniques*, vol. 56, pp. 542-553, 2008.
- [38] R. Ashrafi, Y. Park, and J. Azana, "Fiber-based photonic generation of high-frequency microwave pulses with reconfigurable linear chirp control," *IEEE Transaction on Microwave Theory and Techniques*, vol. 58, pp. 3312-3319, 2010.
- [39] M. Li and J.P. Yao, "Photonic generation of continuously tunable chirped microwave waveforms based on a temporal interferometer incorporating an optically-pumped linearly-chirped fiber Bragg grating," *IEEE Transaction on Microwave Theory and Technology*, vol. 59, pp. 3531-3537, 2011.
- [40] J.W. Shi, F.M. Kuo, C. Nan-Wei, S.Y. Set, C.B. Huang, and J.E. Bowers, "Photonic generation and wireless transmission of linearly/nonlinearly continuously tunable chirped millimeter-wave waveforms with high time-bandwidth product at W-band," *IEEE Photonics Journal*, vol. 4, pp. 215223, 2012.
- [41] W. Liu and J.P. Yao, "Photonic generation of microwave waveforms based on a polarization modulator in a Sagnac loop," *IEEE Journal of Lightwave Technology*, vol. 32, pp. 3637-3644, 2014.
- [42] C.B. Huang, D.E. Leaird, and A.M. Weiner, "Time-multiplexed photonic enabled radio-frequency arbitrary waveform generation with 100ps transitions," *Optics Letters*, vol. 32, pp. 3242-3244, 2007.
- [43] C.B. Huang, D.E. Leaird, and A.M. Weiner, "Synthesis of millimeter-wave power spectra using time-multiplexed optical pulse shaping," *IEEE Photonics Technology Letters*, vol. 21, pp. 1287-1289, 2009.
- [44] A.M. Weiner, "Femtosecond pulse shaping using spatial light modulators," *Review of Scientific Instruments*, vol. 71, pp. 1929-1960, 2000.
- [45] A.M. Weiner, "Ultrafast optical pulse shaping: A tutorial review," *Optics Communications*, vol. 284, pp. 3669-3692, 2011.
- [46] A. Rashidinejad and A.M. Weiner, "Photonic radio-frequency arbitrary waveform generation with maximal time-bandwidth product capability," *IEEE Journal of Lightwave Technology*, vol. 32, pp. 3383-3393, 2014.

- [47] A. Dezfouliyan and A.M. Weiner, "Experimental investigation of UWB impulse response and time reversal technique up to 12 GHz: omnidirectional and directional antennas," *IEEE Transactions on Antennas and Propagation*, vol. 60, pp. 3407-3415, 2012.
- [48] A. Dezfouliyan, and A.M. Weiner, "Phase compensation communication technique against time reversal for ultra-wideband channels," *IET Communications*, vol. 7, pp. 1287-1295, 2013.
- [49] A. Dezfouliyan, "Experimental investigation of ultrawideband wireless systems: Waveform generation, propagation estimation, and dispersion compensation," PhD dissertation, Department of Electrical and Computer Engineering, Purdue University, West Lafayette, IN, 2013.
- [50] M.A. Muriel, J. Azana, and A. Carballar, "Real-time Fourier transformer based on fiber gratings," *Optics Letters*, vol. 24, pp. 1-3, 1999.
- [51] V. Torres-Company, D.E. Leaird, and A.M. Weiner, "Dispersion requirements in coherent frequency-to-time mapping," *Optics Express*, vol. 19, pp. 24718-24729, 2011.
- [52] A.M. Weiner, *Ultrafast Optics*: Wiley, 2009.
- [53] A. W. Rihaczek, *Principles of High-Resolution Radar*: Artech House, 1996.
- [54] A.Y. Nashashibi, K. Sarabandi, P. Frantzis, R.D. De Roo, and F.T. Ulaby, "An ultrafast wide-band millimeter-wave (MMW) polarimetric radar for remote sensing applications," *IEEE Transaction on Geoscience and Remote Sensing*, vol. 40, pp. 1777-1786, 2002.
- [55] M. Miyakawa and J.Ch. Bolomey, "Microwave imaging I: microwave computed tomography," in *Non-Invasive Thermometry of the Human Body*: CRC Press, 1995, pp. 105-126.
- [56] G.G. Brown, B.C. Dian, K.O. Douglass, S.M. Geyer, S.T. Shipman, and B.H. Pate, "A broadband Fourier transform microwave spectrometer based on chirped pulse excitation," *Review of Scientific Instruments*, vol. 79, pp. 053103-053103.13, 2008.
- [57] N. Levanon and E. Mozeson, *Radar Signals*: Wiley-IEEE Press, 2004.
- [58] N. Levanon, *Radar Principles*: J. Wiley & Sons, New York, 1988.
- [59] D. Jackson, R. Priest, A. Dandridge, and A. Tveten, "Elimination of drift in a single-mode optical fiber interferometer using a piezoelectrically stretched coiled fiber," *Applied Optics*, vol. 19, pp. 2926-2929, 1980.

- [60] A. Rashidinejad and A.M. Weiner, "Generation of programmable passband chirped electrical pulses using optical interferometry," *Conference on Lasers and Electro-Optics (CLEO), OSA Technical Digest (online)*, article CTu3G.4, 2013.
- [61] V.R. Supradeepa, C.M. Long, D.E. Leaird, and A.M. Weiner, "Fast characterization of dispersion and dispersion slope of optical fiber links using spectral interferometry with frequency combs," *IEEE Photonics Technology Letters*, vol. 22, pp. 155-157, 2010.
- [62] D.R. Cox and D.V. Hinkley, *Theoretical Statistics*: Chapman & Hall, 1974.
- [63] Y. Li, A. Dezfouliyan, and A.M. Weiner, "Photonic synthesis of spread spectrum radio frequency waveforms with arbitrarily long time apertures," *IEEE Journal of Lightwave Technology*, vol. 32, pp. 3580-3587, 2014.
- [64] D.E. Leaird and A.M. Weiner, "Femtosecond direct space-to-time pulse shaping in an integrated-optic configuration," *Optics Letters*, vol. 29, pp. 1551-1553, 2004.
- [65] F.M. Soares, N.K. Fontaine, R.P. Scott, J.H. Baek, X. Zhou, T. Su, S. Cheung, Y. Wang, C. Junesand, S. Lourdudoss, K.Y. Liou, R.A. Hamm, W. Wang, B. Patel, L.A. Gruezke, W.T. Tsang, J.P. Heritage, and S.J.B. Yoo, "Monolithic InP 100-channel  $\times$ 10-GHz device for optical arbitrary waveform generation," *IEEE Photonics Journal*, vol. 3, pp. 975-985, 2011.
- [66] C.G.H. Roeloffzen, L. Zhuang, C. Taddei, A. Leinse, R.G. Heideman, P.W.L. van Dijk, R.M. Oldenbeuving, D.A.I. Marpaung, M. Burla, and K.J. Boller, "Silicon nitride microwave photonic circuits," *Optics Express*, vol. 21, pp. 22937-22961, 2013.
- [67] M.H. Khan, H. Shen, Y. Xuan, L. Zhao, S.J. Xiao, D.E. Leaird, A.M. Weiner, and M. Qi "Ultrabroad-bandwidth arbitrary radiofrequency waveform generation with a silicon photonic chip-based spectral shaper," *Nature Photonics*, vol. 4, pp. 117-U130, 2010.
- [68] J. Wang, H. Shen, L. Fan, R. Wu, B. Niu, L.T. Varghese, Y. Xuan, D.E. Leaird, X. Wang, F. Gan, A.M. Weiner, and M. Qi, "Reconfigurable radio-frequency arbitrary waveforms synthesized in a silicon photonic chip," *Nature Communications*, vol. 6, article 5957, 2015.
- [69] L.R. Chen, "Photonic generation of chirped microwave and millimeter wave pulses based on optical spectral shaping and wavelength-to-time mapping in silicon photonics," *Optics Communications*, in press, 2015. DOI: 10.1016/j.optcom.2015.04.023

- [70] G. Baxter, S. Frisken, D. Abakoumov, Z. Hao, I. Clarke, A. Bartos, and S. Poole, "Highly programmable wavelength selective switch based on liquid crystal on silicon switching elements," *Optical Fiber Communication Conference (OFC)*, pp. 3, 2006.
- [71] M.A. Roelens, J.A. Bolger, D. Williams, and B.J. Eggleton, "Multi-wavelength synchronous pulse burst generation with a wavelength selective switch," *Optics Express*, vol. 16, pp. 10152-10157, 2008.
- [72] A. Rashidinejad, D.E. Leaird, and A.M. Weiner, "Ultrabroadband radio-frequency arbitrary waveform generation with high-speed phase and amplitude modulation capability," *Optics Express*, vol. 23, pp. 12265-12273, 2015.
- [73] T. Kleine-Ostmann and T. Nagatsuma, "A review on terahertz communications research," *Journal of Infrared, Millimeter and Terahertz Waves*, vol. 32, pp. 143-171, 2011.
- [74] A.J. Seeds, M.J. Fice, K. Balakier, M. Natrella, O. Mitrofanov, M. Lamponi, M. Chtioui, F. van Dijk, M. Pepper, G. Aeppli, A. G. Davies, P. Dean, E. Linfield, and C. Renaud, "Coherent terahertz photonics," *Optics Express*, vol. 21, pp. 22988-23000, 2013.
- [75] A.J. Seeds, "Terahertz photonics for communications," *Optical Fiber Communication Conference (OFC), OSA Technical Digest (online)*, Invited Talk Th4H.1, 2014.
- [76] A. M. Weiner, A. Dezfooliyan, Y. Li, and A. Rashidinejad, "Selected advances in photonic ultrabroadband radio-frequency arbitrary waveform generation," *International Topical Meeting on Microwave Photonics (MWP)*, pp. 325-328, 2013.
- [77] Y. Li, A. Rashidinejad, J. M. Wun, D.E. Leaird, J. W. Shi, and A. M. Weiner, "Photonic generation of W-band arbitrary waveforms with high time-bandwidth products enabling 3.9mm Range Resolution," *Optica*, vol. 1, pp. 446-454, 2014.
- [78] M.D. McKinley, K.A. Remley, M. Myslinski, J.S. Kenney, D. Schreurs, and B. Nauwelaers, "EVM calculations for broadband modulated signals," in *Proceedings of 64<sup>th</sup> ARFTG Conference*, pp. 45-52, 2004.
- [79] A. Kaneko, H. Yamazaki, and Y. Miyamoto, "Linear optical modulator," *Optical Fiber Communication Conference (OFC), OSA Technical Digest (online)*, Invited Talk W3K.5, 2014.
- [80] J. Proakis and M. Salehi, *Digital Communications*: McGraw-Hill, 2007.
- [81] H. Ito, S. Kodama, Y. Muramoto, T. Furuta, T. Nagatsuma, and T. Ishibashi, "High-speed and high-output InP-InGaAs unitraveling-carrier photodiodes," *IEEE Journal of Selected Topics in Quantum Electronics*, vol. 10, pp. 709-727, 2004.

- [82] A. Beling, H.G. Bach, G.G. Mekonnen, R. Kunkel, and D. Schmidt, "High-speed miniaturized photodiode and parallel-fed traveling-wave photodetectors based on InP," *IEEE Journal of Selected Topics in Quantum Electronics*, vol. 13, pp. 15-21, 2007.
- [83] A. Stohr, S. Babel, P.J. Cannard, B. Charbonnier, F. van Dijk, S. Fedderwitz, D. Moodie, L. Pavlovic, L. Ponnampalam, C.C. Renaud, D. Rogers, V. Rymanov, A. Seeds, A.G. Steffan, A. Umbach, and M. Weiss, "Millimeter-wave photonic components for broadband wireless systems," *IEEE Transaction on Microwave Theory and Techniques*, vol. 58, pp. 3071-3082, 2010.
- [84] J.W. Shi, F.M. Kuo, and J.E. Bowers, "Design and analysis of ultra-high-speed near-ballistic uni-traveling-carrier photodiodes under a 50 $\Omega$  load for high-power performance," *IEEE Photonic Technology Letters*, vol. 24, pp. 533-535, 2012.
- [85] N.W. Chen, H.J. Tsai, F.M. Kuo, and J.W. Shi, "High-speed-band integrated photonic transmitter for radio-over-fiber applications," *IEEE Transaction on Microwave Theory and Techniques*, vol. 59, pp. 978-986, 2011.
- [86] A. Kanno and T. Kawanishi, "Broadband frequency-modulated continuous-wave signal generation by optical modulation technique," *IEEE Journal of Lightwave Technology*, vol. 32, pp. 3566-3572, 2014.
- [87] J.W. Shi, F.M. Kuo, N.W. Chen, S.Y. Set, C.B. Huang, and J.E. Bowers, "Photonic generation and wireless transmission of linearly/nonlinearly continuously tunable chirped millimeter-wave waveforms with high time-bandwidth product at W-band," *IEEE Photonics Journal*, vol. 4, pp. 215-223, 2012.
- [88] J.M. Wun, C.C. Wei, J.H. Chen, C.S. Goh, S.Y. Set, and J.W. Shi, "Photonic chirped radio-frequency generator with ultra-fast sweeping rate and ultra-wide sweeping range," *Optics Express*, vol. 21, pp. 11475-11481, 2013.
- [89] S.T. Cundiff and A.M. Weiner, "Optical arbitrary waveform generation," *Nature Photonics*, vol. 4, pp. 760-766, 2010.
- [90] F. Quinlan, T.M. Fortier, H. Jiang, A. Hati, C. Nelson, Y. Fu, J.C. Campbell, and S.A. Diddams, "Exploiting shot noise correlations in the photodetection of ultrashort optical pulse trains," *Nature Photonics*, vol. 7, pp. 290-293, 2013.
- [91] T.M. Fortier, M.S. Kirchner, F. Quinlan, J. Taylor, J.C. Bergquist, T. Rosenband, N. Lemke, A. Ludlow, Y. Jiang, C.W. Oates, and S.A. Diddams, "Generation of ultrastable microwaves via optical frequency division," *Nature Photonics*, vol. 5, pp. 425-429, 2011.
- [92] J. Rutman and F.L. Walls, "Characterization of frequency stability in precision frequency sources," in *Proceedings of the IEEE*, vol. 79, pp. 952-960, 1991.

- [93] A. F. Molisch, "Ultra-Wide-Band Propagation Channels," *Proceedings of the IEEE*, vol. 97, pp. 353-371, 2009.
- [94] H. Essen, M. Hägelen, A. Wahlen, K. Schulz, K. Jäger, and M. Hebel, "ISAR imaging of helicopters using millimeter wave radars," *International Journal of Microwave and Wireless Technologies*, vol. 1, pp. 171-178, 2009.
- [95] N. Guo, B.M. Sadler, and R.C. Qiu, "Reduced-complexity UWB timereversal techniques and experimental results," *IEEE Transactions on Wireless Communications*, vol. 6, pp. 4221-4226, 2007.
- [96] K. Popovski, B.J. Wysocki, and T.A. Wysocki, "Modelling and comparative performance analysis of a time-reversed UWB system," *EURASIP Journal on Wireless Communications and Networking*, vol. 7, pp. 1-11, 2007.
- [97] K. Witrisal and M. Pausini, "Statistical Analysis of UWB Channel Correlation Functions," *IEEE Transactions on Vehicular Technology*, vol. 57, pp. 1359-1373, 2008.
- [98] D. Abbasi-Moghadam and V.T. Vakili, "Characterization of indoor time reversal UWB communication systems: Spatial, temporal and frequency properties," *International Journal of Communication Systems*, vol. 24, pp. 277294, 2011.
- [99] C. Zhou, N. Guo, and R.C. Qiu, "Experimental results on multiple-input single-output (MISO) time reversal for UWB systems in an office environment," in *IEEE Military Communications Conference*, pp. 1-6, 2006.
- [100] H.T. Nguyen, I.Z. Kovacs, and P.C.F. Eggers, "A Time Reversal transmission approach for multiuser UWB communications," *IEEE Transactions on Antennas and Propagation*, vol. 54, pp. 3216-3224, 2006.
- [101] Y. Jin, Y. Jiang, and J.M.F. Moura, "Multiple antenna Time Reversal transmission in Ultrawideband communications," in *IEEE Global Telecommunications Conference*, pp. 3029-3033, 2007.
- [102] C. Zhou, N. Guo, and R.C. Qiu, "Time-Reversed Ultra-wideband (UWB) Multiple Input Multiple Output (MIMO) Based on Measured Spatial Channels," *IEEE Transactions on Vehicular Technology*, vol. 58, pp. 2884-2898, 2009.
- [103] Y. Song, Z. Hu, N. Guo, and R.C. Qiu, "Real-time MISO UWB radio testbed and waveform design," in *IEEE Proceedings of the SoutheastCon*, pp. 204-209, 2010.
- [104] Y. Song, N. Guo, and R.C. Qiu, "Implementation of UWB MIMO time-reversal radio testbed", *IEEE Antennas Wireless Propagation Letters*, vol. 10, pp. 796-799, 2011

- [105] A.E. Fouda, F.L. Teixeira, and M.E. Yavuz, "Time-reversal techniques for MISO and MIMO wireless communication systems," *Radio Science Journal*, vol. 47, pp. 1-15, 2012.
- [106] G.C. Ferrante, J. Fiorina, and M.G. Di Benedetto, "Time reversal beamforming in MISO-UWB channels," in *IEEE International Conference on Ultra-Wideband (ICUWB)*, pp. 261–266, 2013.
- [107] G.C. Ferrante, J. Fiorina, and M.G. Di Benedetto, "Robustness of time reversal vs. all-rake transceivers in multiple access channels," *ARXIV*, eprint 1405.4459, 2014.
- [108] A.F. Molisch, K. Balakrishnan, C.C. Chong, S. Emami, A. Fort, J. Karedal, J. Kunisch, H. Schantz, U. Schuster, and K. Siwiak, *IEEE 802.15.4a channel model—Final report*, 2004, [online] Available: online.
- [109] M. Fink, C. Prada, F. Wu, and D. Cassereau, "Self-focusing in inhomogeneous media with time reversal acoustic mirrors," in *IEEE Ultrasonics Symposium*, vol. 2, pp. 681-686, 1989.
- [110] M. Fink, "Time reversal of ultrasonic fields. I. Basic principles," *IEEE Transactions on Ultrasonics, Ferroelectrics and Frequency Control*, vol. 39, pp. 555-566, 1992.
- [111] J.D. McKinney, D. Peroulis, and A.M. Weiner, "Dispersion limitations of ultra-wideband wireless links and their compensation via photonically enabled arbitrary waveform generation," *IEEE Transaction on Microwave Theory and Techniques*, vol. 56, pp. 710-719, 2008.
- [112] J.D. McKinney and A.M. Weiner, "Compensation of the effects of antenna dispersion on UWB waveforms via optical pulse-shaping techniques," *IEEE Transaction on Microwave Theory and Techniques*, vol. 54, pp. 1681-1686, 2006.
- [113] A. Rashidinejad and A.M. Weiner, "Mathematical analysis of peak-to-average power ratio gain in multiple-input single-output beamforming over dense multipath environments," under final preparation, 2016.
- [114] A. Rashidinejad and A.M. Weiner, "Utilizing polarization diversity to increase peak-to-average power ratio gain performance of multiple-input single-output beamforming over dense multipath environments," under final preparation, 2016.
- [115] E. Hamidi and A.M. Weiner, "Phase-only matched filtering of ultrawideband arbitrary microwave waveforms via optical pulse shaping," *IEEE Journal of Lightwave Technology*, vol. 26, pp. 2355-2363, 2008.
- [116] E. Hamidi and A.M. Weiner, "Post-compensation of ultra-wideband antenna dispersion using microwave photonic phase filters and its applications to UWB systems," *IEEE Transaction on Microwave Theory and Techniques*, vol. 57, pp. 890 -898, 2009.

- [117] M.H. Song, V. Torres-Company , A.J. Metcalf, and A.M. Weiner "Multitap microwave photonic filters with programmable phase response via optical frequency comb shaping," *Optics Letters*, vol. 37, pp. 845-847, 2012.
- [118] H.J. Kim, A. Rashidinejad, and A.M. Weiner, "Low-loss ultrawideband programmable RF photonic phase filter for spread spectrum pulse compression," *IEEE Transaction on Microwave Theory and Techniques*, accepted, 2015.

VITA

## VITA

Amir Rashidinejad graduated with a B.Sc. degree in Electrical Engineering from the Sharif University of Technology, Tehran, Iran in 2011. From 2009 to 2011 he was an Undergraduate Research Assistant with the Advanced Communications Research Institute (ACRI) and the Optical Networks Research Laboratory (ONRL) at Sharif University, under the supervision of Prof. Farrokh A. Marvasti and Prof. Jawad A. Salehi.

He joined Purdue University, West Lafayette, IN in September 2011 to pursue his graduate studies and is currently a Graduate Research Assistant in the Ultrafast Optics and Optical Fiber Communications Laboratory, under the supervision of Prof. Andrew M. Weiner. He received his Master's degree in Electrical and Computer Engineering from Purdue University in August 2015 and is currently a Ph.D. candidate in the school of Electrical and Computer Engineering.

His research interests include radio-frequency photonics; ultrafast optics; ultrabroadband microwave and millimeter-wave arbitrary waveform generation and processing; and applications in ranging and communication systems. Amir's research has led to over 15 authored/co-authored publications in peer reviewed journals and international conferences. Amir has served as a reviewer for Optics Express, Optics Letters, IEEE Transaction on Microwave Theory and Techniques, IEEE Journal of Lightwave Technology, IEEE Photonics Journal, and Elsevier Optics Communications.